# Structures magnétiques et micro-systèmes pour applications biologiques

Luiz Zanini

## ▶ To cite this version:

Luiz Zanini. Structures magnétiques et micro-systèmes pour applications biologiques. Autre. Université de Grenoble, 2013. Français. NNT : 2013GRENT004 . tel-00820317

## HAL Id: tel-00820317
## https://theses.hal.science/tel-00820317

Submitted on 3 May 2013

# UNIVERSITÉ DE GRENOBLE

## THÈSE

pour obtenir le grade de

## DOCTEUR de l'**Université de Grenoble**

Spécialité : **Génie Electrique**

Arrêté ministériel : 7 août 2006

Présentée par

## **Luiz Fernando ZANINI**

Ingénieur Matériaux par l'Université Fédérale de Santa Catarina, Brésil

Thèse dirigée par **Gilbert REYNE** et

co-encadrée par **Frédéric DUMAS-BOUCHIAT**

préparée au sein du **Laboratoire de Génie Electrique de Grenoble**

et de l'**Institut Néel**

Ecole Doctorale: **EEATS - Electronique, Electrotechnique, Automatique, Télécommunication, Signal**

## Bio-Mag-MEMS autonomes basés sur des aimants permanents

Thèse soutenue publiquement le **18 février 2013**
devant le jury composé de :

**Dr. Anne-Marie GUE** (Rapporteuse)

**Dr. Paulo WENDHAUSEN** (Rapporteur)

**Dr. Stéphanie DESCROIX** (Examinatrice)

**Dr. Marie FRENEA-ROBIN** (Examinatrice)

**Dr. Gilbert REYNE** (Directeur de thèse)

**Dr. Frédéric DUMAS-BOUCHIAT** (Co-encadrant)

**Dr. Nora DEMPSEY** (Invitée)

# Abstract

The range of applications for magnetic micro- and nano-particles is constantly expanding, in particular in medicine and biology. A number of applications involve particle trapping and deviation under the effect of a magnetic field and field gradient. In most publications, the required magnetic fields are produced either using soft magnetic elements polarized by an external magnetic field, electromagnets or bulk permanent magnets.

Micromagnets produce high fields and favor autonomy and stability while downscaling leads to an increase of field gradients. The challenge is to produce good quality, hard magnetic films in the range of 1 to 100 $\mu$m both in thickness and lateral dimensions and to integrate them into a Bio-Mag-MEMS.

Physical vapor deposition (triode sputtering) is used to prepare high quality rare earth magnets in thick film form. In order to obtain field gradients in the lateral directions, three techniques have been developed:

- Topographic patterning, in which the film itself is patterned either by sputtering onto pre-etched substrates or by etching the magnetic film.

- Thermo-magnetic patterning, which exploits the temperature dependance of coercivity to locally reorient the magnetization.

- Micro magnetic imprinting, which consists of organizing magnetic powder with the aid of the above-cited magnets, then embedding the powder into a polymeric matrix.

Such micro-magnets are autonomous, having no requirements for a cumbersome external field source nor power supply.

Here we demonstrate the potential to develop autonomous devices based on micromagnet arrays. Controlled positioning using superparamagnetic particles as a model is shown at first. Then, the magnet arrays are used to study endocytic processes using magnetically labelled biological elements.

In a step towards device integration, microfluidic channels are produced above the magnet arrays. Magnetic and non-magnetic particles are pumped through the devices and precise positioning, as well as guiding and sorting are performed. High purity is obtained in the sorted solutions.

The good results obtained in the development of micromagnetic flux sources, integration into microdevices and particle/cell handling and sorting indicate the high potential of this work for actual biological and medical applications. Moreover, the biocompatibility and autonomy of such devices allow their use in micro-total-analysis systems, point-of-care or implantable devices.

# Résumé

Les micro et nano billes magnétiques sont de plus en plus utilisées en Biologie et en Médecine, pour une large gamme d'applications. Plusieurs applications utilisent le piégeage et le guidage de ces billes sous l'effet d'un champ et d'un gradient de champ magnétique. Dans la plupart des applications le champ magnétique est macroscopique, créé par un aimant ou un électro-aimant. L'intégration plus poussée est souvent envisagée, dans les articles scientifiques, par des microbobines ou par des éléments magnétiques doux. Ceux-ci doivent alors être polarisés par un champ externe (de nouveau, un électroaimant ou un aimant).

Les micro-aimants mis au point à l'Institut Néel permettent d'obtenir les mêmes inductions que les meilleurs aimants du marché et, par conséquent, de par la réduction d'échelle, des gradients de champ intenses. Ils sont, de plus, favorables à l'autonomie et à la stabilité du système. Le défi est de produire de bonnes couches magnétiques avec des dimensions de l'ordre de 1 à 100 $\mu$m et de les intégrer à des Bio-Mag-MEMS.

Le dépôt physique par phase vapeur (pulvérisation cathodique triode) est utilisé pour le dépôt de ces aimants de haute qualité, en couche épaisse, et à base de terres-rares. Dans le but d'optimiser les gradients latéraux des champs magnétiques, trois techniques ont été développées:

- Le topographic patterning, dans lequel une couche est structurée géométriquement, soit par dépôt sur un substrat pré-gravé, soit par gravure humide après le dépôt.

- Le thermo-magnetic patterning, qui exploite la dépendance thermique de la coercivité pour réorienter localement l'aimantation de la couche.

- Le micro magnetic imprinting, qui consiste à organiser des particules magnétiques à l'aide des aimants mentionnés ci-dessus et, ensuite, de les noyer dans une couche polymérique.

Les micro-aimants présentent l'avantage, majeur pour un microsystème, d'être autonomes. Ils ne nécessitent pas de source externe de champ magnétique, ni d'alimentation électrique. Lors de ces travaux, nous développons des prototypes de microsystèmes fluidiques autonomes basés sur des réseaux de micro-aimants. En premier lieu, la capture par attraction et le positionnement controllé, en utilisant des particules superparamagnétiques comme modèle. Puis, l'étude de phénomènes d'endocytose à l'aide d'éléments biologiques marqués magnétiquement. Dans le but de passer à l'intégration des systèmes, des canaux microfluidiques sont développes sur les réseaux magnétiques. Des particules magnétiques et non-magnétiques sont introduites dans les canaux et leur positionnement, guidage et tri sont réalisés. L'analyse des solutions triées indique une haute efficacité du système.

Les résultats obtenus lors du développement de ces micro-sources de champ magnétiques et de leur intégration dans des microsystèmes, ainsi que la manipulation et tri de particules, démontrent le grand potentiel de ces recherches pour des applications grand public à des systèmes biologiques et médicaux. De plus, la biocompatibilité et l'autonomie de ces systèmes permettent leur utilisation dans des microsystèmes d'analyse totale ($\mu$TAS), des systèmes point-of-care (POC) et des implants biomédicaux, potentiellement jetables et bas coût.

# Contents

# Introduction

The curiosity and the need to understand and handle the tiny constituents of everything has been present among the humankind for millennia. From the hand-held magnifier, to the optical microscope and then to the scanning and transmission electron microscopes, knowledge of what things are made of have dramatically increased. The human body, for instance, is today known at different levels: organs, tissues, cells, constituents of cells, DNA, individual nucleotides. Once each of these parts and their functions are known, the challenge is to manipulate them so that they can perform specific functions at specific sites. Obviously, the human body is not the only subject of interest. Chemical reactions, Micro-Electro-Mechanical-Systems (MEMS), microbiology, etc., can all benefit from the ability to manipulate the world at low-scale.

A field of research which is rapidly expanding concerns micro and nanoparticle handling. These particles can have a vast range of properties and functional compounds added to their surfaces. The techniques used to produce the particles are, themselves, a research field. The goal is to obtain narrower distributions in size, with optimized and reproducible properties and expand the list of available functions a particle can have. The success of these tiny objects can be observed, for example, by the numerous commercial kits which involve the use of particles for bio-assays or to perform sorting of particle-labelled objects (Miltenyi Biotec, DiagnoSwiss, etc.).

Different techniques based on various physical, chemical and biological phenomena can be used to handle objects at the micro and nanoscale. All these techniques present a set of advantages and drawbacks and are more or less susceptible to integration in micro-devices. For instance, dielectrophoresis can be used to act on several particles at once, or on a single particle, and can be easily integrated to a MEMS. However, this technique requires a set of conditions to operate properly (salinity of the medium, balance of responses between the medium and the object, etc.). Optical tweezers can also act on single or multiple objects with very high precision, but are much more difficult to integrate. The final device often requires a large amount of side-equipment, rendering impossible the development of an autonomous and transportable device. The list goes on and on, with electroosmosis, acoustics, thermal actuation...

Giving magnetic properties to an object can increase its potential applications. Contactless actuation allow the manipulation of magnetically labelled objects without direct interference. Magnetic Resonance Imaging (MRI), for instance, is a technique which uses a large number of these particles and their magnetic response to study the internal parts of a subject. Magnetic particles can also be used to label individual objects, which can be then manipulated individually or as a group.

Magnetic separation devices have been developed and are commercially available. The use of bulk magnets for this purpose is evident, since they are a part of our everyday life. However, it is not evident to all that the force created by these large magnets on very small objects can be very weak. The force is, actually, proportional to both the magnetic field and the *field gradient* they produce, thus, a variation of the field in space is of foremost

importance. Unfortunately, the relevant field gradients of bulk magnets are restricted to a limited zone around its edges, and extremely close to it. For practical cases, such magnets fail to attract a very important part of the magnetic particles, especially if those are nano-scaled.

Using downscaled permanent magnets can significantly enhance particle attraction while keeping the advantage of an autonomous magnetic flux source. However, very few reports about it can be found in the literature. The reason is simple: when it comes to developing micro-magnets with the standard techniques of fabrication, one has to choose between

- obtaining high quality magnetic properties and

- precisely controlling the magnet's dimensions.

It is quite straightforward to conclude that a high performance micro-object handling device cannot be developed if these two items are exclusive. Despite of the great potential of micro-magnets, little advances have been done worldwide in this field. Micro-magnets nowadays are usually ferromagnetic thin films based on a two-element iron alloy, or high-performance micro-particles arranged with poor control of particle packaging or dimensions.

The alternatives found for this problem are the use of electromagnets and soft micro-magnets. The magnetic field generated by an electromagnet is easily predictable and controllable. Moreover, their fabrication can be easily adapted to the standard micro-fabrication techniques. The advantages they present are the modulation of the field they produce and the possibility to have a zero field condition, if needed. On the other hand, they present two major drawbacks: Joule heating generated by the required electric current, and the need for external power supply. Soft magnets do not produce heat. However, their field is only generated when they are polarized by an external field, which implies a bulk magnet or an external electromagnet. Turning the field on and off is also possible, though it is not easily modulable. These two alternatives allow actuation at the micro-scale, but the integration to small devices is hardly achievable.

$$* * *$$

In Institut Néel, more precisely in the Micro & Nano Magnetism (MNM) group, high quality magnets in the micrometer range are being developed these last 6-7 years. These magnets are deposited by triode sputtering onto silicon wafers - thus, integration to microsystems is improved - with very high deposition rate (up to 20 $\mu$m/h), as compared to other deposition techniques. Rare-earth based (NdFeB, SmCo), as well as iron based (FePt, mainly) magnets figure in the list of top quality films. The lateral dimensions of these magnets are controlled by a set of recently developed patterning techniques. These techniques allow the development of micromagnets in the lateral dimension range of a few $\mu$m to several mm and thickness range of a few nm to tens, or even hundreds, of $\mu$m.

These magnets are the subject of a few theses developed in the past and others in preparation today. The subjects of these going from the improvement of the magnetic properties of the films, passing by integration to micro-systems, to the recent applications in the levitation of living cells. The potential applications of magnets in biology and medicine are evident. A quick look in a few prestigious scientific journals is enough to conclude that

researchers need to autonomously control the smaller and more specific elements studied every day.

In an effort to meet this demand, the present project was idealized. The centers of interest were magnetism and, later, microfluidics, with a main focus on the applications concerning cell biology. In Grenoble, the expertise of both G2Elab in the conception and modeling of microsystems and Institut Néel in the development and integration of micro-magnets were grouped. Further on, collaborations with research groups in biology, medicine, chemistry and even the conception and fabrication of other types of micro-devices were established. This thesis took place in a strongly collaborative environment, with many researchers of different fields working together for the same purpose.

$$* * *$$

The first part of this thesis consisted of implementing an apparatus for Thermo-Magnetic Patterning (one of the micro-structuration techniques) in Institut Néel. The TMP principle consists of mimicking the thermomagnetic writing for recording media. The first successful tests were performed by F. Dumas-Bouchiat and L. Ranno, using respectively, an excimer laser ($\lambda = 248$ nm) and a YAG laser ($\lambda = 532$ nm). An excimer laser device had been bought by the laboratory and was sitting in its wooden box in the corridor before I even had started. A very rewarding task - though it might not seem, and it didn't by that time - consisted of simply contacting people from the laboratory to assemble available materials and suppliers all over the world to obtain quotes for all the lenses, mirrors and lens mounts we needed. This first task allowed me to understand very quickly that research is not only made of beautiful SEM images and graphs. I soon understood that I should be very grateful for all the condensed experience it brought me in my first days.

A few weeks later I have realized that I had been grateful too soon. The second wave of calls and quotes hit us hard, when we have decided to develop and test microfluidic devices in Grenoble. This further "purchasing mission" allowed us to perform a global search of materials and methods commonly used in microfluidics. The microfluidics apparatus was installed in Minatec and was among the first steps of what is today a very fruitful collaboration with the Laboratoire des Matériaux et du Génie Physique (LMGP). A microfluidics platform was also installed in Institut Néel for practical means. Very good contacts with colleagues in the field and suppliers from different countries were established during this period.

Both periods resulted in a rapid and general introduction in different research fields. A very strong multi disciplinary character was present since the beginning of this thesis. The close collaborations established before and during my period in the laboratory were, in a great part, responsible for what can be presented today. It is clear now that actively participating in the implementation of new activities, as well as having a large contact list, can be very rewarding.

$$* * *$$

This thesis starts with a description of the goals of micro-objects handling. The available techniques are briefly presented, followed by a discussion on the choice of the actuation

methods used here. Fundamentals of the two domains which are the bases of this work, namely *magnetism* and *microfluidics*, are discussed. A non-exhaustive review of the most recent and relevant articles is given, so as to present the advances and issues of each actuation technique. With the advantages of magnetism in mind, and based on the state-of-the-art presented, the ANR (Agence Nationale de la Recherche) EMERGENT Project is introduced and its role in the micro-object handling context is discussed.

The second chapter intends to present the techniques and materials used on the development of magnetic micro-flux sources. Triode sputtering, the high-rate deposition technique used to develop the magnetic films, is described at first, along with the most commonly deposited materials and their characteristics. Magneto-optic imaging and magnetic force microscopy are discussed, since these are uncommon techniques used for the characterization of the patterned magnetic films. A description of the very important micro-structuration methods (topographic and thermo-magnetic patterning, as well as micro-magnetic imprinting) is given. The magnetic patterns used here and the limitations related to patterning with each technique are listed.

The integration of magnetic films to microfluidics is discussed in the third chapter. Polydymethilsiloxane (PDMS), the polymeric material used for all the fluidic devices shown in this report, is introduced. The integration of micro-magnets to PDMS (or planarization, for topographic magnets) is detailed, as well as the development of micro-channel and assembly of the systems. A discussion of flow control systems takes place, followed by the presentation of how pressure-driven control is used here. The chapter ends with a description of the whole setup, including magnets, microfluidic channels and the apparatus for control and observation of fluids and micro-objects.

A model of the magnetic fields and gradients produced by topographic and thermo-magnetically patterned magnets is developed in chapter four. The laminar fluidic flow obtained with the micro-channel is also integrated to the model. The superparamagnetic behavior of magnetic particles is experimentally measured and fitted with the Langevin equation. Particle attraction, capture and deviation is, thus, simulated and the conditions for device optimization are listed.

The fifth and final chapter summarizes the experimental results obtained with the attraction of particles and biological elements. At first, static capture is discussed. The positioning and alignment of magnetic particles of different sizes is observed. Then, cells and bacteria are labelled with nanometer-size magnetic particles and their capture above the micro-magnets is tested. Endocytosis, a natural cell phenomenon, is studied using these nanoparticles and observing the evolution of cell positioning. Particle capturing is also studied inside microfluidic channels. Chessboard-like magnets are integrated to microfluidics channels and particle capture and sorting are performed. Magnetic stripes are, then, used as a way to perform continuous flow separation. The balance of drag and magnetic forces are exploited in order to perform this function. Preliminary results on the use of topographic magnets for both capture and deviation of particles are discussed. Finally, a few more complex functions are described as a perspective. The first results and models developed as a proof-of-concept are presented.

# Chapter 1

# Concepts and context

The micro and nano-scaled world has been a rising research field for the last few years. The advances in micro-fabrication have unveiled a whole world of applications. Micro-grips, tweezers and cutters allow surgeries to be performed by human-controlled robots which act at the point of interest with a precision never seen before. A fingertip can now hold whole electronic devices. Tiny objects can be moved with the beam of an electronic microscope. The list goes on and on.

An especially interesting application which was brought to life by miniaturization is the manipulation of very small objects. The applications are many, from water treatment to cutting-edge medical diagnosis. Researchers in the biological field have been eager to handle blood cells, amoebae, antibodies, proteins, etc. The number of techniques used in such cases are almost as vast as the applications themselves. Systems going from simple downscaled sieves to robust and complex optical tweezers are used and the related results published on a weekly basis.

The forces used to manipulate these small objects come from many different sources. Among the most popular are capillary, dielectrophoretic and electroosmotic forces. Each one presents very different characteristics (intensity and action distance, for instance) which make their selection very important depending on the desired application, the target objects and their surroundings. They also present very different degrees of complexity, as regards the fabrication steps and operation.

The popularity of magnetism in the object handling field is increasing these last few years. Three types of magnetic flux sources are used: electromagnets, soft magnets and permanent magnets. These three methods share two very interesting characteristics: contactless actuation and the possibility to actuate in attraction and/or repulsion. There are, however, a few very different characteristics inherent of each method.

- **Electromagnets**, for instance, are capable of producing modulable magnetic fields and can be turned on and off as desirable. On the other hand, they present the major inconvenient of Joule heating, due to the current passing through the elements. Obviously, another inconvenient is that a power source is needed to generate that current.

- **Soft magnets** do not require an electric current and, thus, do not present the inconvenient of heating. However, since they only generate their own magnetic field when polarized by an external field, the side-equipment is necessarily replaced by a bulk magnet or electromagnet. Modulation of the field is quite complicated in this case, but the on/off characteristic is maintained.

- **Permanent magnets** have the major advantage of being completely autonomous. Their field, as their name indicates, is permanent and do not require any other side-equipment. The downside of this characteristic is that their field cannot be easily modified, which might be a problem in certain cases. Another significant issue is that fabrication of magnets at the micron scale is not simple, either in the top-down or the bottom-up approach.

Another reason why magnetism is becoming so popular is the significant improve in the fabrication of magnetic micro and nanoparticles in suspension. Precisely controlled magnetic particles can be produced with very low dispersion in size (thus, very low variation in their properties). A major advance is the possibility to add biological or chemical functions to these objects. Specific proteins, antibodies or surfactant compounds, for instance, are used to cover the surface of the particles. They can, thus, be rendered stable in a certain medium and, more importantly, reactive to very specific target objects. The applications are numerous, from Magnetic Resonance Imaging (MRI) to nuclear waste treatment. Nanoparticles, in particular, allowed researchers to study a whole new level of phenomena, even inside microscopic biological entities.

More recently, microfluidics has appeared as a very interesting technology for this field. Its numerous advantages made it be even classified as "almost too good to be true"[1]. As expected, many research groups have seen the potential of this emerging technique and started not only to study it as a subject itself, but also to use it as a complement to other subjects, mainly in chemistry, microelectronics and biomedicine.

Microfluidics allowed the manipulation of very small volumes of fluids in a way that is compatible with most of the other techniques of object handling. A powerful research field emerged very quickly. Micro-systems integrating this and other sources of actuation are, today, a significant part of many research laboratories and companies. Their use go from the most fundamental study of chemical reactions and cellular development to the completely integrated and massively produced diagnosis systems.

The expertise of the Institut Néel on the development of high-performance magnetic films was the starting point for this PhD thesis. The numerous partnerships established over the years with biologists and chemists, together with the possibility to enter a new field of research - microfluidics - served as a motivations to create totally integrated and autonomous systems for a vast range of applications. Biological application are privileged, due to the strong interaction with the Ampère Laboratory, in Lyon, France.

This chapter intends to, at first, present a few concepts of magnetism, the basis of this research. Then, microfluidics is introduced and its key characteristics highlighted. A non-exhaustive overview of micro-systems used for particle handling is presented. Systems using different actuation forces are discussed, with a special attention given to those based on magnetic actuation.

Once these concepts and the state-of-art overview are presented, the position of both Institut Néel and G2Elab in the micro-systems and the object handling fields are defined. Based on the collaborations with other laboratories, the ANR EMERGENT project is introduced and the whys and hows of this PhD thesis are clarified.

# 1.1 Magnetism and micromagnets

The magnetic properties of certain materials are known for several millennia. The first registers of the observation of magnetic phenomena date back to 4000 B.C. and are found in Chinese writings which mention *magnetite*. This compound of iron and oxygen ($Fe_3O_4$) is one of the components of lodestone and, when properly magnetized due to an electric discharge from a lightning, is responsible for the ability of this rock to attract iron.

The first applications of magnetism are also very old. Primitive chinese compasses date from around 2500 B.C., while the well-known compass with the floating needle is much more recent, dating of around a thousand years back in our days. The actual relation of the direction of the needle to the Earth's magnetic field is even more recent. It was proposed by William Gilbert in his monograph *De Magnete*, from 1600. Gilbert conducted experiments which explained many characteristics of magnetic materials.

The advances in this field were slow for many years, until the Danish physicist Hans Christian Oersted observed, in 1820, that a compass changed its direction when put near a current-carrying element. The link between electricity and magnetism was established and the discoveries on this new *electromagnetic* domain started a journey which continues until today. André-Marie Ampère and Dominique-François Arago showed a few months after Oersted's observation that a current-carrying wire can be equivalent to a magnet by putting it into a coil shape. Michael Faraday, a British chemist and physicist, studied the electromagnetic phenomena and its relation to light. His experimental discoveries lead to James Clerk Maxwell's unified theory of electricity, magnetism and light.

## 1.1.1 Induction, field, susceptibility, permeability

In vacuum or in air a magnetic field $H$ has the same direction as the magnetic induction $B$. They are both linked by the equation

$$\vec{B} = \mu_0 \vec{H} \tag{1.1}$$

where $\mu_0$ is the vacuum permeability.

Every material has an intrinsic response in the presence of a magnetic field, which is called magnetization. The magnetic induction takes into account both the magnetic field and the magnetization $M$ inside a magnetic material. If this material is isotropic, they are all aligned in the same direction and their relation is expressed by

$$\vec{B} = \mu_0 \vec{H} + \mu_0 \vec{M}. \tag{1.2}$$

The magnetic susceptibility $\chi$ establishes the relation between $M$ and $H$. Based on the susceptibility

$$\chi = \frac{M}{H}, \tag{1.3}$$

equation 1.2 can be rewritten as

$$\vec{B} = \mu_0 \vec{H} + \mu_0 \chi \vec{H} = \mu_0 (1 + \chi) \vec{H} = \mu_0 \mu_r \vec{H} = \mu \vec{H} \tag{1.4}$$

where $\mu_r$ is the relative permeability, defined as $\mu/\mu_0$.

## 1.1.2 Classes of magnetic materials

The susceptibility is an important factor for the classification of the magnetic materials. This dimensionless coefficient can be positive or negative, linear or non-linear. The magnetic materials are usually classified in three main groups: *diamagnets*, *paramagnets* and *ferromagnets*.

*Diamagnetic materials* contain only atoms and molecules which have no net magnetic moment. In the presence of an applied field, their induced magnetization is weak and opposite to the field direction. The susceptibility values are negative, usually in the range of $-10^{-6}$ to $-10^{-4}$ and don't vary with temperature. Diamagnetism is present in all materials, even those containing other types of magnetic materials. Its effects are much weaker than the others and are often negligible. Some common diamagnetic materials used in microsystems are water ($\chi = -9.06 \times 10^{-6}$), silicon ($\chi = -14.0 \times 10^{-6}$), carbon ($\chi = -16.0 \times 10^{-6}$) and copper ($\chi = -22 \times 10^{-6}$). The most diamagnetic natural material is bismuth ($\chi = -175.0 \times 10^{-6}$) which is only defeated by the synthetic hyghly oriented pyrolitic graphite (HOPG) ($\chi = -450.0 \times 10^{-6}$). These materials are the subject of studies concerning stable and actuated magnetic levitation.

The *paramagnetic* behaviour appears when atoms have a net magnetic moment, but these moments do not interact with each other and are free to rotate in any direction. When submitted to an external field, paramagnets have their global moment aligned in the same direction of the field creating a net magnetization, which returns to zero if the field is removed. The magnetization is higher at lower temperatures and decreases as temperature increases. This is due to the thermal agitation of the moments, which tend to be less aligned with the field. The $M(H)$ curve also becomes more linear with increasing temperature. The values of susceptibility for paramagnets are positive and range from $10^{-4}$ to $10^{-3}$. The paramagnetic behaviour of a material can be described by Langevin's equation, which states that the magnetization as a function of the field and the temperature is

$$M = M_0 \coth x - \frac{1}{x} \; with \; x = \frac{\mu_0 m_0 H}{k_B T} \tag{1.5}$$

where $M_0$ is the saturation magnetization at 0 K, $m_0$ is the modulus of the magnetic moment, $k_B$ is Boltzmann's constant and $T$ is the temperature.

*Ferromagnets*, as paramagnets, have a net atomic magnetic moment, but unlike the latter, these moments are strongly coupled together. These coupled moments are spontaneously aligned over large regions called *Weiss domains*. The temperature, in ferromagnets, also reduces the magnetization by thermal agitation of the moments. Ferromagnets, despite of the spontaneous magnetization, can have a zero global magnetization. In this case, each domain is randomly aligned, with no preferential direction. Submitting the material to an increasing magnetic field will align the moments in the same direction, until it reaches saturation. At this point, even if the field is removed, the material will show a global moment due to the preferential orientation of the individual moments. If a field is applied in the opposite direction until saturation and again in the first direction, the magnetization as a function of the field does not follow the same path. This is called *hysteresis* and is what gives magnets so many potential applications. These loops will be further discussed in section 1.1.3.

Ferromagnets are also characterized by their Curie temperature $T_C$, the temperature at which thermal agitation overcomes the coupling interactions and the material loses its specific magnetic characteristics. The susceptibility of ferromagnets usually ranges from $10^4$ to $10^5$.

Figure 1.1 shows characteristic magnetization curves of diamagnetic, paramagnetic and ferromagnetic materials.
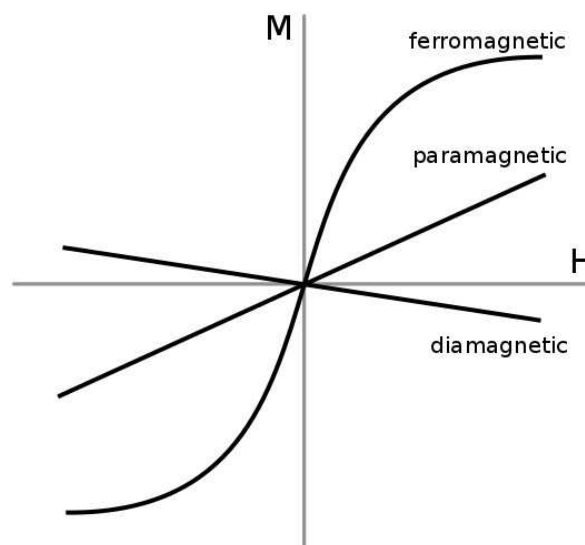


Figure 1.1: Magnetization curves of diamagnetic, paramagnetic and ferromagnetic materials.

## 1.1.3 Hard and soft magnets

The terms *hard* and *soft magnets* come from the analysis of the hysteresis loops of the magnetic materials. Let us, first, properly analyse the magnetic structure of ferromagnets

and their dependance to an applied field. Take a demagnetized ferromagnetic material divided into several randomly oriented Weiss domains. The domains are created to minimize the energy in the material and are affected by defects, inclusions and dislocations. The interfaces between the domains are zones of magnetization reorientation, i.e., transition zones where the moments gradually change from one direction to the other. Felix Bloch, a Swiss physicist, was the first to study the properties of these zones, hence the name *Bloch walls*. The domain walls have an associated energy and can respond to an applied field. Consider the material shown in Figure 1.2, initially dividided in a few domains. An applied field induces a torque on the magnetic moments that tends to force them towards the field direction. The Bloch walls are displaced and the domains which are parallel to the field grow, while the other domains are consumed. Saturation is obtained when all the moments are aligned with the magnetic field.
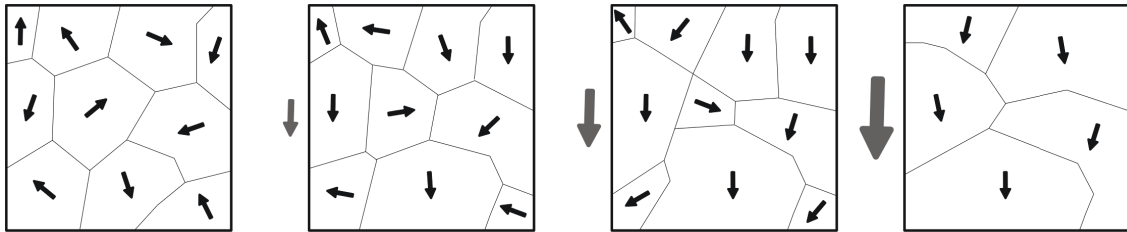


Figure 1.2: Domain walls being displaced by a magnetic field. The increasing magnetic field is represented by the gray arrow.

The saturation state is obtained while the field is being applied. Removing the field causes the magnetization to reduce. In ferromagnets not all the moments reorient after the saturation field is removed. The magnetization remaining at zero field is called *remanent magnetization* ($M_R$).

The field which is necessary to induce a zero global magnetization on the previously saturated material is called the coercive field $H_C$. At this point the domains are aligned with preferential directions and the sum of the moments results in zero magnetization. Hard and soft magnets are characterized by, respectively, high and low coercivities. The $\mu_0 H_C$ values[1] are usually between 0.5 and 2 T for the first and around $10^{-5}$ T for the latter.

Remanence and coercivity are very important extrinsic properties to observe when looking for high-quality magnets. Varying a field between positive and negative values and observing the consequent magnetization or induction generates the hysteresis loops, so appreciated by magneticians. The so-called M-of-H ($M(H)$) or B-of-H ($B(H)$) plots present basically three main quantitative information: the already mentioned $M_R$ (or $B_R$, the conversion between the two of them is obtained from equation 1.2, the coercive field $H_C$ and the energy product $(BH)_{max}$. The hysteresis loop is completed by going to the negative

---

[1]Field and magnetization values are often multiplied by the vacuum permeability and, thus, represented by $\mu_0 H$ and $\mu_0 M$. The advantage is that the unit becomes the Tesla [$T$], which is easier to handle.

| Magnet | $\mu_0 M_R[T]$ | $\mu_0 H_C[T]$ | $BH_{max,th}[kJ/m^3]$ | $T_C[K]$ |
|---|---|---|---|---|
| NdFeB | 0.7-1.3 | 1.0-2.8 | 514 | 585 |
| SmCo | 0.8 | 1.0-3.5 | 220 | 1000 |
| FePt | 0.7 | 1.0 | 407 | 750 |
| AlNiCo | 1.2 | 0.1 | 44 | 1200 |
| Ferrites | 0.4 | 0.3 | 29 | 720 |

Table 1.1: Magnets

and back to the positive saturation fields. Figure 1.3a shows typical hysteresis loops for hard and soft materials.
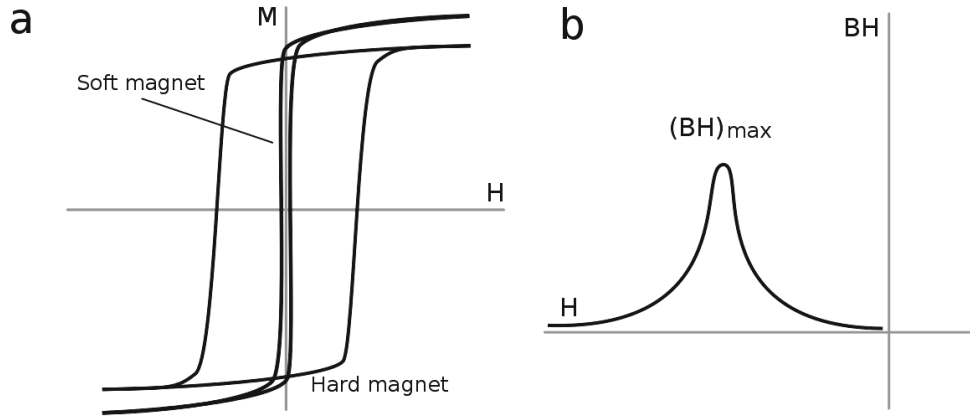


Figure 1.3: (a) Typical hysteresis loops for hard and soft magnets. (b) BH(H) curve showing the highest BH product.

The energy product is calculated from the *demagnetization curve*, which is the portion of the hysteresis loop in the second quadrant. A plot of $BH(H)$ (Figure 1.3b) allows one to identify the point of maximum product, or $(BH)_{max}$. This product gives an idea of the energy a magnet can store. Table 1.1 presents the properties of a few commonly used permanent magnets. $(BH)_{max,th}$ represents the theoretical maximum energy product obtained for each magnetic material.

## 1.1.4 Magnetic particles and the superparamagnetism

Micro- and nanoparticles are used in several domains, from industrial applications to scientific research. Their high surface-to-volume ratio renders these particles especially interesting for the biomedical field. For instance, reducing the radius of a spherical object from 1 mm to 1 $\mu$m yields an increase in surface by a factor $10^6$ while its volume reduces by

a factor of $10^9$. In other words, the surface-to-volume ratio increases by 1000 for a reduction of 1000 in the radius of the object.

The interest of the large available surface with low volume is that specific functional components can be attached to the surface of the particles, allowing their use for labelling, targeting and separation. Yet, the magnetic character of the particles hugely expand their applicability, since remote actuation becomes possible. Nowadays such particles are commonly used for Magnetic Resonance Imaging (MRI)[2, 3], drug delivery [4, 5], hyperthermia [6, 7] and several other applications where a magnetically activated motion can be used. A very important research field and application of magnetic particles is now the High Gradient Magnetic Separation (HGMS), in which objects labeled with these particles are sorted due to magnetic actuation. Non-magnetic (or diamagnetic) particles can also be submitted to a magnetic force, as mentioned before.

Magnetic particles are usually considered to be spherically-shaped objects. Their dimension varies from a few nanometres to several micrometres and the size distribution can be very narrow, depending on the fabrication technique. Usually these particles have a polymeric matrix (polystyrene (PS) or latex) - silicon and silicon oxide are also used - and the magnetic character comes from magnetic materials embedded in it (inclusions). The distribution of the inclusions can follow three main structures. Particles in the nanometre range are usually composed by a magnetic core, which is surrounded by a protective, non-magnetic matrix (see Fig. 1.4a). As the size increases, it becomes more recurrent to see the structure of Fig. 1.4b, with many magnetic inclusions in a spherical non-magnetic matrix. A non-magnetic core surrounded by magnetic inclusions and the whole covered by a protective layer (Fig. 1.4c) is more rarely used[8, 9].
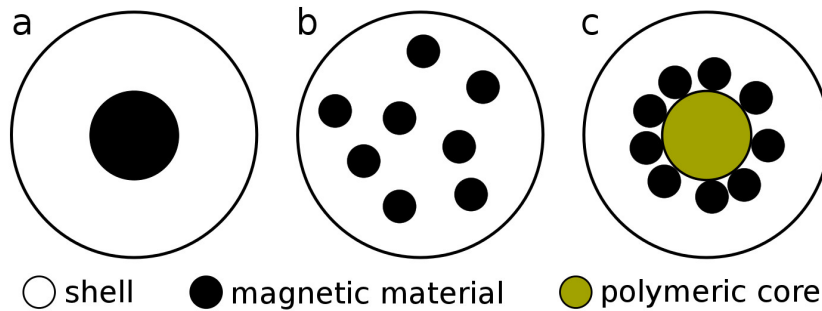


Figure 1.4: (a) Magnetic core, (b) multiple magnetic cores, (c) magnetic particles surrounding a polymeric core.

The shell which protects the inclusions from the environment is often prepared in such a way that a further functional layer can be attached to the particle. This cover layer is usually biological or chemical and is responsible for the interactions of the particles to specific targets, which vary from nano (radioactive atoms, biological molecules, DNA chains) to micro-objects (bacteria, cells). Different particle fabrication and functionalization techniques are available. If more information about it is required, it can be found in the following references: [8], [10].

As regards the magnetic materials incorporated to the particles, the most common are iron and iron oxide - magnetite ($Fe_3O_4$) and maghemite ($\gamma$-$Fe_2O_3$). These materials are interesting for their magnetization due to the magnetic moment of iron, which is the highest among the ferromagnetic transition metals. Nevertheless, iron is very susceptible to oxidation, thus a protective layer is also required for iron particles. This layer can also serve to render iron and iron oxide magnetic particles biocompatible.

*Superparamagnetic* particles are preferred for many applications due to some very interesting properties: high susceptibility and absence of remanent magnetization, which could lead to agglomeration under certain conditions. Superparamagnetism appears in ferromagnetic materials when the grain size is reduced down to a few nanometers (1 - 50 nm, depending on the material). Below this dimensional threshold the material presents a behavior which is similar to paramagnetism. An applied field can orient the grains in any direction and the removal of this field does not leave a remanent magnetization. The susceptibility of superparamagnetic materials is, however, much larger than that of paramagnetic materials.

The superparamagnetic behavior occurs due to the influence of temperature on the magnetization when the grain size is smaller than a critical magnetic domain size. The thermal energy induces a random switch of magnetization direction of the small particles. The magnetic anisotropy of most particles induces, usually, two stable orientations. The average time between two orientation switches is called *Néel relaxation time* $T_N$ and depends exponentially on the volume of the particle. Obviously, large grains can have a $T_N$ of years and are not superparamagnetic. In the case of the nanometric grains this time is typically in the nanosecond range.

For iron oxide at room temperature the limit in dimension for a particle to become superparamagnetic is around 40 nm [11]. The comercial superparamagnetic *micro*particles are usually composed by many superparamagnetic *nano*inclusions embedded in a micrometric matrix.

The superparamagnetic behaviour can also be modeled by the Langevin function (equation 1.5). This behaviour is characterized by a high susceptibility at low magnetic fields, followed by saturation at a few hundreds of $mT$. As previously mentioned, the magnetization of a superparamagnetic material returns to zero when the field is removed, as observed in Figure 1.5. A more detailed model of the particle magnetization is given in Chapter 4.
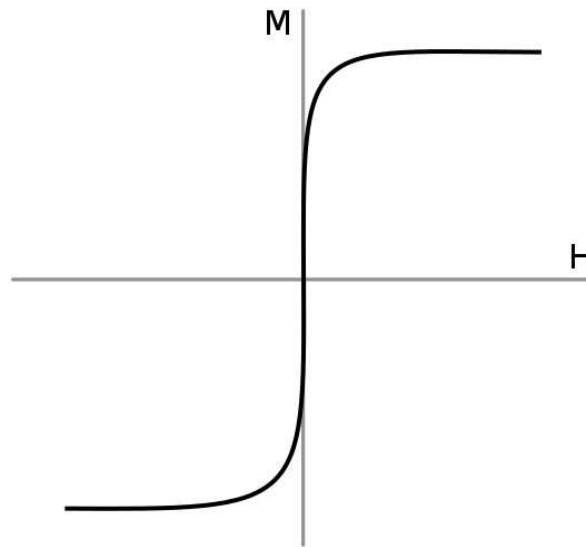
Figure 1.5: Typical magnetization curve for a superparamagnetic material.

Magnetism and magnetic particles become even more interesting for a number of applications when coupled to microfluidics. The possibility to act on the flow of a liquid solution while acting on the particles themselves render magnetic labeling a major technique, for instance, for the study of bacteriologic processes and cell sorting.

## 1.2 Microfluidics

One of the most simple and precise descriptions of what microfluidic is was given by Whitesides in 2006: "It is the science and technology of systems that process or manipulate small amounts of fluids ($10^{-9}$ to $10^{-8}$ litres), using channels with dimensions of tens to hundreds of micrometres" [1]. In this same Nature paper Whitesides mentions that, despite of the many advantages it offers, microfluidics is not widely used. It rapidly changed in the following years, as indicates ISI Web of Knowledge: around 100 papers citing microfluidics in 2000 against more than 3000 papers in 2010. Today microfluidics is widely spread and its applications go from simple channels to very complex systems integrating electrical, mechanical, and optical parts.

What makes microfluidics so interesting are its fundamental characteristics, which bring many advantages:

- Very small amounts of liquid: very low waste of materials, which is very interesting for precious samples.

- Fast reactions: due to the small volumes, reactions don't depend on the time-consuming mixing over large distances and can occur in a controlled and fast fashion.

- Laminar flow: (discussed further in this chapter) a great advantage of the scale reduction. Controlled mixing can be performed or mixing can be easily avoided. The fluid flow can also be easily predicted and modeled.

- Polymer-based devices: microfluidics is compatible with several polymer-based technologies, which makes it an easy, fast and cheap alternative to glass or silicon.

Many other advantages - such as the possibility to functionalize the polymeric surfaces of a microfluidic channel and the small environmental footprint of these devices - can be derived from the list above. The list is not exhaustive, as this field is constantly evolving with different materials, fabrication methods and applications.

## 1.2.1   Scaling laws and the continuum hypothesis

The first thing that pops out when analyzing the properties of microsystems is the surface-to-volume force ratio. Surface forces are proportional to $l^2$ - where $l$ is a characteristic dimension of the system - and volume forces are proportional to $l^3$. Analyzing the ratio of these forces yields

$$\frac{l^2}{l^3} = l^{-1}; \ if \ l \longrightarrow 0, \ \frac{surface forces}{volume forces} \longrightarrow \infty. \tag{1.6}$$

Put in words, volume forces are usually predominant at the macroscale, while for microfluidics, surface force effects and surface interactions are essential.

Microfluidic devices are supposed to handle *fluids*, i.e. liquids or gases. The interactions in a liquid are much more complex, since each molecule is always surrounded by many others. At short ranges the molecules can be considered ordered around determined positions. Nevertheless, as opposed to solids, in which the thermal oscillations makes atoms move slightly around a precise position in a lattice, the oscillations in liquids make them able to flow. Even though fluids are composed by atoms and molecules, for most applications in microfluidics they can be analyzed as a continuous entity. This *continuum hypothesis* renders much easier the analysis and prediction of fluid properties and dynamics. The hypothesis is valid up to a maximum volume, above which the environment can change the local properties of the fluid, e.g. a force applied on a liquid can locally change its density [12].

## 1.2.2   Reynolds number and flow regimes

Microscopic fluid flows are typically very different from the day-to-day macroscopic flows (washing your hands in the sink, pouring orange juice in a glass). The reduced dimensions of a microfluidic channel induce a modification in how the fluid behaves: the common turbulent regime becomes in this case a smooth laminar regime. These regimes are characterized by a distinct Reynolds number, which is simply a relation between inertial and the viscosity forces.

The dimensionless Reynolds number comes from an analysis of the Navier-Stokes equation, represented below, which describes the evolution of a velocity vector field. Velocity is represented $\vec{u}$, $t$ is the time, $\rho$ and $\mu$ are the density and the viscosity of the fluid and $p$ is the pressure.

$$\frac{\partial \vec{u}}{\partial t} + (\vec{u} \cdot \nabla)\vec{u} = -\frac{1}{\rho}\nabla p + \frac{\mu}{\rho}\nabla^2 \vec{u} \tag{1.7}$$

The viscous and inertial effects can be analyzed by taking a characteristic velocity $U$ and a characteristic length $L$ and scaling the terms of the equation. One can observe that $\vec{u}$ scales with $U$ and $t$ scales with $\frac{L}{U}$ (advection time scale). It implies that the unsteady inertial term $\frac{\partial \vec{u}}{\partial t}$ scales with $\frac{U^2}{L}$. The spatial derivative $\nabla$ scales with $\frac{1}{L}$, thus, the non-linear inertial term $(\vec{u} \cdot \nabla)\vec{u}$ also scales with $\frac{U^2}{L}$. Finally, the viscous term $\frac{\mu}{\rho}\nabla^2 \vec{u}$ scales with $\frac{\mu U}{\rho L^2}$.

The inertial-to-viscous ratio, i.e. the Reynolds number is, thus, given by:

$$Re = \frac{ul\rho}{\mu}. \tag{1.8}$$

A turbulent regime occurs typically when the Reynolds number is higher than 4000. In this case the inertial forces are predominant and the flow is characterized by a chaotic movement of the fluid. The mean velocity is "forward", so the water comes out from the hose and you can water your garden, but inside the hose the water streamlines are going in every direction permanently. Figure 1.6a schematically shows how a fluid flows inside a channel in a turbulent regime.

If the size of the channel is sufficiently reduced, the *laminar regime* is achieved ($Re < 2300$). In this case the streamlines become organized and regular, as shown in Fig. 1.6b. This type of flow regime can be compared to a set of playing cards piled up on a table. Tilting the table makes the cards slide above each other with different velocity, but they remain parallel as they move. In other words, the fluid particle follows a determined streamline along the channel and is not constantly mixed with the neighbouring fluid particles.

Below 4000 and down to around 2000 the flow regime is characterized by a transient state, which is both turbulent and laminar. Viscous and inertial effects occur concurrently, the first more concentrated around the edges of the pipe or tube, and the latter on the zones not affected by the boundary effects.
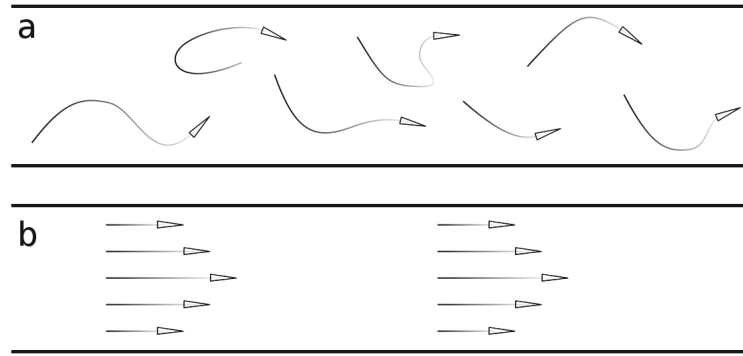
Figure 1.6: (a) Turbulent flow. (b) Laminar flow.

Typical microfluidic devices induce Reynolds numbers around 1, frequently even less. It means that going to the micron scale rapidly reduces the mass on the system, thus reducing inertial effects. On the other hand, surface and viscous effects quickly become important. The result is a very smooth, predictable laminar flow inside the microfluidic channels.

The parabolic velocity profile observed in laminar regimes comes from the effect of the edges of the channel on the flowing fluid. In a turbulent regime the effect of the *boundary layer* does not "penetrate' on the fluid significantly. Inversely, the boundary layer progressively penetrates on a laminar flow, resulting in a modification of the velocity profile seen in Figure 1.7. Once the effects of all the edges of the channel are stable, a continuous parabolic profile is observed.
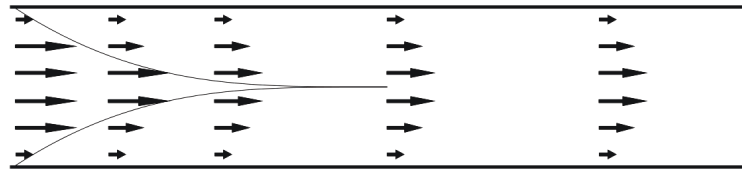


Figure 1.7: Influence of the boundary layer on the fluid flow.

Turbulent regimes present a few advantages, such as the possibility of mixing liquids at high speed and homogeneously, while in laminar regime one has to count on interdiffusion between the liquids - which is often a very slow process - or on adapted microchannels in which vortices or perturbed streamlines are present. Nevertheless, the laminar regime has a major advantage, possibly the one responsible for its succes among microdevices: predictability. Laminar flows can be described mathematically and simulated with very high precision. In this manner, microfluidic devices are modeled and optimized before being fabricated. Controlled chemical reactions, interdiffusion of liquids and the trajectory of particles can be precisely predicted, even in devices integrating multiple techniques, i.e. microfluidics, electricity, magnetism. [13]

### 1.2.3 Digital and continuous flow microfluidics

Two main techniques of fluid manipulation are used in microfluidic devices. The first one, called *digital microfluidics*, is used to manipulate isolated amounts of fluid, or *droplets*. The advantages brought by this technique are the significant reduction in the required sample volume and the possibility of analyzing many samples at once. Precise amounts of liquid can react with each other and be observed at high speed. However, this technique often requires a complex apparatus.

The second technique, *continuous flow microfluidics*, is the most widespread today. It consists simply on passing the fluid continuously through the microchannel. The fluid displacement is induced, in most cases, by a difference in pressure between the inlet(s) and the outlet(s) of the channel. Apart from this *pressure-driven flow*, other two common methods are the *electrokinetic flow*, where the fluid flows due to an applied electric field, and the *capillary flow*, where capillary forces induce the movement. This last method has the drawback of only working with very low channel dimensions and while the channel is not completely wet, but also the advantage of handling very small amounts of liquid.

Pressure-driven flow is used for all the systems used in this research. The difference in pressure is achieved mostly by applying a higher pressure on the inlets of the channel. However, for certain applications, a lower pressure is applied on the outlets (the liquid is pumped out).

### 1.2.4 Flow cytometry

*Flow cytometry* appears in a significant part of scientific papers dealing with micro-object handling, as it can be seen in the context overview of Section 1.3. This technique is today very reliable for counting and separating objects in the microscale at a very high speed. It is used in several domains, mainly in cell biology and medicine. The equipment required to perform flow cytometry is complex and expensive, but the principle can be simplified as presented below.

The first important point to notice is that flow *cyto*metry - cyto comes from the greek and stands for *cell* or *hollow*, but is mainly used for animal or plant cells - is not only used to sort cells. It can be used with molecules, particles and other objects in liquid solution. In fact, flow cytometry is not used only to sort these objects. Some flow cytometers are not even capable of performing sorting, in spite of the wide use of the name FACS (which is an acronym for Fluorescence Activated Cell Sorting and, actually, a trademark). This technique is sometimes used simply to count distinct populations of objects in a same solution. [14].

A flow cytometer is composed by three main parts:

1. A source of focused light, usually a laser;

2. A fluidic system capable of aligning the objects of study in a stream;

3. An electronic part to collect and analyze the signals.

The basic scheme is shown in Figure 1.8. The liquid solution containing the objects of interest passes through the fluidic system of the equipment and is focused in a single stream. The goal is to obtain a stream sufficiently thin so that the objects flow separately. In a basic configuration, a laser irradiates the objects and is blocked/diffracted in a characteristic fashion depending on the object's content and properties. Two signals are collected: the transmitted beam at low angles (0.5 - 10°) from the axis (forward scattered, FSC) and the refracted beam at 90° (side-scattered, SSC). The FSC beam gives the object radius. The second beam is scattered due to the inhomogeneities of the object (the nucleus of a cell or inclusions in a latex particle), so it gives an idea of the content of the object. Some flow cytometers are equipped with multiple laser sources which are used to excite specific fluorescent groups tagging the objects. The electronic part is responsible for collecting these signals and transmitting them to the analyzer.
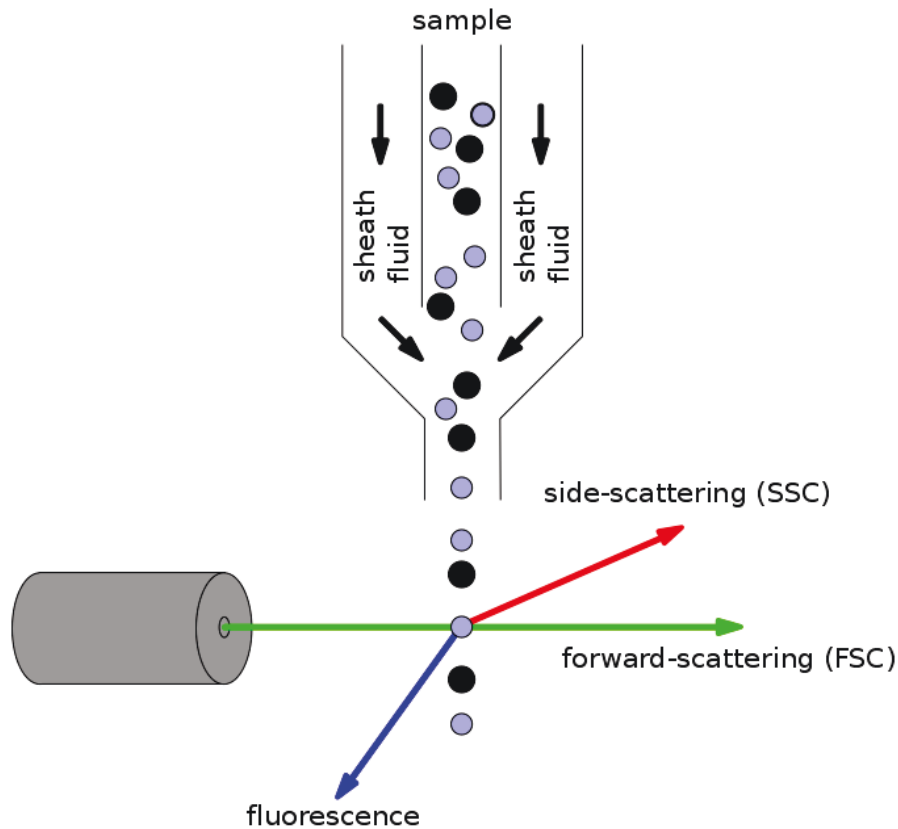


Figure 1.8: Schematic of the flow cytometry principle.

Flow cytometers work in a multiparameter fashion, i.e., all the informations - size, granularity, fluorescence - are collected for each object. It facilitates the discrimination of several populations when some parameters are similar. Consider, for instance, two populations of cells in a solution, one population is tagged with fluorescent magnetic nanoparticles, while the other is not modified. Analyzing FSC×SSC plots for these populations may result in superimposed groups of data, since the size and the granularity

are not so different (see Figure 1.9a). Plotting the fluorescent signal versus the granularity (Fig. 1.9b) or versus the size (Fig. 1.9c) will result in two very distinct populations, since the non-tagged group shows no fluorescence signal, while the signal for the tagged group is very strong.
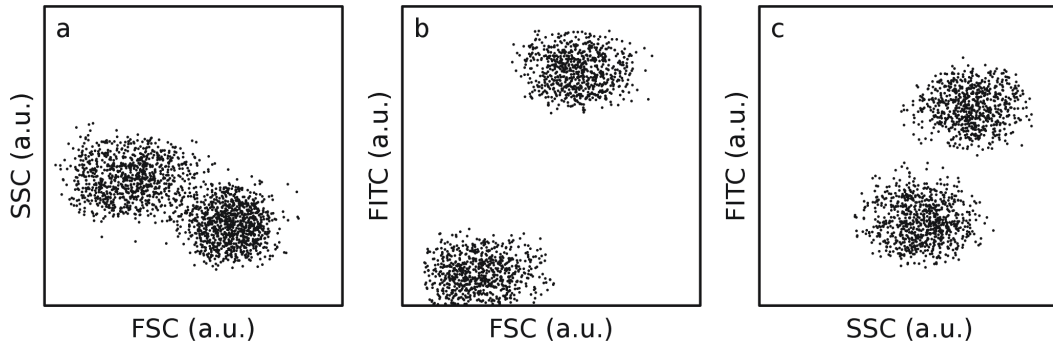


Figure 1.9: Two groups of objects analyzed by flow cytometry. The groups are superimposed in the (a) FSC×SSC plot, but can be better discriminated if one of them is tagged with a fluorescent agent (FITC), as shown in (b) the FSC×FITC plot and (c) the SSC×FITC plot.

The treatment and analysis of the data is often complex, due to overlapping of fluorescence spectra and the need of compensation factors. In the case of FACS equipments (those actually performing sorting), the liquid stream is turned into separate drops of liquid, which are then electrically charged in order to be deviated by charged plates and collected into different recipients.

## 1.3    State of the art: handling micro-objects

As mentioned in the introduction of this chapter, not only magnetophoresis is used to handle objects at the micron scale. Other forces coming, for instance, from sources as simple as the perturbations on the streamlines of a microfluidic flow caused by the channel structure itself are used.

Hydrodynamic effects can be used to change particle trajectory in a microfluidic channel. This is maybe the simplest actuation technique, since it can be based only on the shape of the channel. The perturbations on the streamlines caused by the shape of the channel are responsible for the force acting on the particles. Di Carlo et al. developed a micro-channel configuration which allows particles to be focused on its center due to these effects [15]. The particles enter the channel randomly dispersed and, as they move through the curves of the channel, are focused both longitudinally and laterally, i.e. one single line of particles is obtained (see Fig. 1.10a). The group attributes particle focusing to lift forces in the cases where inertial effects are significant.

Similarly, but in a more controllable, yet more complex fashion, Wang et al. [16]

developed a system which deviated the trajectory of a particle by a change in the fluid flow. A piezoeletric transducer coupled to the micro-channel is responsible for the control of a bubble produced on the edge of the channel (see Fig. 1.10b). Changing the size of the bubble induces a modification in the streamlines around it, thus deviating a particle in its vicinities. Particle separation is demonstrated with high precision using this system.
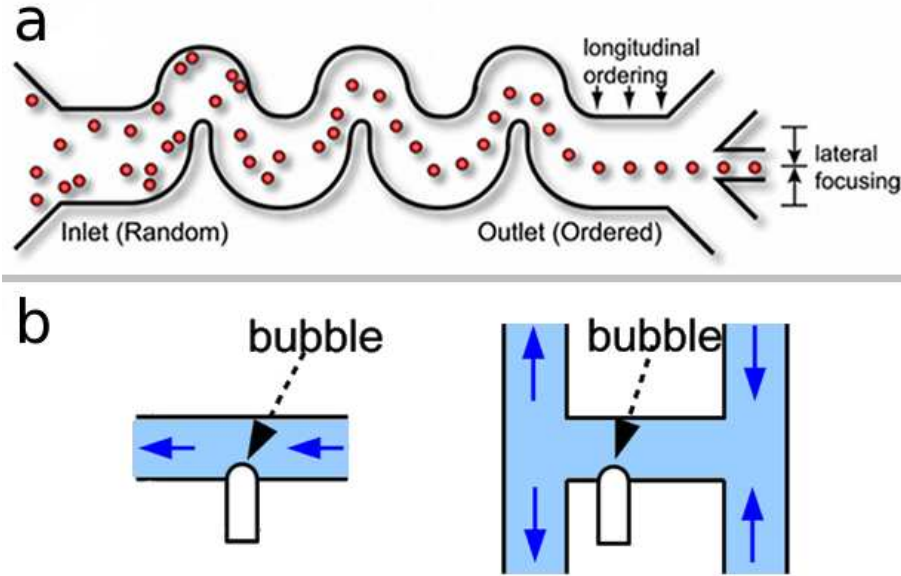


Figure 1.10: (a) Particle focusing using hydrodynamic forces [15]. (b) Particle deviation by a modification in the streamlines caused by bubble controllable in size[16].

Acoustic forces are also an option for contactless actuation. Considering the case of acoustic actuation with microfluidics, the basic principle is to generate standing sound waves in the channel. These waves can be produced in such a way that nodes and anti-nodes are generated at different points of the channel. Once an object enters the channel a radiation force acts on it, pushing it to a node or an anti-node, depending on various factors (acoustic properties of the object, its density and compressibility, etc.). This radiation force is actually a sum of two forces: a primary force coming from the standing wave and a secondary force - orders of magnitude smaller and only significative at small distances - coming from the sound waves scattered by the object [17].

Adams et al. used this technique to sort particles of different sizes [18]. In this paper the group reports on the separation of three sizes of particles, using the system shown in Figure 1.11a. The particles enter the microfluidic channel by its extremities, while a buffer solution is inserted at the center. The first separation occurs in the beginning of the channel, where the whole solution is submitted to an acoustic radiation force. Different responses to the force are presented by each type of particle. The acoustic forces focuses two groups of particles in the center of the channel, while the third group is slightly deviated and collected in the low-pass outlets. The deviated particles are then guided to the extremities of the channel,

a buffer solution being inserted in the center, and submitted to a second acoustic radiation force, which is different in this stage and focuses only one group of particles in the center of the channel. Outlets conveniently disposed in the end of the channel collect each group of particles. Adams et al. also used acoustophoretic forces combined with magnetophoretic forces to separate three types of particles in another system, reported in [19].
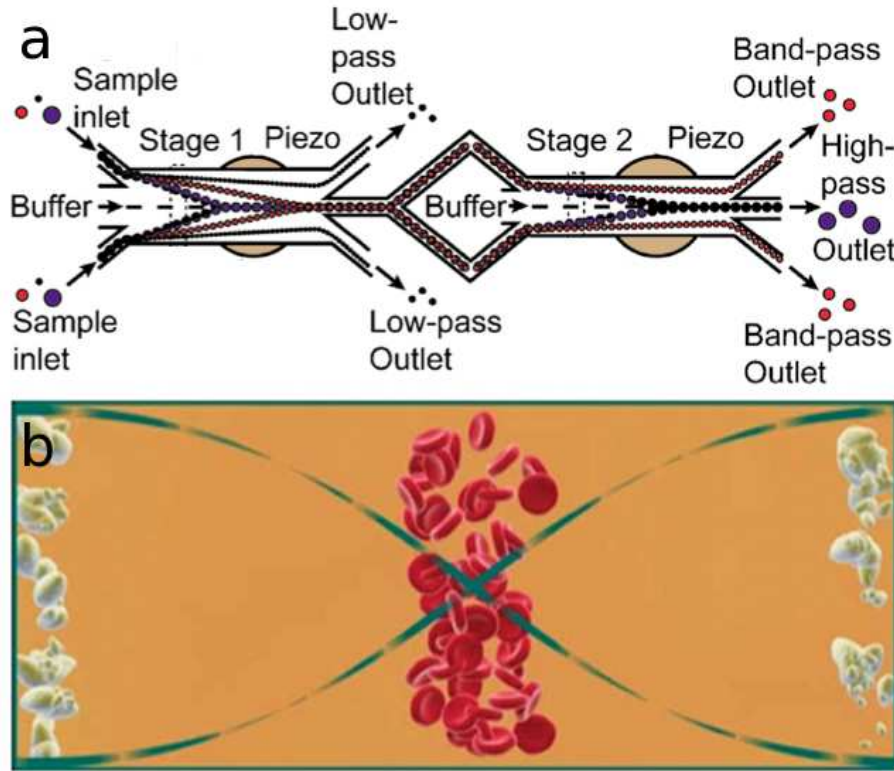


Figure 1.11: Acoustic forces used to sort (a) microparticles [18] and (b) reb and white blood cells [20].

Another work developed by Petersson et al. used acoustic forces to separate red blood cells from lipid particles in whole blood [20]. In this case, the acoustic radiation force concentrated the red blood cells on the nodes of a standing acoustic wave, while the lipids were guided to the anti-nodes of the wave. A schematic of the separation mechanism is reproduced in Fig. 1.11b. The objects were then collected by three outlets in the end of the microchannel.

Dielectrophoretic (DEP) forces are also widely used for continuous flow sorting. In dielectrophoresis and uncharged object can be displaced due to a force generated by an electric field gradient. This external field will polarize the dielectric material, which will have, thus, an internal electric field. The internal field can be represented by a dipole which is aligned with the external field at a point. As the object moves in the field gradient, a force acts on it, deviating its trajectory [21].

Kim et al. reported on the use of this force for the separation of mammalian cells [22]. The system so used contains a first set of electrodes which focus the cells at a certain point of the channel and a second set which deviates the cells according to their size, as shown in Figure 1.12a. With this technique, cells in different cycle phase could be sorted, since to each phase corresponds a cell dimension.
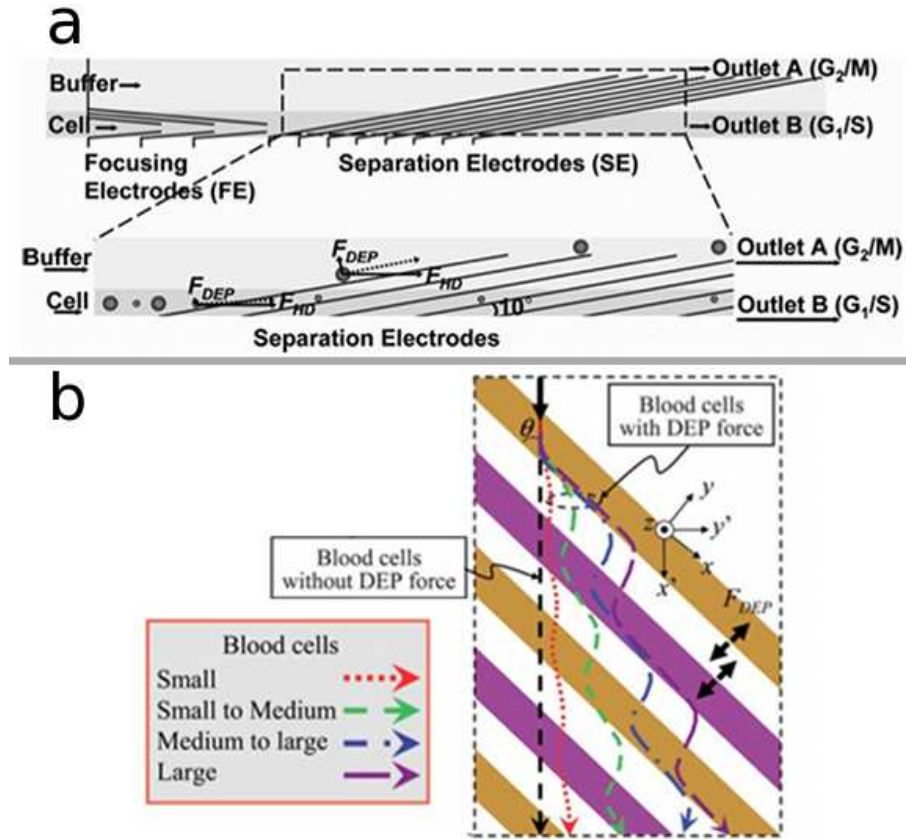


Figure 1.12: (a) Particle focusing and deviation using dielectrophoresis [22]. (b) Sorting of particles based on the dielectric character [23].

Han et al. used dielectrophoresis to perform separation of red and white blood cells [24]. In this work separation occurs due to a difference of sign in the force acting on each type of cell resulting in simultaneous positive and negative DEP.

In another work [23], the group reports on the separation of blood cells according to their size, using the same type of actuation. Figure 1.12b, adapted from Han's article, shows a microfluidic channel with two sets of electrodes aligned with a certain angle related to the fluid flow. Blood cells are differently deviated by the electrodes and can be collected in independent outlets further in the channel. The DEP force becomes stronger as the cell size increases.

The optical force created by a light source - a laser, for instance - can also be used to

deviate objects. Both angular and linear momenta can be transferred to a micro-particle, for instance, when the latter is irradiated. [25]. This optical force can be separated into two components: the gradient force (or dipole force) and the scattering force. These work both with micro and nano-particles and can be computed, as shown by Rohrbach and Stelzer in [26, 27], if the particle size is significantly different to the wavelength of the irradiating light.

Wang et al. reported on the separation of mammalian cells in microfluidic channel using optical switching in [28]. Particle deviation was reported later on by Hoi et al. [29]. Their technique consists of flowing the micro-particles through a channel, and acting on them by means of a laser beam which is focused at a certain point inside the channel. As it can be observed in Figure 1.13, the particles can be deviated towards an outlet which is positioned at a certain angle related to the main channel. The amount of deviated particles can be adjusted by controlling the angle of incidence of the laser.
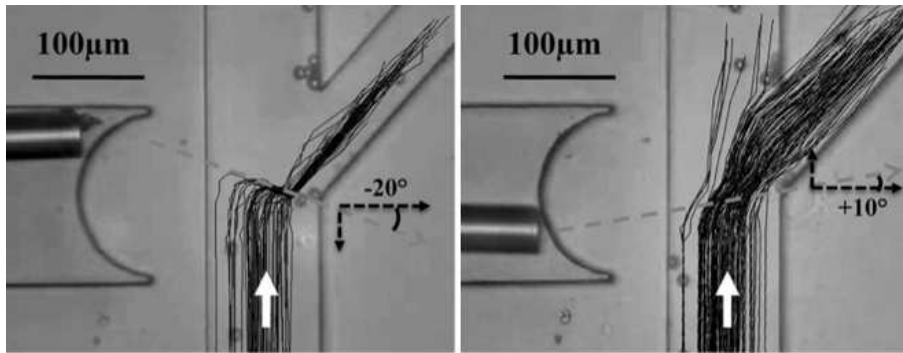


Figure 1.13: Control of particle trajectory using optical forces [29].

### 1.3.1 Magnetic flux sources

As previsouly discussed, three types of magnetic flux sources are used to perform magnetophoresis (MAP) of micro and nano-objects: permanent magnets, electromagnets and soft magnets. In this section an overview of recent publications on magnetophoresis using these three methods is given. It is not an exhaustive overview, for it intends simply to give an idea of materials and methods used nowadays (in particular MAP coupled to microfluidics) and for this research domain is constantly evolving.

Permanent magnets at the macro and at the micro-scale are treated here as two different types of magnetic flux sources. One can deduce that the physics behind both of them is the same, which is right. The discrimination here has two purposes: to stress that the constraints in fabrication methods for these two types of magnets are very different; and to emphasize that great advantages of permanent magnets for micro-object handling are only observable with magnets at the micro-scale.

*Bulk permanent magnets*

Permanent magnets at the macro-scale (bulk) were the first sources of magnetic field to be combined to microfluidic channels in order to attract magnetic particles. The ease to produce such sources of field in different shapes and sizes and to integrate them to the devices, combined with the high magnetic field created by the rare-earth permanent magnets, was decisive for their success on the field of magnetic separation.

As it will be discussed in Chapter 4, in order to generate a significant magnetic force on an object, both high magnetic field and field gradient are required. Bulk magnets generate intense fields at a large distance, compared to the $\mu$m- or mm-sized fluidic channels. Their highest magnetic field gradients, however, are restricted to the edges of the magnet, and are often not so consequent inside the microfluidic channel, depending on magnet-channel configuration.

*Soft magnets*

Soft magnets are one of the most developed domains for HGMS. Basically, the soft magnets used for MEMS are the materials which show a significant magnetization only when polarized by an external magnetic field. In the absence of the polarizing field, these materials create virtually zero stray fields. The possibility to switch the field "on and off" is one of the most interesting aspects of this type of field source. Another important factor for their popularity is their compatibility with standard silicon fabrication techniques.

As regards electromagnets, which also present these two characteristics, soft magnets have two other advantages: no Joule heating while generating a magnetic field; and no need of external power sources, in the case the polarizing field is produced by a permanent magnet. Also, the bias field used to polarize the soft elements is often useful to saturate superparamagnetic particles used to label the objects of interest, for instance.

*Electromagnets*

Electromagnets are widely used as a source of magnetic field to remotely act on magnetic objects. The scale of the electromagnets in such applications varies from big Helmholtz coils used to act on microscopic bacteria to micro-coils built below microfluidic channels.

Many advantages related to such field sources made them so attractive to research and industrial applications. Turning the magnetic field "on and off", as in the case of soft magnets, is obviously very important. Another main factor for choosing electromagnets is the possibility to modulate the magnetic field simply by adjusting the current they conduct. Simulations of the magnetic field generated by current-carrying elements can be performed today with a very high precision and the devices using this technique are easily optimized and tested.

In the case of soft magnets which are polarized by a bulk external field, the ensemble of the elements is polarized at once. It may be a problem in some cases where localized actuation is required. This problem is easily overcome with electromagnets, since a set of current-carrying element can be designed in such a way that they can be independently activated when needed.

A major inconvenient for the use of electromagnets is Joule heating. When a continuous and/or intense magnetic field is required, handling the generated heat has to be a priority. The situation becomes even more critical if working with biological entities, which are often sensible to variations of temperature.

*Permanent micro-magnets*

Magnetic manipulation devices including permanent micro-magnets are not as developed as the other devices due, mainly, to the difficulties related to the fabrication and integration of high-quality magnets at the micro-scale. Shape control and magnetic properties are often exclusive, which lowers the performance of the devices.

These field sources are, however, very interesting for micro-systems. The autonomy of permanent magnets - no need of a power source or an external field - is especially useful for lab-on-chip devices and point-of-care applications. Also, the stray field created by these magnets is restricted to the region of interest, which makes them suitable for integration into micro-devices or use with other equipment, such as microscopes.

Micro-magnetic flux sources share the disadvantages of the bulk magnets: no "on/off" possibility and no real-time modulation. It will be shown in Chapters 4 and 5, however, that these disadvantages are not a limiting factor to the development of very precise and efficient continuous flow cell sorting devices.

## 1.3.2 Magnetophoresis: capture and release

The most evident application of magnetic flux sources in micro-object handling is capturing. All the sources cited in the previous section can perform this function. Release, on the other hand, is easily performed with electromagnets and soft magnets, but physically removing the flux source is required in the case of permanent magnets.

One of the earliest works in magnetic capturing using bulk magnets was reported by Miltenyi in [30]. In this work, a Magnetic Cell Sorter (MACS) from Miltenyi Biotec is used to separate cells labeled with magnetic particles from non-labeled cells. The schematic in Figure 1.14a shows the three basic steps of the MACS technology: the objects of interest are labeled with magnetic particles; the solution passes through the MACS Column, in which the labeled cells are captured by the magnets and the non-labeled cells are collected on the outlet of the column; the labeled cells are removed from the action range of the magnetic field and collected.
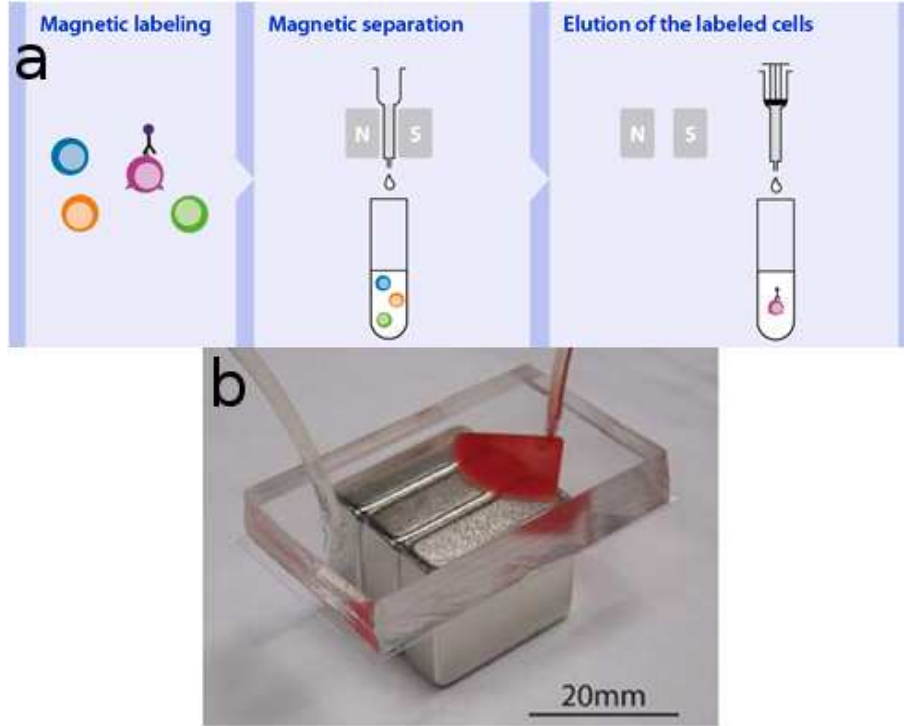
Figure 1.14: (a) Basic principle of the MACS(R) Technology: Label, separate and collect. Picture from the Miltenyi Biotec website [31]. (b) Microfluidic system integrating a bulk permanent magnet [32].

Hoshino et al. developed microfluidic systems in which bulk magnets with antiparallel magnetization are disposed side by side in order to create a higher field gradient[32]. This system, shown in Fig. 1.14b, is used to capture magnetically labeled cancer cells and to observe them inside the microfluidic channel.

The same idea (blocking/unblocking particles) have been used by many other research groups to separate micro-objects. Bulk permanent magnets have been also used, for instance, to give magnetically labeled cells a specific spatial arrangement[33] and to create hair-like structures of magnetic particles [34].

A schematic of the attraction of magnetic objects above soft magnetic elements is shown by Tseng et al. in [35], and reproduced in Fig. 1.15a. A macroscopic source of magnetic field polarizes micro- or nanoscaled soft magnetic elements, which generate both fields and field gradients that attract the round magnetically labelled objects. These elements have been widely used to capture magnetic particles, to concentrate them in determined locations and separate them from mixed solutions [36, 37, 38, 39, 40].

Guo et al. have shown in [41] the standard steps used to capture and release magnetic particles. The four frames shown in Fig. 1.15b present sequentially: polarized square patterns produced on a soft magnetic material, with a microfluidic channel above them; magnetic microparticles captured by the magnetic elements; the polarizing field is removed and the captured particles start to unpin; the system no longer holds magnetic particles.

Separation by magnetic/non-magnetic character can be done using this technique, which is basically the one shown previously with bulk magnets.
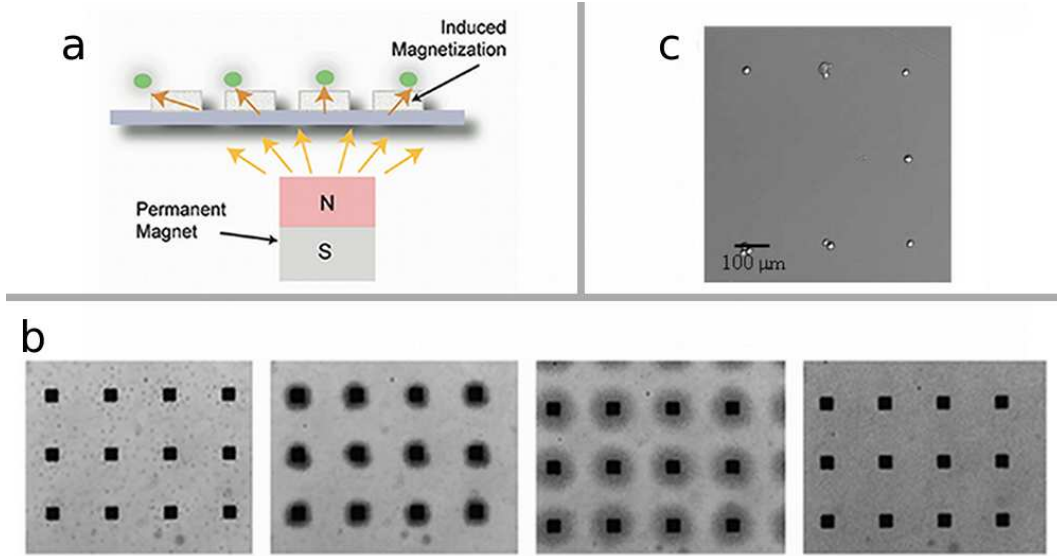


Figure 1.15: Attraction of magnetic particles with soft magnets performed by the groups of (a) Tseng [35], (b) Guo [41] and (c) Ino [42].

The capture/release approach has been also used for biological studies [43, 35]. Ino et al., for instance, developed a method of organizing magnetically labelled cells based on microstructured pilars produced on soft iron [42]. At certain conditions, a single cell can be trapped above each pillar and individually studied. Fig. 1.15c shows cells above and centered to magnetic pillars.

Electromagnets at the macro-scale can be used to act on microscopic bacteria. Such work is reported by Kim et al. in [44]. In this work the displacement direction of magnetotatic bacteria[2] is artificially modified by the magnetic field created by a Helmholtz coil.

In the microscopic scale many works have been developed in the optimization of micro-coils and micro-wires and their applications to particle trapping. Ramadan et al. presented, for instance, different arrangements of micro-wires which can be integrated to micro-devices, especially for biological manipulation [45, 46]. Figure 1.16a shows some configurations developed by the group and the resulting particle capture.

Smistrup et al. used the same approach to develop systems in which magnetic particles are captured and released above electromagnets inside microfluidic channels [47, 48, 49]. In this case, dynamic simulations were used to determine the relation between the initial particle position inside the channel and its capture position. Figure 1.16b shows a cross-section of

---

[2]Magnetotatic bacteria are able to produce magnetic nanoparticles which are disposed in line and align with the Earth's magnetic field. These bacteria are, thus, able to follow a precise direction in order to find their best living condition

the microfluidic channel which represent the initial positions of the particles. The length of the channel is represented by $L$.
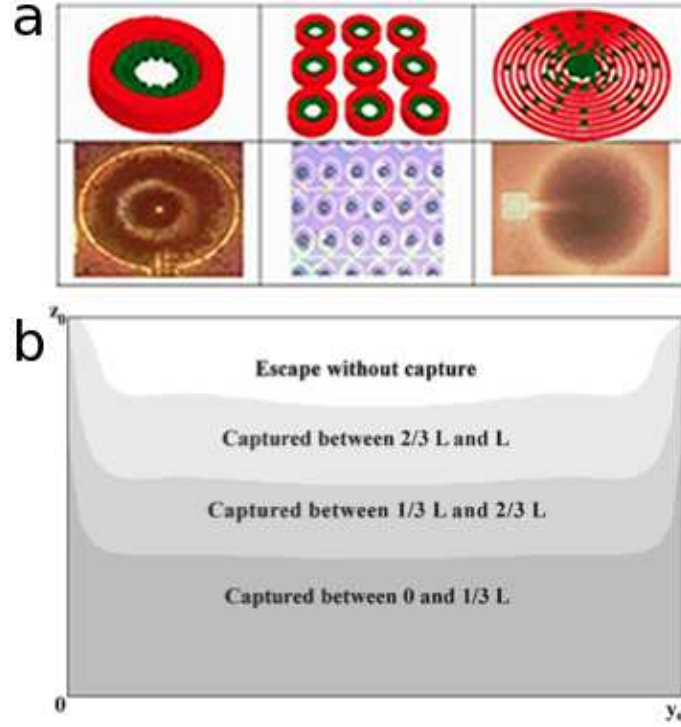


Figure 1.16: (a) Microcoils used to position magnetic objects. Upper and lower rows show, respectively, the schematic of the coils and the actual results [45]. (b) Representation of the cross-section of a channel showing the positions of particle capture along the length of the microfluidic channel. [47].

Rostaing et al. developed a system in which the position of particles can be changed by passing a current on different sets of wires[50]. It allows concentration and mixing of particles and is very interesting for biological applications.

Few works have been reported concerning permanent micro-magnets and microfluidics. Yellen et al. have reported the possibility of positioning non-magnetic particles above arrayed magnetic patterns with high precision [51]. Figure 1.17a shows non-magnetic, fluorescent particles arrayed in precise positions due to the action of magnetic fields created by both the micro-magnets and an external electromagnet on magnetic nanoparticles dispersed on the solution. In another work, the displacement of a magnetic particle above a similar magnetic pattern was reported, when varying the external applied field [52].
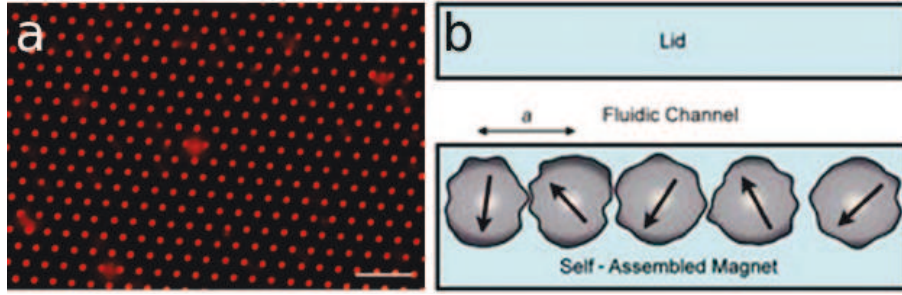
Figure 1.17: (a) Magnetic particles positioned above an array of permanent micro-magnets [51]. Self-assembled NdFeB grains disposed below a microfluidic channel [53].

Issadore et al. used micrometre-sized NdFeB grains to create high magnetic field gradients close to a microfluidic channel [53]. A schematic of the micro-fluidic/micro-magnets system is reproduced in Fig. 1.17b. The NdFeB grains are suspended in uncured PDMS and self-assembled in the presence of an external field. The PDMS is then cured and a microfluidic channel is built above the magnet array. The system was used to sort magnetic/non-magnetic particles and labelled/non-labelled cells with high purity.

Magnetic particle handling with ferromagnets has been reported without microfluidics. Several groups have used micro-scaled magnetic tracks to manipulate single magnetic micro-particles, which are trapped above the domain walls of the tracks. These walls are controllable in real time and can be displaced, with a consequent movement of the particle. Publications on the development of these systems as well as particle manipulation can be found in [54, 55, 56, 57].

### 1.3.3 Magnetophoresis: continuous guiding

Particle capture and release can be performed with relative ease. Continuously guiding and, in particular, sorting particles with microfluidics, on the other hand, can be a much more difficult task. A good control of the attraction force, as well as a fine balance between magnetic and drag forces are required. Numerous successful attempts of continuous flow magnetic cell sorting have been reported using bulk permanent magnets, soft magnets and electromagnets, as shown below.

The group of Pamme designed a system combining microfluidics and a bulk permanent magnet, in which the goal is to guide objects towards different outlets according to the magnetic label. Figure 1.18a shows a schematic of the system. One channel inlet is used to pump in the liquid solution containing the objects of study while a buffer solution is pumped in the other inlets. Notice that the position of the magnet is in the opposite side of the main inlet. The outlets are used to collect the solution containing the particles which are separated by label. This system has been used to sort magnetic particles based on their susceptibilities [58]; cells labeled with magnetic particles based on magnetic moment and particle size [59]; magnetic particles based on the variation of magnetic response in temperature [60]; and different types of cells, based on their endocytotic capacity [61].
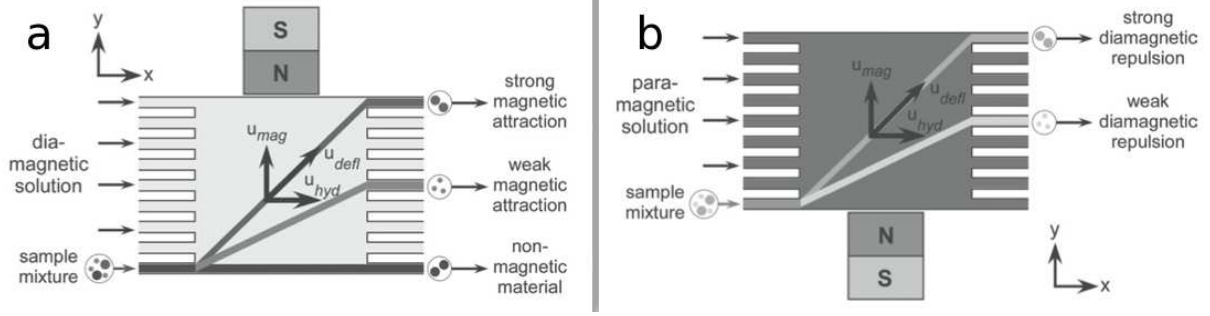
Figure 1.18: (a) A microfluidic system integrating a bulk permanent magnet for magnetic separation developed by the group Pamme. (c) A similar system used for magnetic repulsion. Figures adapted from [60]

The system has also been used to sort diamagnetic particles of different sizes by magnetic repulsion[62]. In this case, the magnet and the main inlet were positioned on the same side in order to exert a greater repulsion force on the particles, the bigger particles being repelled to greater distances (Fig. 1.18b).

A system based on soft magnets for particle sorting was developed by Afshar et al. (Prof. Martin Gijs' group) and presented in [63]. The system is composed of soft magnetic poles near a microfluidic channel, the magnetic element being polarized by a coil. Two distinct zones of magnetic actuation are present (see Fig. 1.19a). The first zone has the same function of attracting and concentrating the magnetic particles which flow near the magnetized elements. The second active zone is situated further in the channel and attracts the particles to the other side of the channel. The attraction force acting on the particles depend on their dimension, thus, particles of different size can be separated, as shown in the second frame of the figure.
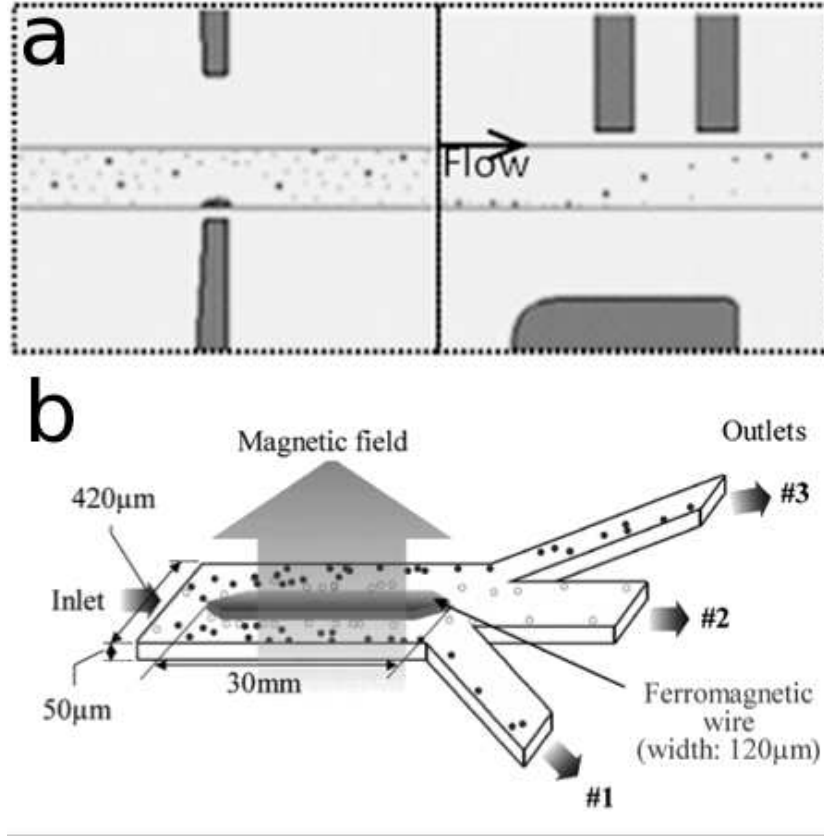
Figure 1.19: (a) Deviation of magnetic particles using soft magnets performed by the group of Gijs [63]. (b) Continuous sorting of red and white blood cells [64].

Han et al. used a ferromagnetic wire magnetized by an external field in order to separate red and white blood cells [65, 64]. Since red blood cells (RBC) are attracted to the highest magnetic field gradients, while white blood cells (WBC) are repelled from it, these cells can be sorted using a simple device, shown in Fig. 1.19b. In the figure, the solution containing both types of cells is pumped in the only inlet and exits the channel by three possible outlets. The ferromagnetic wire placed in the center of the channel concentrates the RBC, which are guided towards the central outlet, while the WBC are repelled from the wire and exit the channel by the two external outlets.

Still based on the continuous sorting of objects, many advances have been made using ferromagnetic stripes. The principle is shown by Inglis et al. in [66] and reproduced in Figure 1.20a. A magnetically tagged object submitted to a drag force inside a microfluidic channel is also submitted to a magnetic force when passing near soft magnetic stripes. The angle between the magnetic and the drag force deviates the object from its initial path, thus, separation can be achieved.
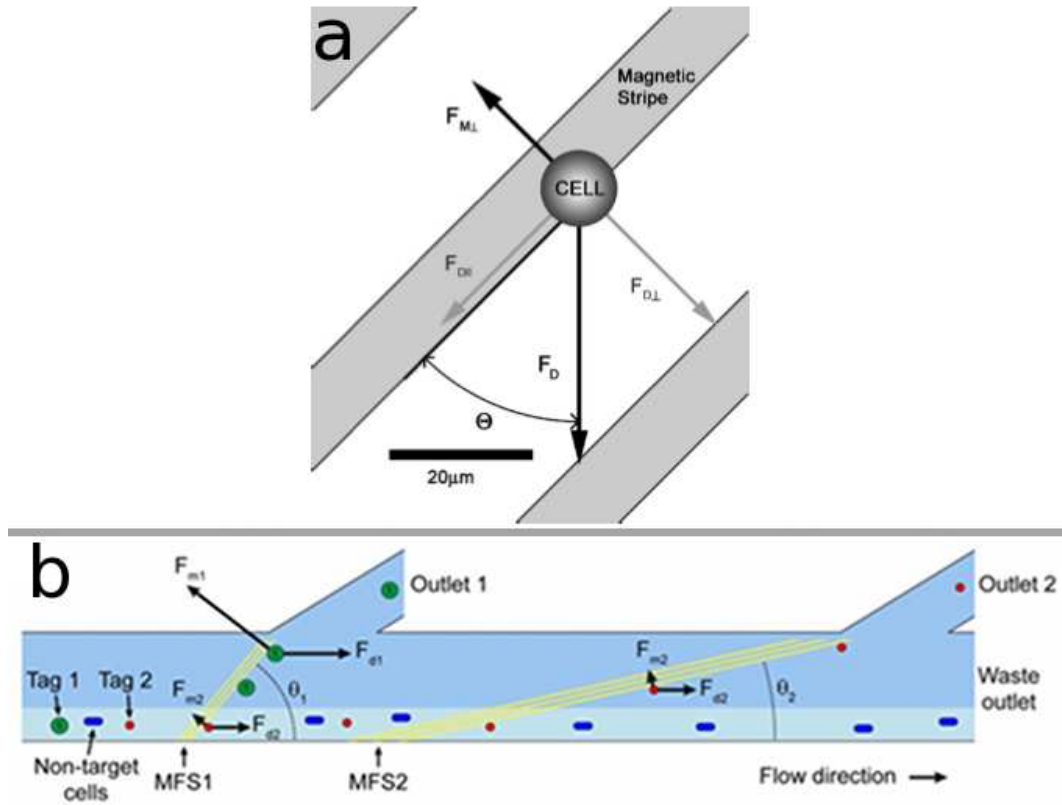
Figure 1.20: Soft magnetic rails deviating (a) cells [66] and (b) differently labelled objects [67].

This binary separation (magnetic/non-magnetic) has been reported in several publications [66, 68, 69, 70]. Adams et al. developed a system based on the same principle, but in which three types of objects can be sorted [67]. The system, shown in Figure 1.20b, has one inlet for the solution of objects to be sorted and one inlet for a buffer solution. The objects are concentrated in one side of the channel. A first set of magnetic stripes deviates a first group of magnetically labelled objects, while a second set deviates a second group. The third group is not labelled and follows the fluid flow without being deviated. The three groups are collected in different conveniently placed outlets. The separation of two different magnetically labelled objects results from a difference in both the drag force and the magnetic force, due to the use of different labels.

Another interesting system was developed by Fulcrand et al. (A.-M. Gué's group), which allows dynamic particle manipulation[71]. The working principle is reproduced in Figure 1.21a. Magnetic particles flow in liquid solution through a microfluidic channel. A set of micro-coils disposed successively from one side of the channel to the other is placed below the channel. The first coil is activated in order to capture the magnetic beads. The following coil is activated and the precedent is deactivated, displacing the group of particles further in the channel and towards a different position in the channel section. This is repeated until the particles are conveniently placed as regards to the channel outlets, then the particles are released from the coils and collected.
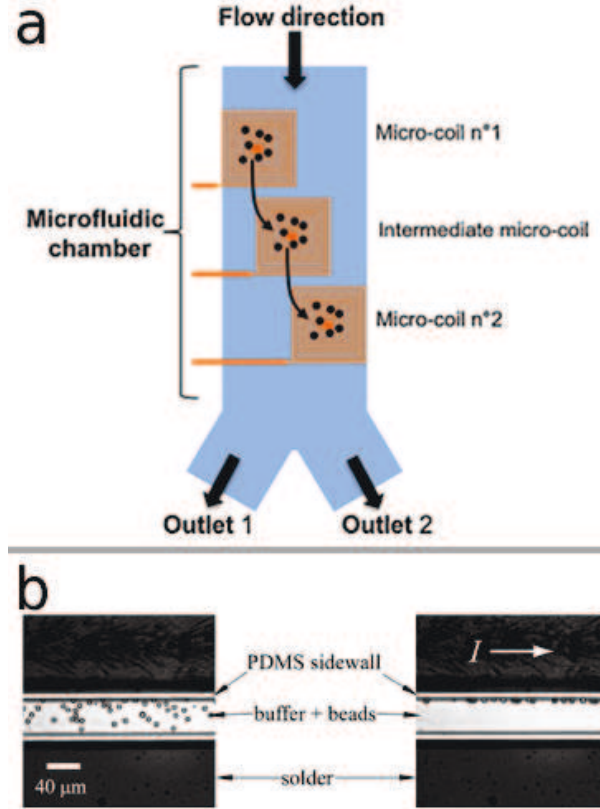
Figure 1.21: Particle deviation performed by the groups of Gué [71] and Shevkoplyas [72].

Other systems based on deviation of particles for separation were reported by Derec et al. [73] and Shevkoplyas et al. [72]. The deviation of the particles, in this case, is obtained by a permanent magnetic field created by a wire in the vicinities of the microfluidic channel. Figure 1.21b shows the system produced by the group of Shevkoplyas, where a microfluidic channel is seen in the center, with a conductive wires on each side. The magnetic particles inside the channel are randomly dispersed at first, since no magnetic field acts on them. Once a current passes through the top wire, the particles are attracted to it and are concentrated on one side of the channel. This method can be used to sort particles in a continuous fashion, since they are continuously guided, instead of captured/released.

Continuous flow separation using permanent micro-magnets is not reported, until today, outside Institut Néel/G2Elab. This is a major evidence of the importance of the technology developed in Grenoble for the microsystems field, particularly in biology and medicine. This idea has culminated in a project involving different laboratories and research domains, as discussed in the following section.

## 1.4   The ANR EMERGENT Project

The urbanization and industrialization of many regions around the globe have led to the contamination of the soil by several stable chemical compounds. Processes of

decontamination are being studied and are already used in many cases, but some polluants are difficult to remove. Bio-attenuation processes remain a big hope. In this case, the environment itself is responsible for the decomposition/transformation of the agressive agents by natural means, i.e., the action of local microorganisms[74].

The diversity of microorganisms in the soil, combined with their high capability to horizontally transfer[3] their genes, makes bio-attenuation a main option as regards to not yet handled polluents. Some of these microorganisms, especially bacteria, are able to develop new abilities to survive in a different environment and to feed from polluents due to genetic modification. Once this new adapted gene is created, the attenuation process is amplified by its horizontal transfer.

The practical importance of the study of these horizontal transfers is clear, however, some major difficulties related to the heterogeneity of the soil hold back the evolution of this research. It is a complex task to study a single population of bacteria if the actual sample contains several other species of microorganisms.

The EMERGENT Project focuses on this issue in order to both develop a method to isolate the population of interest from a complex medium and study the horizontal gene transfer between the individuals of this population. The degradation of lindane is taken as a model to study the role of the horizontal gene transfer on the adaptability of populations of bacteria in-situ. Lindane is chosen due to the complete absence of natural compounds similar to it on Earth, which explains the absence of microorganisms able to destroy the chemical compound on non-contaminated zones.

The approach chosen for the Project is, at first, to develop a technique to tag DNA with magnetic particles *in vitro* and, then, internalize it into the bacteria. The tagged bacteria can, thus, be manipulated (separated, positioned, displaced) with an applied magnetic field. Four laboratory partners from chemistry, physics and biology work together to achieve the goals of the EMERGENT Project. The role of each laboratory is given below:

- **Magnetic particles:** Fabrication of magnetic particles with controlled size and shape and on-demand addition of chemically or biologically functional groups. Laboratory: *IPCMS*, Strasbourg.
- **DNA, cells and bacteria:** Manipulation of DNA (inclusion or removal of specific sequences) and biological elements (cells and bacteria). Laboratory: *Ampère*, Lyon.
- **Micro-magnets:** Fabrication and integration of high-performance permanent micro-magnets. Laboratory: *Institut Néel*, Grenoble.
- **Magnetophoresis:** Conception and modeling of micro-systems dedicated to the capture and sorting of magnetically labeled objects. Laboratory: *G2Elab*, Grenoble.

The research presented here was developed at both G2Elab and Institut Néel and focuses on the corresponding areas in the list above. Chemical and biological details given here are restricted to those which are important for the development of this research. Further information can be found elsewhere [75, 76].

---

[3]Horizontal transfer is defined by the transfer between individuals of a same generation, as opposed to vertical transfer, which is the transfer "from parent to child".

# Chapter 2

# Development of micro-magnetic flux sources

The use of permanent magnets nowadays is widely spread and the applications range from fridge magnets and speakers to hard disks and wind turbines. The best magnetic properties are obtained with rare-earth-based magnets, which are usually massive (the characteristic dimension exceeds 1 mm) and fabricated by powder metallurgy (melting, casting, milling and sintering).

The top-down approach to obtain magnets in the sub-millimeter range (machining bulk magnets) is often not well-adapted and the magnetic properties and/or the integrability are lost in the process. In Grenoble, an effort is done in order to develop high-quality micro-magnets by the bottom-up approach. A partnership between CEA LETI and G2Elab resulted in the production of CoPt micro-magnets by electrodeposition. The integrability to micro-systems obtained with this technique was fairly good. However, the bi-stable switch shown in this article was able to perform a limited amount of commutations, due to the relatively poor properties of the integrated magnet.

Nowadays other techniques are being used in G2Elab and Institut Néel to develop micron-sized magnetic elements which can be integrated to micro-systems. In G2Elab, soft materials are one of the objects of study. These materials, as discussed before, have the advantage and, at the same time, the disadvantage of producing a significant magnetic field only when polarized by an external magnetic field. Along with the possibility to "turn on and off" the magnetic field, comes the need of a bulk magnetic field source.

At the Institut Néel, triode sputtering is used to produce fully dense magnetic films. This innovative technique required several studies on materials and on structural and magnetic properties which led to the development of high-performance magnets. Different approaches are being currently used for the micro-structuration of such magnetic films prior to their application to micro-systems and biology. This micro-structuration is based on three methods, presented below in their chronological order of development in the laboratory:

- Topographic Patterning (TOPO): The production of actual physical patterns on the film, leading to a structured surface, which can be planarized if needed. This method has two variations, as presented in Section 2.3;

- Thermo-Magnetic Patterning (TMP): The reorientation of magnetic moments in the film at certain zones by laser irradiation, resulting in flat micro-patterns above which a high magnetic field gradient is obtained;

- Micro-Magnetic Imprinting ($\mu$MI): Particles are positioned using a magnetic field

and subsequently embedded in a polymeric matrix, creating flexible, transparent and biocompatible (depending on the chosen polymer) magnetic components.

Size and shape of the micro-magnets, ease of the production method and adaptability to the potential applications have to be balanced for each of these methods. Their positive and negative points are further discussed in the next few sections.

This chapter is not an exhaustive description of all the methods used to develop micro-magnetic flux sources. Its goal is to present the most recent advances in the materials and micro-structuration development in the group, together with the characterization techniques which are relevant to this research. The methods used to estimate the dimensions of the micromagnets produced by Thermo-Magnetic Patterning – which will be shown further on as a key parameter for their application – are presented.

## 2.1  Triode sputtering

Triode sputtering is a physical vapor deposition (PVD) technique which allows rapid deposition of thick films, due to its high deposition rate, which can be up to 20 $\mu$m/h. The setup used in this work is schematically shown in Figure 2.1. The substrate is positioned facing the target inside a vacuum chamber. Four targets can be positioned simultaneously on the rotating target holder. The dimension of each target can be up to $10 \times 10$ cm$^2$. A substrate diameter up to 8 inches is acceptable, but 4-inch silicon wafers are most commonly used. The base pressure of the system is $10^{-7}$ mbar, while the working pressure is around $10^{-3}$ mbar, controlled by a flow of argon gas. A tungsten filament positioned close to both the target and the substrate is heated up and emits electrons, which are attracted to the anode. The collision between electrons and inert argon atoms generates a plasma. Two bulk permanent magnets are used both to elongate the trajectory of the electrons towards the anode and to confine the argon plasma. A difference in potential applied between the target and the substrate is responsible for accelerating the plasma ions towards the target. The alloy on the target is sputtered by the ions in all directions, part of it being deposited on the substrate. The substrate holder can be rotated during deposition in order to increase homogeneity in composition and thickness and heated up in order to induce changes in the microstructure of the deposited films. Also, the target-substrate distance can be adjusted for better sputtering conditions [77, 78, 79].
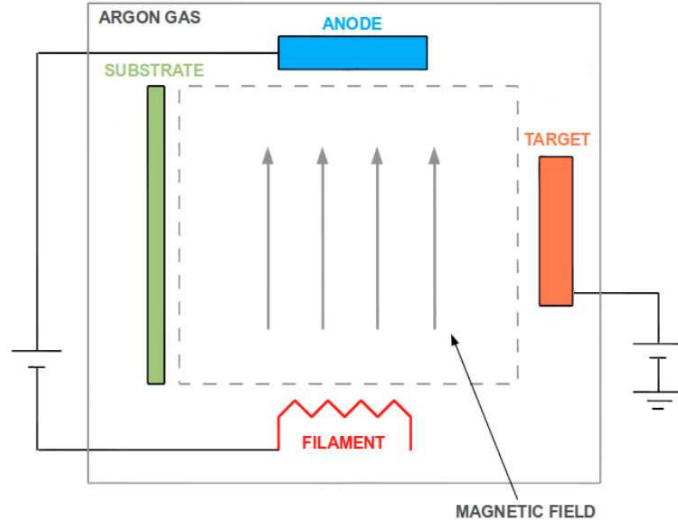
Figure 2.1: Schematic of the triode sputtering apparatus.

### 2.1.1 Materials

The three main materials used in the group at the moment are based on the $Nd_2Fe_{14}B$, $SmCo_5$ phases and FePt. This work has been mostly focused on NdFeB, thus the following discussion on magnet preparation will be limited to this material. However, it is worth mentioning that very good magnetic properties can be obtained with all these materials. Their properties highly depend on the parameters chosen for their deposition. Figure 2.2a and b show hysteresis loops obtained with 5 $\mu$m-thick films of SmCo and FePt, respectively. At certain conditions a very high magnetic texture can be obtained with SmCo. In-plane (ip) and out-of-plane (oop) hysteresis loops show a clear in-plane texture for this film. The pole figure obtained around the {200} axis confirms that texture. Coercivity values up to $\mu_0 H_C = 1.3$ T and remanence up to $\mu_0 M_R = 0.8$ T can be obtained. In the case of FePt, isotropic films can be obtained with coercivity up to $\mu_0 H_C = 1.0$ T and remanence up to $\mu_0 M_R = 0.7$ T. These films are especially interesting for application in corrosive environments.
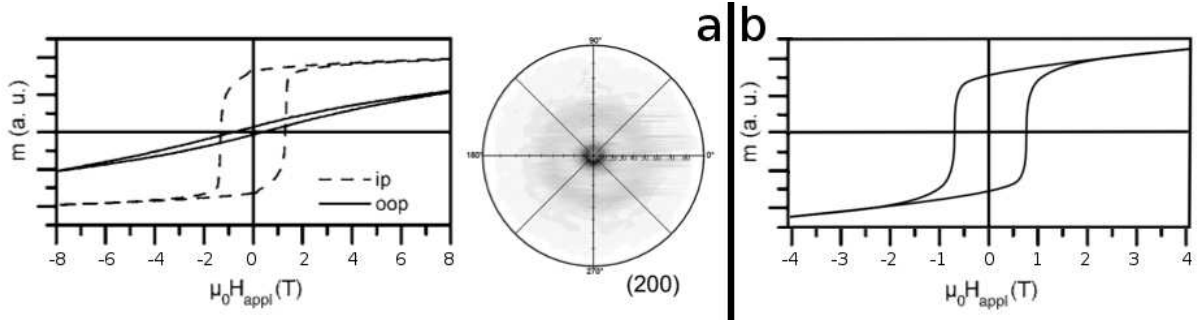
Figure 2.2: (a) In-plane and out-of-plane hysteresis loops confirming a high in-plane texture on a SmCo film. The pole figure around the {200} confirm the crystalline structure in that plane. (b) Hysteresis loops obtained with an FePt film. Both films show high coercivity values.

A major concern for the deposition of thick films is their mechanical stability. Many factors can lead to cracks or peel-off of the film: a difference in thermal expansion between layers, crystallization processes, phase transformations, etc. For NdFeB, peel-off and fractures are minimized by the use of, respectively, a tantalum buffer layer and a thermally oxidized silicon wafer. The annealing temperature can also be reduced in order to prevent peel-off, though it has an influence on the final magnetic properties. A capping tantalum layer is used to prevent oxidation of the NdFeB layer.

The magnetic materials used here can be amorphous or crystalline. This characteristic is determined by two key parameters: deposition temperature and annealing temperature. These parameters are also strongly responsible for the size and shape of the grains, in the crystalline case. One-step (deposition) and two-step (deposition + annealing) processes can be used to tailor the magnetic properties. In the case of NdFeB, highly anisotropic, high-quality films can be obtained with the two processes, although the deposition followed by annealing is more currently used, since it results in better magnetic properties.

A one-step process generates an as-deposited crystalline structure. The deposition temperature plays an important role on the coercivity of the magnets. Values of coercivity up to $\mu_0 H_C = 0.3$, 0.8 and 1.2 T are obtained with depositions at $500\,°C$, $575\,°C$ and $600\,°C$, respectively. A remanence of 1.2 T is obtained in the latter case, which is lower than usually obtained with a two-step process (around 1.4 T). High-quality magnets are usually obtained when the grains are equiaxed or columnar. In order to obtain equiaxed grains, the deposition temperature is set to $\leq 450\,°C$, which leads to an amorphous and magnetically soft phase. Then, the film is annealed at $750\,°C$ giving rise to the anisotropic, magnetically hard phase. The resulting microstructure is shown in Figure 2.3a. Columnar grains can be obtained with a deposition at $500\,°C$ followed by annealing at $750\,°C$. The grains can be as long as the film's thickness, as shown in Fig. 2.3b.
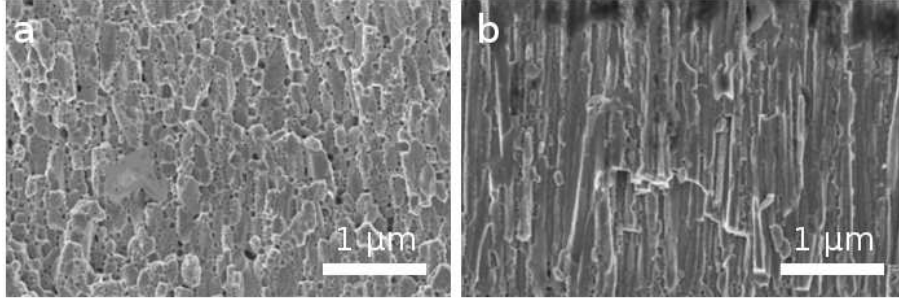
Figure 2.3: SEM fracture views of NdFeB films showing (a) equiaxed grains and (b) columnar grains.

The Nd-content in the film is observed to be closely related to the coercivity. Up to a certain point, the coercivity is increased as the Nd-content increases. SEM observations and EDX analysis have shown that an exceeding amount of neodymium can precipitate at the grains boundaries. This intergranular phase leads to magnetic decoupling of the grains which, in turn, leads to a higher coercivity. The choice of a Nd-rich target for triode sputtering is convenient to take into account grain decoupling, but also to compensate the difference in sputtering rate of the different elements.

Another interesting characteristic caused by this excess in Nd is that, during annealing, part of it is extruded out of the film. The result, analyzed by SEM, is shown in Figure 2.4a. As the Nd phase is squeezed out, it deforms the Ta layer creating bumps on the surface of the film. An analysis by atomic force microscopy (AFM) reveals that these bumps have an average height of about 1 $\mu$m (Fig. 2.4b). At naked-eye observation, a less shiny aspect of the films (caused by the bumps) - as opposed to the mirror-like aspect of a flat film - is an indicator of high coercivity.
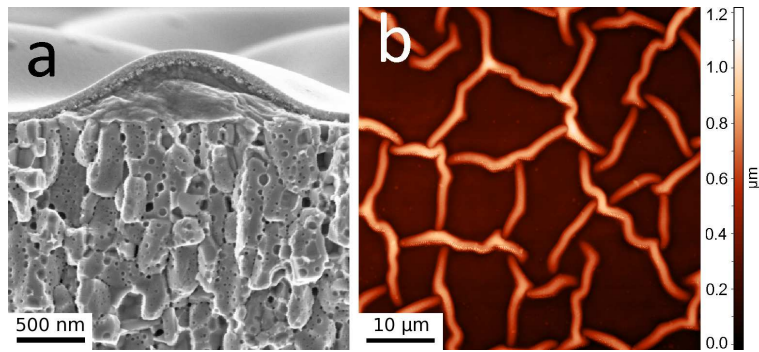


Figure 2.4: (a) SEM image of a fracture cross-section. (b) AFM image of the film's surface with bumps.

Once these parameters are well known and controlled, very good magnetic properties can be obtained. The films used for the applications shown in this report are developed

with the parameters set for maximal coercivity and remanence. These characteristics, as discussed, are associated with highly anisotropic films and the $Nd_2Fe_{14}B$ phase. In order to confirm that this phase is obtained, x-ray diffraction (XRD) measurements are performed on a sample of the magnetic film. The intensity peaks clearly correspond to the {hkl} peaks of the 2-14-1 phase (Fig. 2.5a).
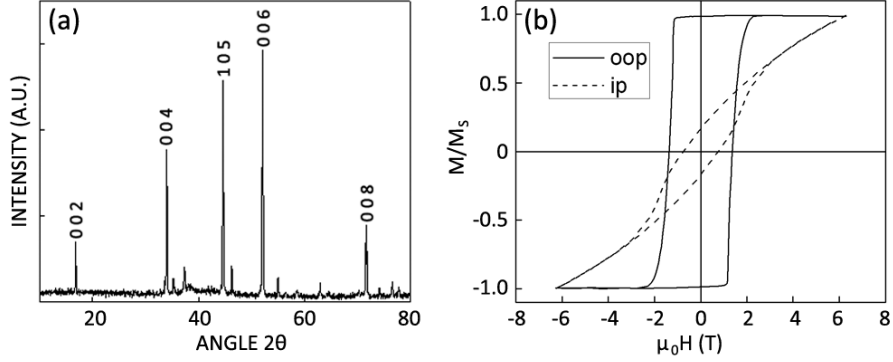


Figure 2.5: Microstructural and magnetic analysis of the films: (a) $\theta - 2\theta$ XRD pattern with Co radiation – the {hkl} indices of the $Nd_2Fe_{14}B$ phase are shown; (b) in-plane (ip) and out-of-plane (oop) hysteresis loops.

In-plane and out-of-plane hysteresis loops also confirm a high crystallographic texture (Fig. 2.5b). The easy axis of magnetization is perpendicular to the film plane. High coercivity values (around 1.8 T) are obtained along this direction. The rectangular shape of the out-of-plane loop is another indicator of the high magnetic properties of these films. This shape is associated with a homogeneous coercivity of all the grains, as opposed to the behavior associated with a rounded loop, where some grains are much less coercive than the others.

## 2.2 Characterization of micromagnets

Before presenting the micro-struturation methods in further details, the less usual techniques used to characterize the micro-magnets will be briefly shown in the next sections.

### 2.2.1 Magneto-optic imaging

In this work magneto-optic imaging films (MOIFs) supplied by Prof. Rostislav Grechishkin (Tver State University, Russia) have been used. Magneto-optic imaging takes advantage of the interaction between polarized light and a magnetic material in order to characterize domain structures. The MOIFs are composed by a ferrite garnet film below

which an aluminium layer is deposited. As the polarized light passes through the garnet, its plane of polarization is rotated proportionally to the magnetic component which is parallel to its direction of incidence. This *Faraday rotation* occurs twice, since the light is reflected by the aluminium layer and passes through the garnet a second time before visualization (Figure 2.6). The double rotation improves the contrast obtained with the MOIFs.
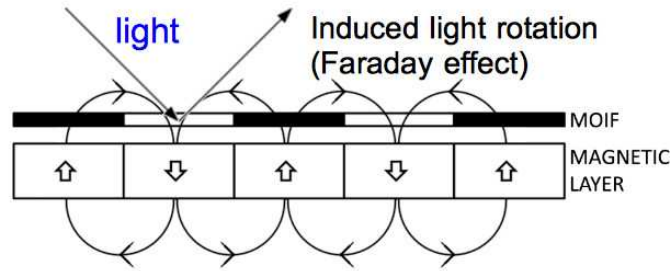


Figure 2.6: Schematic representation of the image obtained with a MOIF, observed by the rotation of polarized light.

Both qualitative and quantitative information about the stray magnetic field can be obtained with these soft magnetic films. A qualitative image is produced by uniaxial MOIFs (U-MOIFs). These films have an out-of-plane spontaneous magnetization, which means that polarized light is rotated even if no field is acting on the MOIF, leading to a binary image. Figure 2.7a shows a U-MOIF image obtained when the garnet is placed above an out-of-plane magnetic pattern. Note that in this film only the "Institut NEEL" inscription has its magnetization pointing "up", while everywhere else the magnetization points "down". As the field created by this magnet is restricted to the zones close to the pattern[1], a limited zone of the MOIF around the inscription reveals the out-of-plane field, leaving all the surrounding areas in the non-saturated state.
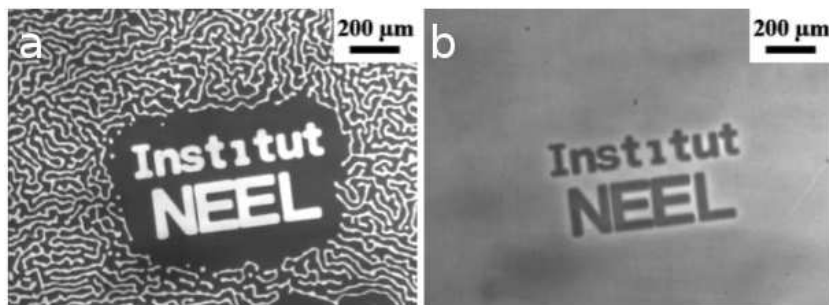


Figure 2.7: (a) Uniaxial and (b) planar MOIFs showing a magnetic pattern. The first one shows a binary contrast, while the second reveals the field in grayscale.

---

[1]The magnetic field generated by micro-magnetic patterns and the edge effect mentioned here are discussed in further detail in Chapter 4.

In a P-MOIF (P, for planar), the spontaneous magnetization is in the film plane. If a P-MOIF which is not under the influence of a magnetic field is observed, a gray image is obtained. However, if this magnetization is forced by an external field in the oop direction, a black or white contrast is produced. Figure 2.7b shows the same "Institut NEEL" inscription observed with a P-MOIF. In this case, a grayscale image can be obtained, with the color intensities corresponding to the magnitude of the field, thus allowing quantitative imaging.

## 2.2.2 Magnetic Force Microscopy (MFM)

The setup of a magnetic force microscope is very similar to that of an atomic force microscope (AFM). Usually in both techniques the force applied on a sensitive object (tip) is measured by the deflection of a cantilever on which the tip is mounted, or by the variation in the resonance frequency of the tip. This deflection is often observed by the reflection of a laser beam on the cantilever. In MFM the tip is coated with a magnetic material, which may have a wide range of properties, depending on the measured sample. Tips coated with a high-coercivity material are used to produced the images shown in this work, so that the up and down magnetic field can be observed. The high stray field generated by the magnetic films used here can reorient the magnetization of a low coercivity tip, thus resulting in an image which shows the intensity, but not the direction, of the field.

One of the main advantages of MFM is its high resolution, in the order of tens of nm. This advantage can be clearly observed in Figures 2.8a and b, which show MOIF and MFM images of the same magnetic pattern. A MOIF averages the magnetic field, showing rounded features, while the MFM measurement performed much closer to the sample and much more accurately shows squared patterns with rounded edges. Furthermore, the measurements are performed without contact with the sample, so the subject of interest can be preserved and observations are possible even in the presence of a coating layer.
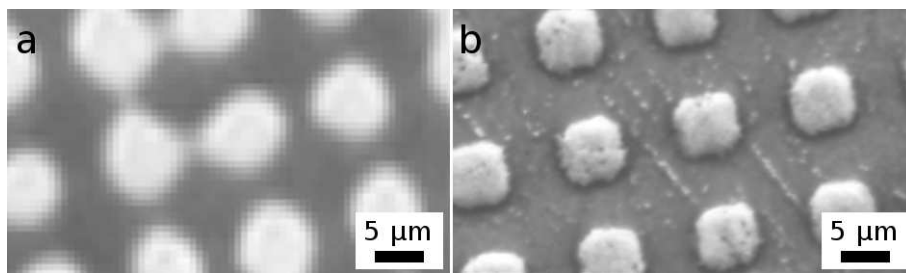


Figure 2.8: A magnetic pattern observed by (a) MOIF and (b) MFM showing the very different resolutions obtained with these techniques.

## 2.3 Topographic patterning (TOPO)

The principle of obtaining micro-magnets by the topographic method is to deposit the magnetic film onto an already patterned substrate. The step-by-step of the topographic patterning technique is shown in Figure 2.9a and developed as follows:

- An aluminum layer with thickness around 100 nm is deposited onto a silicon wafer;

- A photoresist is spin-coated on top of the Al layer and patterned by soft lithography;

- The aluminum layer is wet etched on the exposed zones. The Al layer zones covered by the photoresist remain and will serve as a "hard mask" while etching the silicon substrate;

- Deep Reactive Ion Etching (DRIE, see below) is used to etch the silicon substrate, creating the desired topography;

- The remaining resist and the Al layer are removed and the substrate is thermally oxidized in order to produce a superficial SiO$_2$ layer, which will serve as an adhesion layer;

- Triode sputtering is used to deposit the magnetic layer with buffer and/or capping layers, if needed.

DRIE is a highly anisotropic etching technique commonly used in microelectronics. Successive steps where an ion plasma is projected towards the substrate, attacking its surface, and a passivation layer is chemically deposited are used in order to create holes in the substrate with almost perfectly vertical walls. This method is known as the Bosch process.
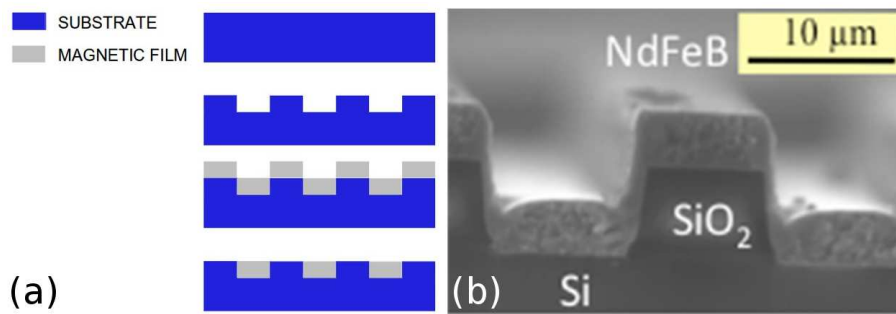


Figure 2.9: (a) Simplified steps to produce topographically patterned micro-magnets: substrate patterning; deposition of a magnetic layer; planarization by removal of the upper magnets. The last step is optional, depending on the application. (b) An example of topographic magnets.[80]

The result of the steps above is a magnetic layer deposited on two levels: the normal surface of the silicon wafer (upper level) and the etched regions produced by DRIE (lower level), as shown in Fig. 2.9b. The size and shape of the topographic micro-magnets are closely related to the characteristics of the patterned substrate. The thickness of the deposit has to be adapted to the size of the produced patterns, as the growth of the magnetic film is affected by the edges of the patterns.

The etching process itself has some constraints about sizes and aspect ratios. First of all, the minimum feature size is limited by the lithography process. Using the standard procedure – exposing a photoresist with a few $\mu$m in thickness to UV light – patterns as small as one or two microns can be obtained with reasonable repeatability. Below this value, light scattering starts to be a major problem and other slower and more expensive processes have to be used. Once the pattern dimensions are chosen, one has to choose the proper depth of etching. The production of patterns with very high aspect ratio by DRIE is possible, however, the mechanical stability is compromised and the features might break during the further steps of fabrication or integration to the microsystems.

An alternative technique to produce topographic magnets consists of depositing a magnetic film on a flat substrate and subsequently etching the film at certain zones. The etching step, in this case, is performed in a solution (wet etching) of $(NH_4)_2S_2O_8 \cdot H_2O$ and $H_2SO_4$. A schematic of the process and an actual wet etched topographic magnet are shown in Fig. 2.10a and 2.10b, respectively. Due to the high susceptibility of rare-earth elements and iron to oxidation, and to the use of chemicals, extra care has to be taken when using this process. The high magnetic properties associated to NdFeB magnets can be obtained if the magnets are correctly processed, as reported in [80].
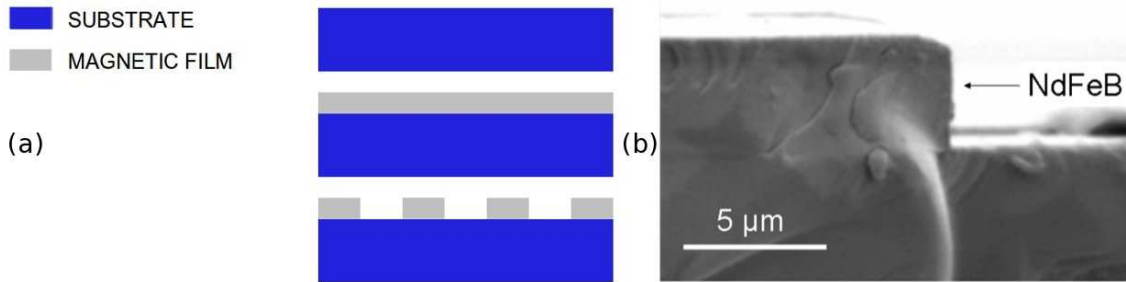


Figure 2.10: (a) Schematic representation of topographic patterning by the wet etching method: deposition of the magnetic layer; wet etching. (b) SEM image (side-view) of a patterned magnet.[80]

In this work, topographic magnets produced exclusively by the DRIE method were used. Simple geometric shapes (lines, squares and circles), isolated or arrayed, were fabricated in two sets:

- Small patterns – 5 to 25 $\mu$m as the smallest lateral dimension – with an etching depth of 20 $\mu$m;
- Large patterns – 50 to 200 $\mu$m as the smallest lateral dimension – with an etching depth of 100 $\mu$m.

## 2.4 Thermomagnetic patterning (TMP)

Thermomagnetic patterning is a recently developed technique used in magnetic films to produce - as it can be deduced from its name - patterns by simultaneous thermal and magnetic action. The process is based on magnetic writing, where a magnetic layer is locally exposed to a magnetic field which overcomes its coercivity and reorients ("writes") its moments. In the standard magnetic writing the moments can be reoriented in two possible directions, which will then correspond to a 0 or a 1, in a binary system. In the case of TMP, the whole magnet, i.e. a piece of film with a surface typically around 4 cm$^2$, is exposed to the magnetic field. In order to produce micropatterns, the usual process occurs as follows:

- The annealed magnetic film has its moments saturated in one direction, e.g. out-of-plane, up (Fig. 2.11a);

- The sample is positioned above a bulk magnet which produces a field opposing its initial magnetization (down). The field created by the bulk magnet does not exceed the film's room temperature coercivity;

- A mask with the desired patterns is position above the sample and a laser beam irradiates the whole (Fig. 2.11b);

- The laser beam which passes through the mask is partly absorbed by the surface of the sample, which heats up;

- Heat diffuses through the magnetic layer, lowering its coercivity in the vicinities of the irradiated zone (Fig. 2.11c);

- The volume in which the coercivity is overcome by the external field has its moments reoriented (Fig. 2.11d).
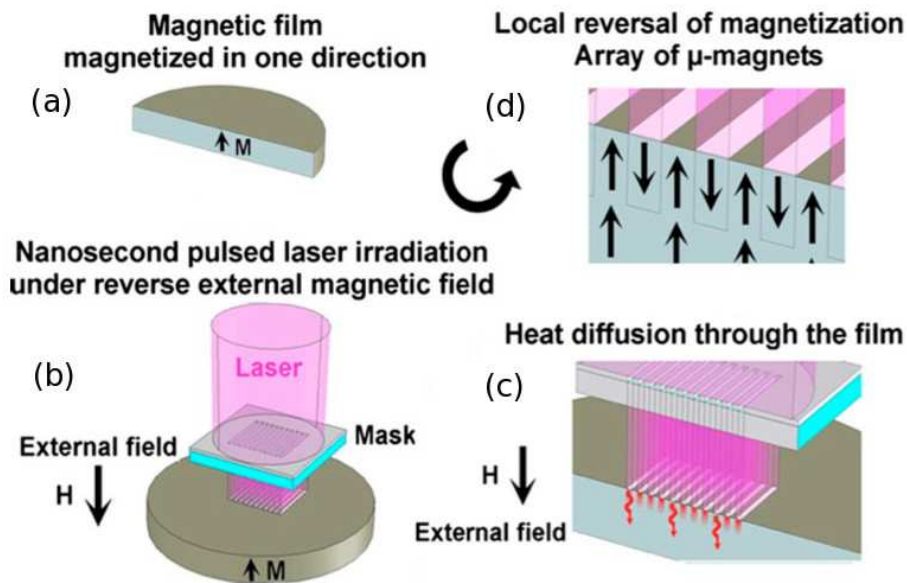


Figure 2.11: Schematic of Thermo Magnetic Patterning principle. [81]

These steps have been followed for most of the samples produced by TMP. However, some adaptations can be used to vary the shape of the patterns or to produced different magnetic arrangements. First of all, the magnetization of the film does not have to be necessarily out-of-plane. If an isotropic magnetic film is used, the magnetization of the layer can be reoriented in any direction, according to the applied field. This can be used to create complex magnetic structures such as "magic cylinders" and Hallbach arrays (see the Magnetic Patterns section).

The parameters of TMP can be combined in order to increase the magnetically reoriented volume. Three main parameters can be changed:

- **The laser fluence** - the energy per surface unit - is the easiest parameter to change, as it requires no additional apparatus. An increase in the fluence will increase the energy absorbed by the sample and, thus, the volume which is sufficiently heated to be magnetically reoriented.

- **The external field** is applied with a bulk magnet or an electromagnet. With the first, a continuous and autonomous field is applied but its intensity is invariable. The electromagnet allows the precise control of the field to which the sample is exposed. However, cumbersome side-equipment is needed: the mandatory power supply and a delay generator - in the case the magnetic field generated by the electromagnet is pulsed - in order to synchronize both the magnetic field and the laser pulses.

- **The temperature of the sample** can be modified by placing it above a heating plate which will be set to a precise temperature. Increasing the initial sample temperature improves the gain in temperature with the same laser fluence, thus improving magnetization reversal. This heating plate also requires a power supply.

A brief experimental and theoretical analysis of the influence of these variables on the final lateral shape of the magnetic pattern is presented in Annex A[2].

Other parameters concerning the laser beam can also be chosen in order to optimize TMP. The duration of the pulse, the homogeneity of the laser beam in space and its wavelength have an influence on the patterning process. However, these parameters depend on the laser source and are usually not modified. In this work a KrF excimer laser was used, with 248 nm wavelength and 20 ns pulse duration. This type of laser was chosen for its high homogeneity in space and high maximum fluence, allied with a good compatibility with the materials used here.

### 2.4.1 Mask fabrication

The first requirement for a mask to be used in TMP is that at least two distinct intensities of the laser beam can be obtained after it passes through the mask. It implies that

---

on a mask there will be a zone A of high transmittance and a zone B of low transmittance. Two types of mask were used in this work. The first one was produced in the laboratory using standard microfabrication techniques and will be described below in more details, while the second was purchased from different suppliers, according to the required patterns.

Both types of mask are based on zones of maximum and minimum transmittance, ideally 100% and 0%, respectively. The major difference between them is that the home-made masks (Fig. 2.12a) are produced on quartz substrates - transmittance >85% for a wavelength of 248 nm - while the purchased masks (Fig. 2.12b) consist of holes produced on a thin sheet of an opaque material, usually copper or $Si_3N_4$.
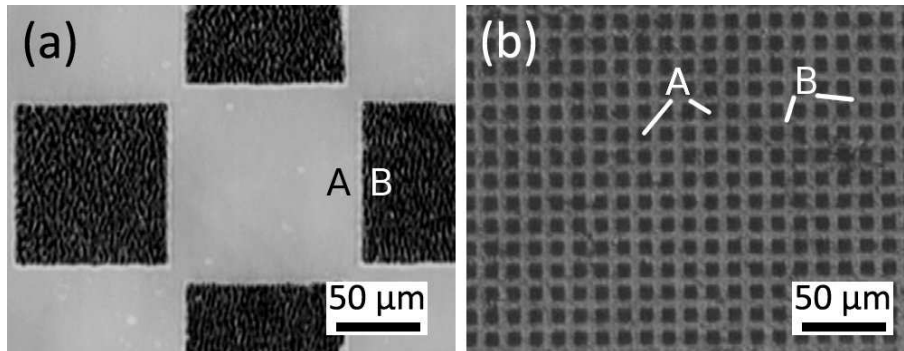


Figure 2.12: Masks for Thermo Magnetic Patterning: (a) a home-made mask with chessboard patterns produced on a quartz substrate; (b) a purchased mask. A and B represent zones of high and low transmittance, respectively.

The home-made masks are fabricated on 500 nm-thick quartz plates. Either tantalum or chromium is deposited by sputtering on the substrate to serve as an adhesion layer. Chromium is preferred for its higher reflectivity to a 248 nm wavelength. This first 5 nm-thick layer is followed by a 100 nm-thick layer of copper, also sputtered. A negative photoresist (ma-N 420) is used to create a model of the patterns which will be used for TMP. The resist is spin-coated on the Cu layer to a thickness of 2 $\mu$m and lithographed, resulting on the inverse of the desired TMP patterns. Copper is, then, electrodeposited on the sputtered copper layer up to a thickness of 2 $\mu$m (it should not be thicker than the resist layer). The resist is removed with acetone, exposing the copper surface, which is then wet etched using Etch 18.

As regards the TMP process, each type of mask presents its advantages and drawbacks, mostly related to the fabrication methods. First of all, cost and time do not go together. Quartz-based masks cost less, since they are home-made with standard materials and techniques, but take much more time and much more steps to fabricate. Purchased masks can be chosen between standard products, such as grids for Transmission Electron Microscopy (TEM), and custom made masks, in which the patterns can be home-designed. In any of the two cases, the prices often overcome the hundreds of euros.

The size range of the patterns which can be obtained with each type of mask are

comparable, but there are some important factors to consider. First of all, the home-made masks can be quick and easily produced if the pattern dimensions are down to tens of $\mu$m. Below this dimension, more precise lithography techniques, such as ion beam lithography, may be required. The pattern dimensions of purchased masks are usually in the $\mu$m range, depending on the supplier and the fabrication method. A very important thing to notice is that single-layer masks have a considerable thickness, from tens to hundreds of micrometers. Thus, a small tilt in the mask during TMP can significantly disturb the irradiation zones.

Last, but not least, interference can be an issue when producing magnetic patterns. In any mask, the edges of the patterns can diffract the laser beam, creating fringes of higher and lower intensity. In the case of the quartz masks, the laser beam can also be reflected multiple times inside the substrate, thus, creating fringe patterns of irradiation. This effect is caused if the upper and lower faces of the quartz plate are not parallel. An example of interference cause by reflection inside the quartz substrate is shown in Figure 2.13. This figures shows a U-MOIF image of a NdFeB disk in which TMP was performed. A chessboard mask was used to produce the pattern in the center-left of the figure. Each square is an individual micro-magnet with lateral dimensions of $50 \times 50\ \mu m^2$. The fringes indicated by the arrow are caused by interference.
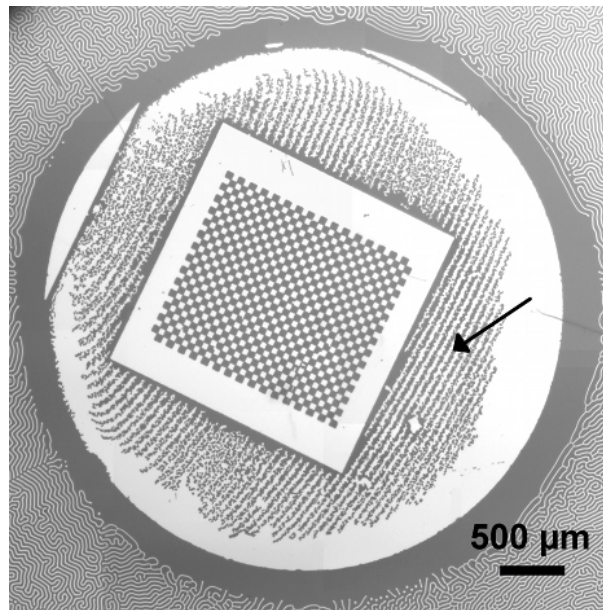


Figure 2.13: Interference patterns caused by reflections in the quartz substrate.

## 2.4.2 Depth of magnetization reversal

Three approaches have been recently developed in the group and are used to estimate the depth of magnetization reversal, d, in the samples produced by TMP:

- Scanning Hall Probe Microscopy (SHPM) + analytical calculations of the magnetic field;

- Magneto-optic imaging + VSM measurements;

- Analytical simulations of heat diffusion + coercivity × temperature measurements.

These three methods have been used on the characterization of several samples and have presented fairly similar results. The description of each method presented next considers samples prepared with the same parameters for TMP: magnetic films with thickness t = 5 $\mu$m, room temperature coercivity around 1.9 T and remanent magnetization around 1.3 T, external field generated by a bulk permanent magnet ($\mu_0 H = 0.5$ T at its surface) and a single laser irradiation with fluence 240 mJ/cm$^2$.

*SHPM and analytical calculations*

A Scanning Hall Probe Microscope has been developed by the group of Klaus Hasselbach (Institut Néel). This microscope measures the z-component of a sample's stray magnetic field using a second-generation quantum-well Hall probe based on a 2D electron gas. Its resolution - in the order of 20 $\mu$m - is related both to the size of the probe (4×4 $\mu$m$^2$) and to the probe-sample distance, which is typically around 26 $\mu$m. Further details about the technique can be found in Mikhail Kustov's PhD thesis and in [82].

The following measurements and calculations have been performed by Kustov and present in [81]. Figure 2.14a shows the z-component of the stray field ($B_z$) created by a chessboard pattern, as observed by SHPM 26 $\mu$m above the surface of the film. The inset shows the $B_z$ profile along the line AB drawn in the main figure.

In order to estimate the depth of magnetization reversal, analytical calculations of $B_z$ are performed considering an array of micro-magnets with the same lateral profile (Fig. 2.14b) and varying $d$. Three examples of the $B_z$ profile are shown in the inset of Fig. 2.14b for different values of $d$: 0.5 $\mu$m (blue), 1.0 $\mu$m (red) and 1.5 $\mu$m (green). Based on this method a reversal depth of 1.1 ± 0.2 $\mu$m, the error is associated with uncertainties on the estimated volume and the sample-probe distance.
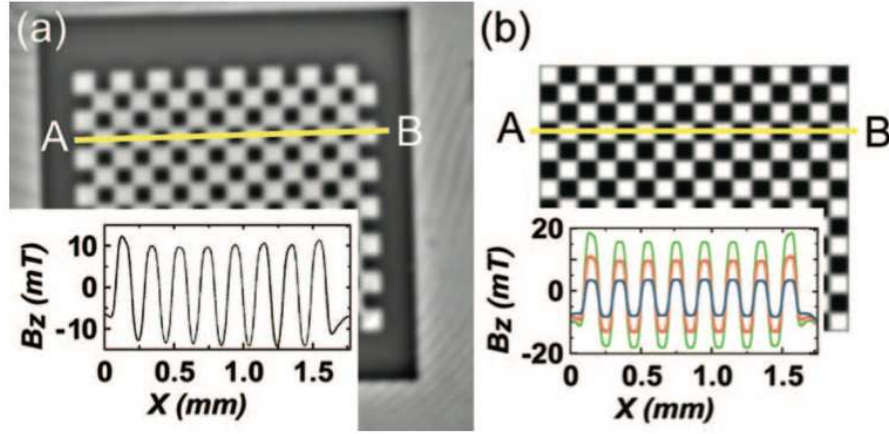
Figure 2.14: (a) Representation of the z-component of the magnetic field as observed by SHPM; inset: $B_z$ profile along the yellow line; (b) Schematic of the magnets considered on the analytical calculations; inset: $B_z$ profiles corresponding to magnets with different reversal depths (0.5 $\mu$m - blue; 1.0 $\mu$m – red; 1.5 $\mu$m – green).

*MOIF observations and VSM measurements*

In this approach the magnetic patterns are at first observed with a U-MOIF so as to calculate the areas corresponding to the irradiated zone ($S_1$) and the whole surface of the film ($S_2$) zones. The image is rendered binary and the pixels of each zone are counted using the ImageJ software. The reversed volume is then considered to be a parallelepiped, as shown in Figure 2.15a, with d as an unknown variable.

VSM measurements are performed in the sample in order to obtain the values of magnetization at both the patterned state $M_{ri}$ and the remanent state after saturation $M_{rs}$. Figure 2.15b presents an example of the hysteresis cycle obtained with a TMP sample. The following equation is used to determine the value of $d$:

$$d = \frac{1}{2} t \frac{S_2}{S_1} \left( 1 \pm \frac{M_{ri}}{M_{rs}} \right) \tag{2.1}$$

The thickness of the film is represented by $t$. The reversal depth obtained with this macroscopic approach is 1.2 $\pm$ 0.3 $\mu$m, the error in this case coming from the uncertainty in the estimation of the film thickness and the areas corresponding to the irradiated and non-irradiated zones.
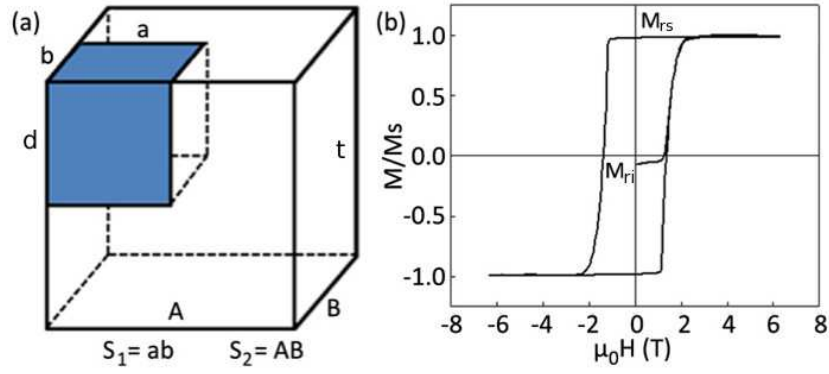
Figure 2.15: (a) Representation of the ideal shape of the magnetic patterns considered in the calculation of reversal depth. In blue, the zone which has been magnetically reversed. (b) Hysteresis loop of a sample patterned by TMP, showing its initial magnetization $M_{ri}$ and the remanent magnetization after saturation $M_{rs}$.

*Simulations of heat diffusion and $H_C \times T$ measurements*

The last method used for the estimation of reversal depth is based on a 1D heat diffusion analytical model of the system. In this model the energy coming from the laser beam is absorbed by the material. As a consequence, it heats up the first layer of the film and the heat diffuses towards the magnetic layer. The film is discretized in several points and the temperature of each point is determined from the time $t_0$, in which the laser beam starts to heat the sample, to the time $t_f$, in which the sample has cooled down to room temperature. Further details of the model are given in Annex B. Based on these simulations the maximum temperature $T_{max}(d)$ to which a point located at depth $d$ is heated up can be determined.

The coercivity $\times$ temperature curve is obtained by measuring the hysteresis loops of the magnetic film at different temperatures. Figure 2.16a shows a typical $H_C \times T$ curve obtained for a NdFeB film using a VSM. Combining these values with the maximum temperature values obtained with the model one can obtain the black curve shown in Fig. 2.16b, representing the minimum coercivity $\mu_0 H_{tot}[T_{max}(d)]$ reached in each point of the film.
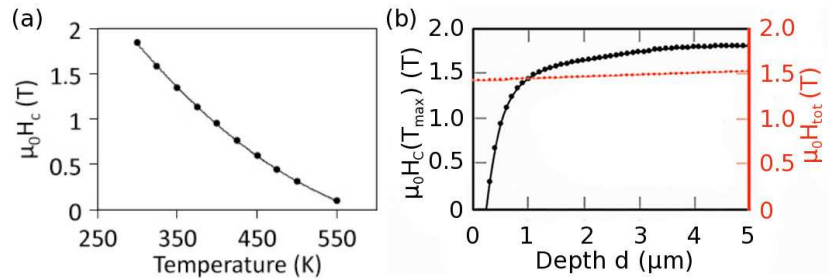


Figure 2.16: (a) Coercivity $\times$ temperature curve for a NdFeB film with room temperature coercivity of 1.9 T. (b) Minimum coercivity reach in each point along the depth of the film (black) and total field (red). The curves cross at $d_0 = 1.1 \ \mu$m.

Figure 2.17a shows a schematic of a film with its crystalline structure. In the model developed here, this film is actually considered to be homogeneous, with the fields from each part acting as schematized in Figure 2.17b and described below.

The condition for magnetization reversal is that the total field $\mu_0 H_{tot}[T_{max}(d)]$ acting on a certain depth in the film (the yellow point in Fig. 2.17b) overcomes $\mu_0 Hc[T_{max}(d)]$. The total field is calculated by the sum of the external field from the bulk magnet $\mu_0 H_{ext} = 0.5$ T and the demagnetizing field $\mu_0 H_{demag}(d)$ from the magnetic film itself, which varies according to the depth. The demagnetizing field is, at first, $\mu_0 H_{demag}(0) = 0.9$ T and $\mu_0 H_{tot}(0) = 1.4$ T. Once the magnetization of the film starts to reverse, the film contains two regions: the lower saturated region with thickness $t - d$, which generates a demagnetizing field of 0.9 T, and the upper reversed region with thickness d, with the demagnetizing field calculated numerically. The total field along the thickness of the film is plotted in red in Fig. 2.16b. The depth at which the total field overcomes the coercive field is observed to be $d_0 = 1.1$ $\mu$m.
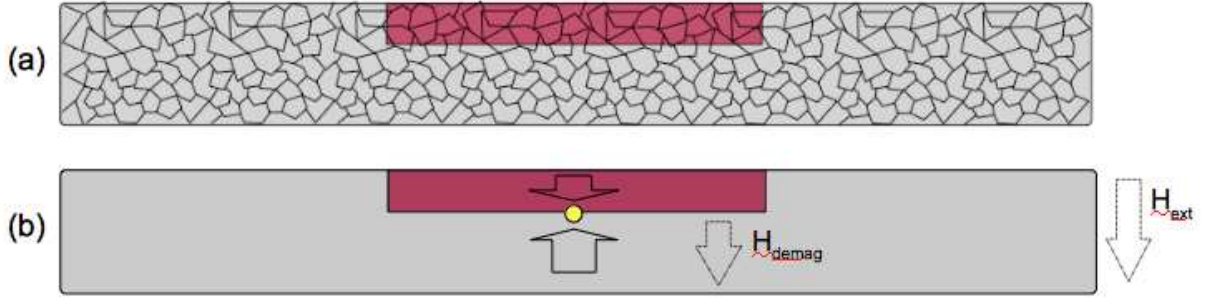


Figure 2.17: (a) Schematic of the grain structure of a magnetic film showing the zone heated by the laser. (b) Schematic of the homogeneous film and the magnetic fields from different sources acting on it.

Considering that the films are composed of grains with average size $D_{grain} = 0.4$ $\mu$m and that, once a reversal zone has been nucleated, it propagates through the whole grain, statistically the reversal depth is $d_{max} = d_0 + D_{grain}/2 = 1.1 + 0.2 = 1.3$ $\mu$m.

The three methods used to estimate the reversal depth have shown very similar results, on the order of 1.2 $\mu$m. This value will be taken as the average reversal depth on further calculations of fields, gradients and simulations of the microfluidic system.

## 2.5  Micro-Magnetic Imprinting ($\mu$MI)

A third technique for the development of micromagnets has been recently developed in Institut Néel, namely Micro Magnetic Imprinting ($\mu$MI)[83]. It is at the moment being intensively studied, due to its very promising characteristics, but has not been integrated in

any systems presented here. As it is a technique worth discussing, a brief description of it is given in this section.

The Micro Magnetic Imprinting process exploits magnetophoresis to fabricate composite magnetic field sources based on cheap raw materials: magnetic powder or particles (hard or soft) and a non-magnetic carrier matrix are the bases of the technique. In $\mu$MI the magnetic material is positioned by a modulated magnetic field and subsequently embedded by the polymeric matrix. The first tests performed for this technique and reported here are based on commercially available hard magnetic NdFeB powder and PDMS, which is a polymeric material discussed in more detail in Chapter 3. TMP or TOPO magnets are ideal masters for the modulated field. In the example shown here, TMP magnets are used.

The powder used here (MQFP-B) was purchased from Magnequench. The $Nd_2Fe_{14}B$ particles are magnetically isotropic ($\mu_0 M_R \sim 0.8T$), irregular in shape and have and average size of 5 $\mu$m. In the first step of $\mu$MI, the powder is sprinkled onto a TMP magnet. Dry air is then flushed on the powder in order to remove the non-trapped particles. Liquid PDMS is poured on the master/powder and hardened at 60 °C for 2 hours. Finally, the hardened PDMS is peeled off from the master, resulting in a flexible and optically transparent matrix with well-organized micro-magnetic patterns. A flowchart of this process is shown in Figure 2.18a.



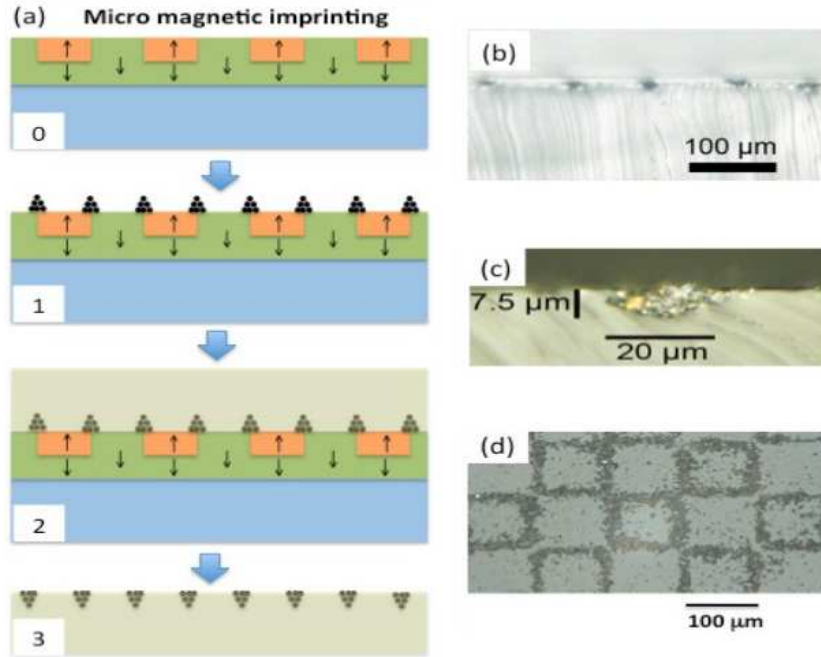Figure 2.18: (a) Schematic diagram of the micro magnetic imprinting process: (1) hard magnetic particles sprinkled onto master structure and magnetophoretically concentrated at the interfaces between neighboring micro-magnets; (2) polymer binder poured over the hard magnetic powders; (3) the solid composite is peeled off the master structure. (b) Side-view, (c) side-view zoomed and (d) plan-view of the magnetic structures.

Optical side view and plan-view images of a composite structure are shown in Figures 2.18b-d. In this example, the magnetic powder aggregates have a depth of about 5 $\mu$m and maximum width of about 20 $\mu$m, and they are separated by a pitch of about 100 $\mu$m, which corresponds to the width of the micro-magnets in the master structure.

## 2.5.1 Stray field analysis

After fabrication the composite structures are magnetized at a field of $\mu_0 H = 4$ T. In order to quantify the stray field produced by the $\mu$MI structures and confirm their potential for any applications, the z-component of the field is measured by Scanning Hall Probe Microscopy (SHPM) and compared to the field measured above the master TMP magnets. A micro-Hall probe of active area 10 $\mu$m, scanned at a height of $18 \pm 5$ $\mu$m above the respective surfaces. 2D images and 1D line profiles are compared in Figure 2.19. Comparison of the 2D images clearly shows that magnetic imprinting does not produce a replica of the master structure, but a new structure defined by the master's stray field pattern in the region where the hard magnetic powders are magnetophoretically concentrated. Though the field profile is more homogeneous above the master structure, the maximum peak-to-peak field value at the height of the Hall probe is similar in both structure types ($\sim 20$ mT). The inhomogeneities in the field pattern produced by the PDMS/powder composite structure are attributed to local variations in the size and packing fraction of the hard magnetic powder agglomerates and should be reduced by an optimization of the fabrication process.
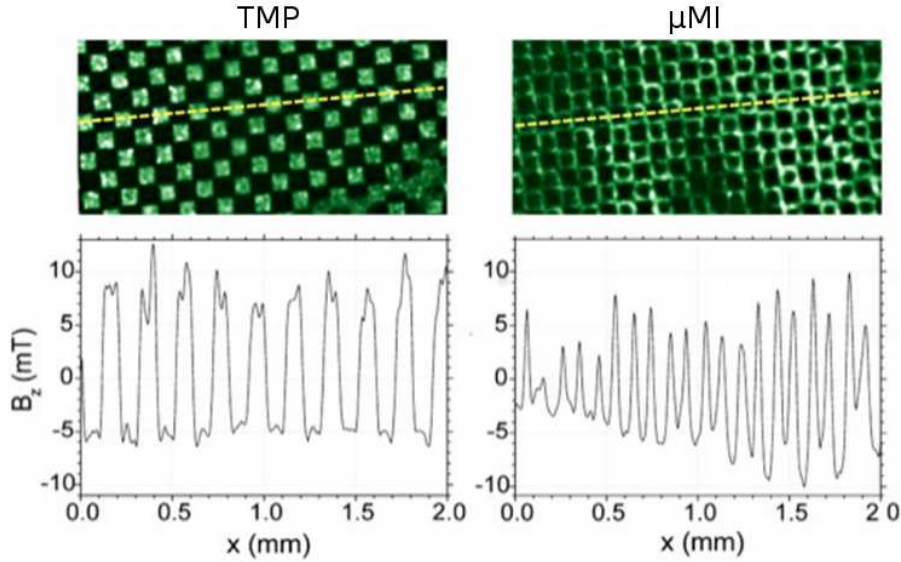


Figure 2.19: Scanning Hall Probe measurements (2D image + 1D line scan) of the stray magnetic field measured at a height of 18 $\mu$m above the master structure (left) and above the composite structure (right)[84].

The distribution of powders in the above-described composite structures is essentially 2D in nature, since the stray fields produced by the thermomagnetically patterned master

structure are very localised, on a length scale comparable to the film thickness. 3D distributions of the magnetic powders can be achieved by applying an external macroscopic magnetic field, this field serving to form extended agglomerates of hard magnetic particles through dipolar interactions, the master structure serving to anchor the agglomerates at specific positions. $\mu$MI in a macroscopic magnetic field, in this case produced by a bulk NdFeB of dimensions $2 \times 2 \times 2$ cm$^3$, placed below the master film, served to increase 10-fold the height of the powder agglomerates enrobed in the PDMS matrix. The influence of the increased volume of magnetic material and the modified demagnetising factor of the 3D structures compared to 2D structures, on the efficiency of magnetophoretic manipulation, is now being studied.

## 2.6   Micro-magnets

The development of micro-magnets is shown here with three different techniques: thermo-magnetic patterning, topographic patterning and micro-magnetic imprinting. The two patterning techniques are based on high-rate triode sputtering with subsequent or simultaneous patterning. The imprinting technique is based on the arrangement of magnetic powder by a first micro-patterned magnet, followed by a step where a polymer based embeds the powder.

Clearly, the most important characteristic these micro-magnets share is the possibility to generate high magnetic fields and gradients in a completely autonomous fashion. Furthermore, this field is limited to a zone very close to the magnet array, with little or no significant field being present a few hundreds of microns far from magnetic film (see Chapter 4. The combination of these two characteristics already gives an important hint of the potential of permanent micro-magnets for downscaled, autonomous micro-devices which can be integrated, or not, to other equipment. The restricted zone of action allows their use along with other equipment, such as microscopes and spectrometers, without interfering in their normal usage.

The three ways of producing micro-magnets also share a few characteristics which make them are very flexible, from different points-of-view:

- Materials - A wide range of magnetic materials can be used, thus allowing a very high adaptability for applications in different environments.

- Integrability - These processes are well-adapted to the standard fabrication techniques and can be integrated to different micro-systems.

- Functionalization - The micro-magnets can be easily covered by a protective, biocompatible or functional material.

There are also a few characteristics which are exclusive for each type of magnet. For instance, topographic magnets can be developed in very thick films, up to 50 $\mu$m (Fig. 2.20a). This higher thickness allows an increase in action distance, which can be an important characteristic for different applications, such as particle attraction or interaction with an

electromagnet in a given micro-device. The minimum lateral feature size is limited by the lithography step during the fabrication of the patterned substrate. Features of a few $\mu$m can be produced, by the thickness-to-width ratio cannot be much higher than 1. As the magnetic field gradient is produced by the topographic variations in the film, all the magnets can be oriented in the same direction. This is an interesting characteristic for an easier development of micro-magnets, since only one magnetization step is required, but a limiting factor if more complicated magnetic arrangements have to be produced.

This last point is where the thermo-magnetically patterned magnets present a great advantage. A magnetically isotropic film can be magnetized in any direction, creating very complex arrangements, such as Halbach arrays (Fig. 2.20b). Also, TMP can be performed in completely flat films or topographic magnets. On the other hand, the maximum reversal depth is, today, limited to around 1.3 $\mu$m, which reduces its action distance. The minimum lateral feature, in this case, is limited by the thermal diffusion during patterning. Up to date, patterns down to 3 $\mu$m have been produced. The fine control of the magnetic field which can be obtained with TMP magnets in flat films is of special interest for numerous applications, in particular in biology for the precise positioning of elements.

Micro magnetic imprinting is a recently developed technique, but has clearly a great potential for numerous applications. Until now, hard NdFeB powder and PDMS are used to produce the $\mu$MI structures and show positive results. However, a vast choice in materials is available. Different polymeric matrices can be used, as well as, hard and soft magnetic powder or particles. The magnetic features in the polymer are observed to be a few $\mu$m thick and tens of $\mu$m wide. The use of an external magnetic field during particle alignment can increase the thickness of the particle agglomerates. Positive preliminary results have been obtained in that direction. The low fabrication and material costs is one of the main advantages of $\mu$MI. This, allied with the flexibility and transparency of the structures, and the possibility to render them biocompatible and functional (Fig. 2.20c), makes $\mu$MI a very important micro-magnetic flux source for a vast range of devices.
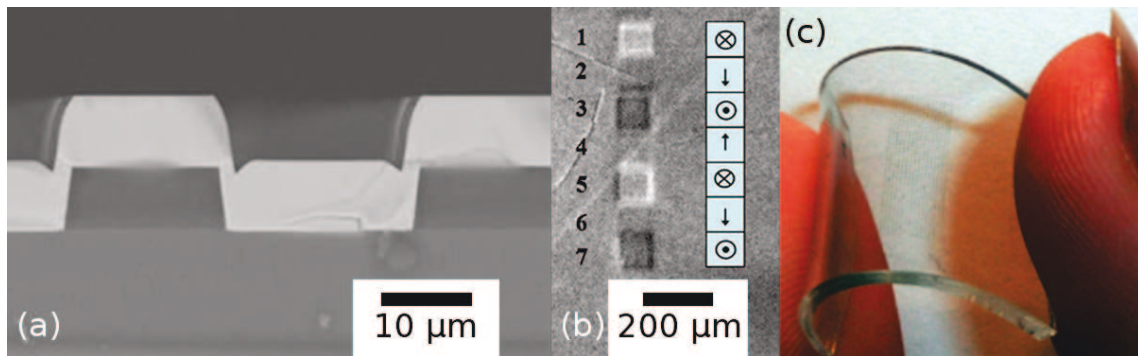


Figure 2.20: A summary of the important and exclusive characteristics associated with each type of micro-magnet. (a) TOPO magnets can be developed in very thick films. (b) TMP magnets allow multidirectional patterning in flat magnets. (c) $\mu$MI structures can be flexible and tranparent.

The next step towards the application of these magnetic flux sources is their integration to micro-systems. Here, micro-object handling in microfluidics is the aimed application, thus the next chapter deals with magnet integration to microfluidic channels. As $\mu$MI is a very recent technique, its presentation in this report is limited to the description shown in this chapter. However, one should keep in mind that the technique has shown very positive results as regards integration and generated field. The further discussion on integration and application of TMP and TOPO magnets can be potentially extended to $\mu$MI structures.

# Chapter 3

# Microfluidic system: development and setup

As previously mentioned, one of the major issues about the fabrication of magnetic micro-systems is the integration of the magnetic part into the device. In this chapter integration of micro-magnets is discussed, focussing on micro-object handling application with microfluidics, especially in the biology field. Even though the magnetic structuration processes at the micron scale are under control, their actual integration often requires to:

- produce a second protective layer;

- render them biocompatible;

- integrate another source of action force.

A polymeric material, namely polydimethylsiloxane (PDMS), is chosen for the system presented here, due to its popularity among biologist and microfluidicians. This popularity is closely related to its low cost and simple use, as discussed further in the chapter. The first and second points on the list above are addressed in a single step: the application of a coating polymeric layer above the magnets. This impermeable layer (to liquids, but relatively permeable to air), is used both to protect the magnets from any aggressive media and to avoid contact of biological elements with non-biocompatible materials.

As micromagnets generate a static magnetic field, another source of acting force has to be integrated in the system in order to obtain movement of particles. The supplemental acting force here is a fluidic force (or drag force or, yet, viscous force). Polymeric microfluidic channels are prepared and positioned above the already polymer-covered magnets, so that a fluid containing the elements of study can be controlled.

Many equipments and methods to control the fluid flow are available. Amongst them, electro-osmotic flow and pressure-driven flow are the most common. Here, a difference of pressure $\Delta p$ between the inlets and outlets of the microfluidic channels induces fluid flow. This $\Delta p$ is obtained with a Fluigent MAESFLO, which also features a flowmeter module.

A PDMS station was installed (in a collaboration between G2Elab, I. Néel and LMGP) in order to develop home-made micro-channels and integration of micro-magnets. A microfluidic station was also installed so that the micro-devices could be tested. The apparatus used for these tests is discussed in this chapter. In this chapter the materials and methods used for the integration of micro-patterned magnets to microfluidics are presented. The flow control equipment will be also described.

# 3.1 Microfluidic system

The most popular material for polymer-based microfluidic systems is polydimethylsiloxane (PDMS). The reasons for its popularity are, mainly, the following properties:

- Optically transparent (to visible light);

- Inert;

- Biocompatible (not completely, but adapted for most biological applications);

- Flexible;

- Non-flammable.

PDMS is composed by silicon, oxygen, carbon and hydrogen, disposed as $CH_3[Si(CH_3)_2O]_nSi(CH_3)_3$ - schematically shown in Figure 3.1. The number of repetitions of the monomer $Si(CH_3)_2O$ is represented by $n$.
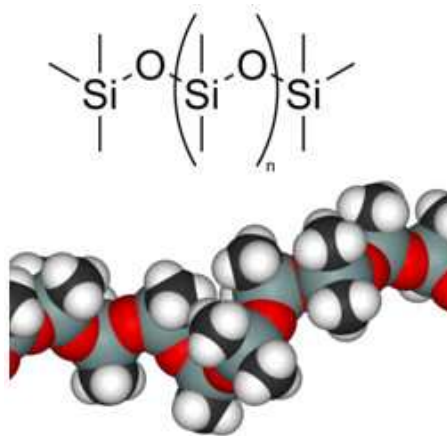


Figure 3.1: Chemical arrangement of PDMS (top) and 3D representation of a molecule (bottom).

Sylgard 184 Elastomer Kit from Dow Corning is used to produce the PDMS components. Its two components - the non-reticulated polymer and the curing agent – are thoroughly mixed in a proportion of 10:1. Due to the introduction of air bubbles in the mixing process, the mixture is degassed in a vacuum chamber until it is completely clear. The absence of air bubbles is important to preserve transparency.

Once the two components are mixed, the polymer starts to reticulate (harden). At room temperature the hardening process may take up to three days. This time is reduced

to 15-20 minutes if the temperature is increased to $100\,^{\circ}$C. If magnetic films are present, the temperature is limited to 50-60$\,^{\circ}$C, due to the negative effect of temperature in the magnetization of the film.

Both TOPO and TMP magnets are usually covered by a PDMS layer before the microfluidic channel is positioned above them. The presence of this layer increases the minimum object-film distance, thus reducing the maximal magnetic force. Depending on the application, this reduction can be an advantage or a drawback, as demonstrated further. The PDMS layer also renders the system biocompatible (for most applications) and acts as a second protection from oxidation of the magnets. Moreover, it allows a chemical bond of this component to the PDMS component containing the microfluidic channel.

For TOPO magnets, the main reason to use this PDMS layer is to obtain a planarized surface. Otherwise, positioning a microfluidic channel above the magnets and precisely controlling the fluidic flow would be impossible. An effort to produce flat, thin and reproducible layers of PDMS above TOPO magnets was done in a collaboration with Bruno DE SOUSA ALVES during his Master internship and will be presented here.

The integration of TMP and TOPO magnets to PDMS are discussed in the further sections. Micro-channel preparation based on replica molding is also presented, followed by the methods used to assemble the systems.

## 3.1.1   PDMS spin-coating above TMP

In the case of TMP magnets, the surface is already flat, excepting the bumps created by the Nd-rich phase, as previously discussed. However, the use of a PDMS layer between the microchannel and the magnetic film can be interesting for a number of reasons:

- Create a second protective layer and avoid contact between the flowing liquid and the magnets;

- Allow the PDMS-PDMS bonding to seal the channel using oxygen plasma, since no chemical bonding is produced between the Ta layer and PDMS. (Further details are discussed in Section 3.1.4;)

- Regulate the minimum particle-magnet distance and, thus, the maximum magnetic force in order to perform precisely controlled magnetic capturing and deviation.

A spin-coater (SPS SPIN150) is used to produce flat, homogeneous PDMS layers above the TMP magnets. The final layer thickness is controlled using a standard mixture of the liquid polymer and varying the rotation speed, the acceleration of the spin-coater and/or the duration of the process. Other parameters such as small variations in the non-cross-linked PDMS/curing agent ratio or the substrate roughness have been tested and do not present a significant influence on the layer thickness. It can be observed in Figure 3.2 that thicknesses ranging from a few $\mu$m to several tens of $\mu$m can be obtained by this method.
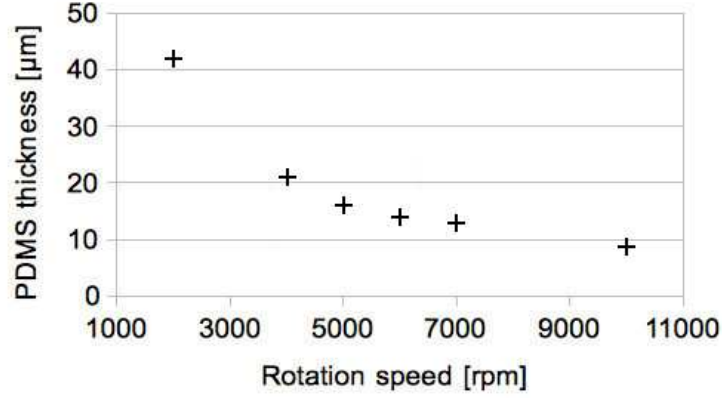
Figure 3.2: Evolution of the PDMS layer thickness as a function of spin-coating rotation speed, considering an acceleration of 1000 rpm/s and a duration of 30 s.

The homogeneity of the PDMS layer, however, decreases if thick layers are spin-coated: for thicknesses above 100 $\mu$m – rotation speeds below 1000 rpm - a clear edge effect can be observed, as PDMS accumulates on the edges of the sample, compromising the flatness of the layer.

In the case a much thinner layer is needed, for instance for the attraction of nanoparticles, a solvent can be added to the PDMS mixture in order to reduce its viscosity. Vézy et al. obtained positive results using different ratios of heptane, as reported in [85]. These solvents are generally volatile and can be naturally removed from the spin-coated layer.

### 3.1.2 Null-patterning of TOPO magnets

The irregular surface of the topographically patterned magnets, although necessary to generate a magnetic field gradient, is a major drawback for most applications. The preparation of microfluidic channels above these magnets, for instance, requires a flat surface.

Chemical-Mechanical Planarization (CMP) could be used to remove the upper magnets and silicon patterns, as previously shown in Figure 2.9. This method has been successfully used, for instance, in the development of thick electroplated copper windings. However, this technique is time consuming, expensive and not adapted to deep features. Due to its time cost and need of further optimization, it is not used in this work. The planarization (also called null-patterning) by filling up the patterns with another material without removing the existing patterns and magnets is preferred. Figure 3.3 presents the parameters used in the study of planarization of TOPO magnets. The fixed dimensions coming from the topographic features and the studied dimensions which varied with the null-patterning process are:

- $w_f$: feature width;
- $d_f$: feature depth;

76

- $d_{PDMS}$: thickness of PDMS above upper magnets;

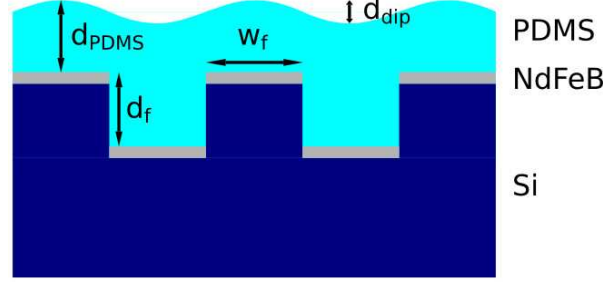- $d_{dip}$: dip-depth (the peak-to-valley variation in the PDMS thickness)



Figure 3.3: Schematic of the parameters studied in the null-patterning process.

*First attempts of null-patterning*

A few different methods of planarization have been developed at first by Dan O'Brien (post-doctoral fellow) and Alain Masse (PhD student), and subsequently by Bruno de Sousa Alves (intern under my supervision). Since spin-coating of PDMS on TOPO magnets produces very poor results due to its topography, alternative methods had to be developed. These methods consist of pouring liquid PDMS on the sample, then placing it between two supports and applying a compressive force on the system. Glass plates were used as supports and three different methods were used to apply the force on the ensemble glass/sample/PDMS:

- Vacuum packing: the ensemble is put in a plastic bag which is pumped and sealed;

- Paper clips: the glass plates are clipped in each side using standard paper clips;

- External mass: a mass is put above the glass plate in order to apply a constant controlled force.

Two issues have been noticed with these methods. At first, once the PDMS is compressed between the glass plates, the hardening period becomes much longer. Tests run at room temperature and at $50 - 60\,^{\circ}$C have shown that the PDMS layer may take a few days to harden. The second issue observed is that the PDMS layer remains stuck on the glass plate. A considerable force is necessary to unstick the two parts, which can cause the polymer above the magnets to deform.

In order to address these problems, a layer of a photoresist was spin-coated on the glass plate prior to the assembling of the two parts. Once the PDMS layer was hardened, acetone was used to remove the resist and the glass plate would come out easily. This method showed relatively good results concerning the unsticking part, however the removal of the resist with acetone took much longer than expected. Since acetone attacks the resist only at its edges,

it may take tens of minutes to completely remove the resist layer. The hardening time was also increased, since the temperature of hardening had to be decreased due to its negative effect on the resist: bubbles were created during the process and their shape remained on the PDMS layer afterwards. Note that PDMS slightly swells due to acetone, but deswelling by heating to around 50 °C is possible, without affecting its properties.

Mechanical profilometry was used at first to measure the profiles of the PDMS layer, however due to the fact that it is a contact technique, artifacts were often added in the measurements. This technique was then replaced by optical profilometry, which is a non-contact technique and with which non-destructive measurements of PDMS can be performed, due to the PDMS transparency.

Even though some issues have been observed with these methods, the results concerning the PDMS layer thickness and the flatness of the layer were positive. A minimum layer thickness ($d_{PDMS}$) of 4 $\mu$m was obtained, depending on the process used. Thicknesses up to a few tens of $\mu$m could also be produced. Concerning the dip-depth ($d_{dip}$) and the roughness of the PDMS surface, satisfactory results were also observed. Figure 3.4a shows a typical 3D measurement performed with an optical profilometer. In this figure a flat surface is observed, around a zone which was influenced by an air bubble.
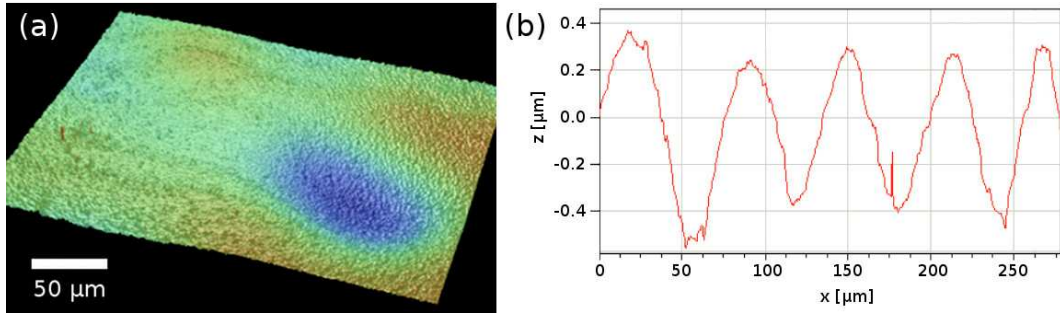


Figure 3.4: (a) 3D measurement of a null-patterned surface. The surface is flat, excepting the bump created by an air bubble. (b) A profile measurement along a line in the flat part. Negligible roughness and a dip-depth of a few hundreds of nm are observed.

A measurement along a line in the flat part (Figure 3.4b) shows a negligible roughness and a dip-depth of a few hundreds of nanometers. Taken into account that the peak and the valley considered in the measurement of the dip-depth are separated by a distance of at least one feature width, the influence of this variation on particle trajectory is negligible.

*Successful attempt: immersion*

A different method was proposed by Bruno Alves de Sousa and showed encouraging results at the first attempts. The idea, much simpler than the previous ones, consists of the direct immersion of the TOPO magnet, upside-down, in a recipient filled with liquid PDMS.

The step-by-step of the process is straight-forward:

- A plastic box is used as recipient for the sample and PDMS (Figure 3.5a);

- Liquid PDMS is poured on a TOPO magnet and degassed in order to remove any air bubbles which can remain between the topographic patterns (Figure 3.5b);

- The sample is inverted an placed in the box (Figure 3.5c);

- The box is filled up with PDMS and put in a muffle furnace at 50 °C (Figure 3.5d);

- After hardening, the PDMS with the embedded sample is cut and removed from the box (Figure 3.5e);

- The null-patterned sample is ready for integration to a microfluidic channel (Figure 3.5f).
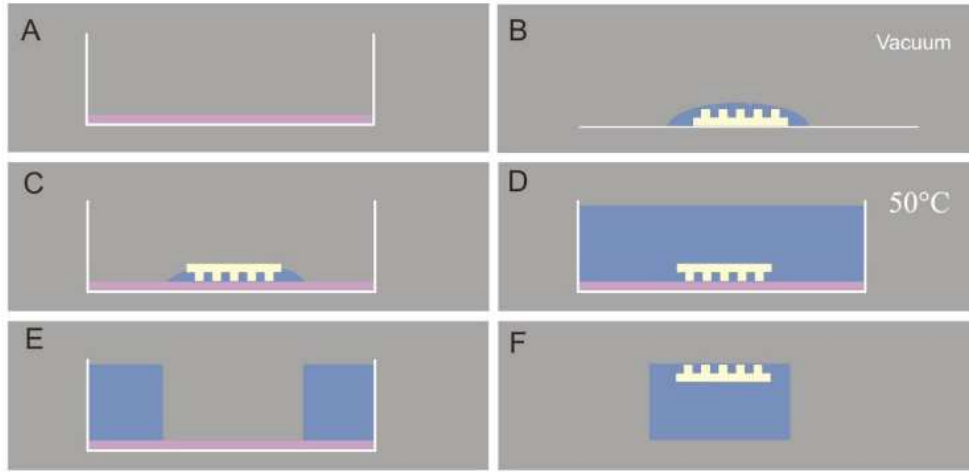


Figure 3.5: Schematic of the steps used to produce a null-patterned TOPO magnet using PDMS.

Different pattern dimensions are used for null-patterning with this method. A typical thickness of 35 $\mu$m is found in all the cases, the dip-depth varying with the feature size. Figure 3.6a shows a top-view of the final PDMS surface above the magnets. One can notice a gradient of height increasing from bottom-left to top-right of the figure, caused by a tilt in the sample during the measurement by optical profilometry. Rounded features can also be noticed, indicating that the feature dimensions ($\varnothing$ 50 $\mu$m circles) create bumps on the PDMS surface. A line scan (Figure 3.6b) clearly confirms the gradient coming from the tilt in the sample and the bumps from the topographic features, which are aproximately $100 - 200$ nm high. A reproduction of the plastic box surface roughness is also observed on the PDMS surface.

Figure 3.6: (a) 3D measurement showing a successfully null-patterned sample. (b) A line scan confirms that the bumps created by the topographic features are in the nm range and do not interfere with particle flow. The "noise" in the measurement comes from roughness of the plastic box.

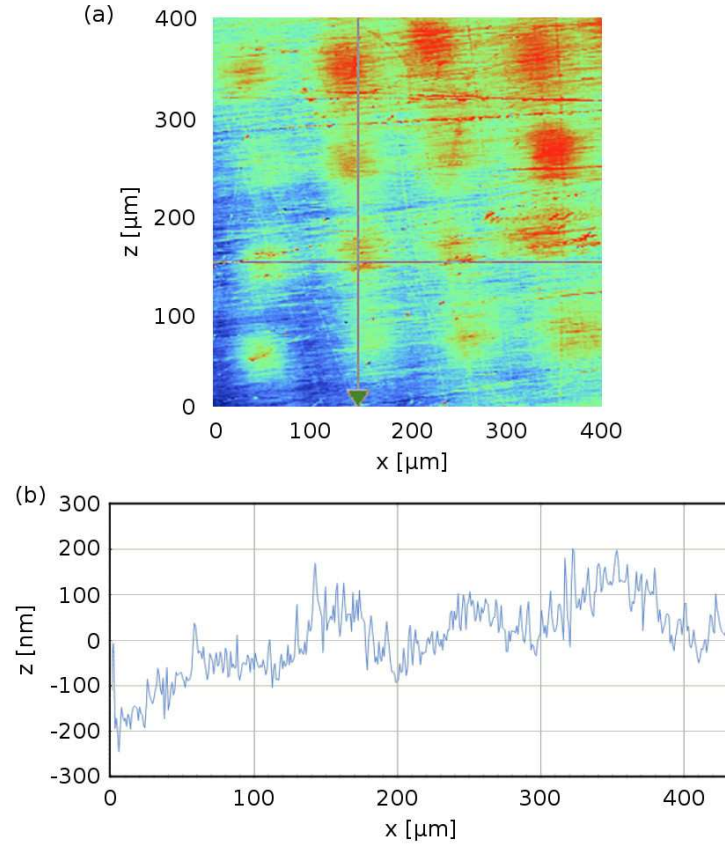*Optimization of the process*

The dip-depths observed in the first tests in immersion are small and do not disturb the flow of particles. However, the PDMS thickness obtained (35 $\mu$m) can be too big, specially for the capture of nanoparticles, since it will correspond to the minimum particle-magnet distance. Yet, even though the plastic box-PDMS bonding is considerably weaker than the glass-PDMS bonding, it can still generate irregularities in the PDMS surface. For those reasons, further optimization methods for the null-patterning process were developed.

In order to solve the PDMS-substrate bonding problem, a glass plate with a layer of parylene is used as substrate. Parylene is a biocompatible polymer of composition $C_8H_8$, which can be deposited by evaporation as a thin film. PDMS and parylene do not naturally bond during processing, thus solving the sticking problems observed in the previous null-patterning tests.

The first approach to reduce the PDMS thickness consisted of decreasing the viscosity of PDMS. Toluene was added to PDMS at different ratios and the null-patterning process was carried out the same way. Severe irregularities caused by the creation of bubbles was

noticed with all the mixtures. As toluene is a highly volatile, it evaporates and creates paths on PDMS during the process. Figure 3.7a shows an example of the sample surface for the case where a toluene-PDMS mixture was used. The dip-depth in this case can reach several $\mu$m. This method has been abandoned after the preliminary tests.
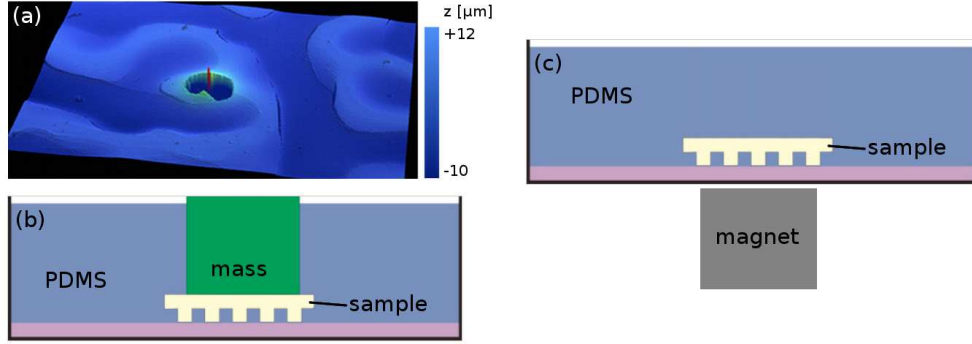


Figure 3.7: (a) 3D image measured by optical profilometry showing the irregularities caused by the evaporation of toluene; (b) schematic showing how a force is applied on the sample using a weight; (c) schematic of the use of a macromagnet to pull down the sample immersed in PDMS.

Another method developed to reduce the PDMS thickness consists of adding a weight above the sample, as shown in Figure 3.7b. This method efficiently reduces $d_{PDMS}$ in an homogeneous fashion. It brings also the possibility to easily control the force applied on the sample by changing the weight and, thus, control the PDMS thickness, as discussed in the next section. However, an inconvenient of the method is that the weight remains embedded in the PDMS behind the sample and renders the system larger than usual.

In order to apply the force on the sample without adding unnecessary volume to it, a technique taking advantage of magnetic interactions is used. A bulk magnet is positioned below the recipient, close to the sample, as show in Figure 3.7c. An attractive interaction between the magnets in the sample and the bulk magnet occurs, pulling down the sample. This method is also efficiently used to reduce the thickness of the PDMS layer (6 $\mu$m, as opposed to 30 $\mu$m obtained in similar conditions, without the magnetic force), but a fine control of the force applied on the sample is more difficult to obtain. Further studies concerning this method are underway.

A systematic study of the different, successful techniques was performed in order to better understand the processes and design a protocol of the techniques.

*Systematic study*

The first study concerns the influence of the feature characteristics on the thickness and the dip-depth of the PDMS layer. Tests are at first carried out using samples with varying feature width ($w_f$) and a feature depth ($d_f$) fixed at 100 $\mu$m. The PDMS thickness observed for all the samples is around 35 $\mu$m with no significant variation related to the feature width.

81

Figure 3.8a shows that $d_{dip}$ increases as $w_f$ increases. This effect is much more evident for features ranging in size from 25 to 250 $\mu$m. In the case of wider features, the dip-depth increases smoothly and appears to stabilize at around 8 $\mu$m for features in the mm range.
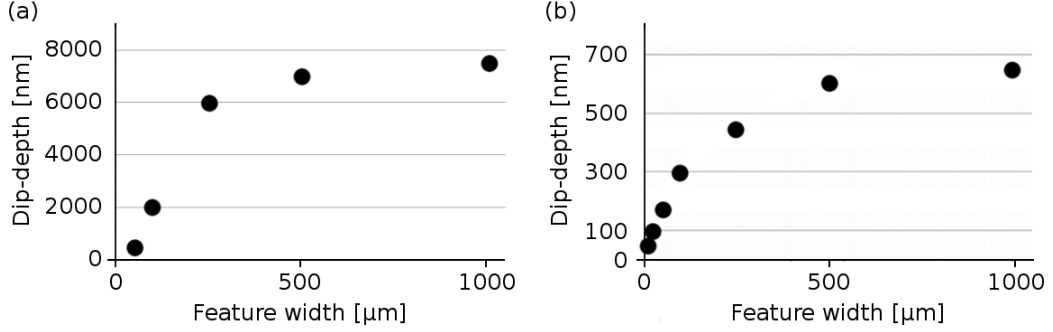


Figure 3.8: Evolution of the dip-depth on the PDMS layer as a function of the feature width using samples with (a) 100 $\mu$m-deep and (b) 20 $\mu$m-deep features.

The dip-depth observed in these samples is associated to a contraction of PDMS during the curing step. The effect is much less important when using smaller features, since the closeness of the pillars retain more significant contractions. The few percent contraction can be much more significant when considering the wider surface available in samples with bigger features.

In order to analyze the influence of the characteristic depth on the null-patterned surface, further tests are carried out using samples with similar feature widths, but a depth of 20 $\mu$m. As it can be observed in Figure 3.8b, the profile of dip-depth as a function of feature width is similar: the variation of $d_{dip}$ is much more significant for smaller lateral dimensions and tends to stabilize with features in the mm range. However, both the values of $d_{PDMS}$ and $d_{dip}$ are considerably different in this case. The PDMS thickness observed with the less deep sample is approximately 65 $\mu$m, almost twice the thickness observed with deeper patterns. The dip-depth, on the other hand, reduced by roughly one order of magnitude, ranging from 50 to 650 nm, approximately.

Concerning the effect of using a weight on the sample, tests are performed using masses ranging from 0 to 5 g. The thickness of the PDMS layer is observed to decrease significantly from the initial 35 $\mu$m without a mass to around 5 $\mu$m using a mass of 2.1 g. Increasing the mass beyond this value does not seem to affect the layer thickness, as shown in Figure 3.9.
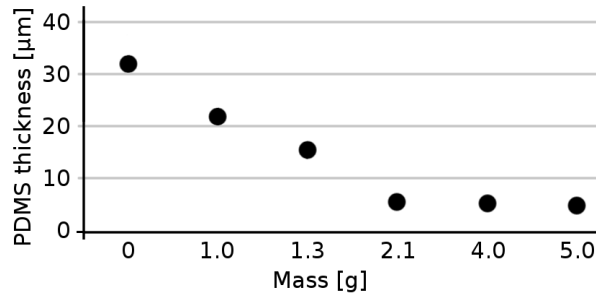
Figure 3.9: Evolution of the PDMS thickness as a function of the mass used to apply a force above the sample.

### 3.1.3 Micro-channel preparation

The microfluidic channels used here are prepared by replica molding. The molds are produced by soft lithography using the dry film photoresist Dupont Riston MultiMaster 540. This film has the advantage of being solid and can be directly applied on a substrate without the need of spin-coating. However, its thickness is fixed at 38 $\mu$m, thus, the channel height is limited to multiples of this value.

The dry film photoresist, as most of the standard photoresists, is insolated using UV light with wavelength of 365 nm. The masks used during irradiation are design in a CAD software and printed in plastic. After exposure to UV light, the film is developed with sodium carbonate dissolved in water.

The non-reticulated PDMS mixture is poured on the mold, hardened for a few hours at 50-60 °C and, finally, unmolded.

### 3.1.4 Assembling

Once the magnetic films are covered with PDMS and the micro-channels are prepared, the two parts can be assembled in order to obtain a closed system in which a liquid solution will be pumped. In general, applying a small, constant pressure on the system is sufficient to insure a good contact and avoid leaks. However, other methods can be used to obtain a stronger bond between the two components. A common method is to apply a thin layer of curing agent on one of the surfaces prior to putting the components in contact. It provides a better bonding, but it is not well-suited for high pressures and part of the curing agent may remain inside the channel.

The best bonding method – and the one used in the systems presented here – is to create an oxygen bond between the two surfaces. In order to do so, both surfaces are, at first, exposed to oxygen plasma, which will replace the superficial $CH_3$ groups by $OH$ groups. The two modified surfaces are then put in contact and and oxygen bond is created between the Si atoms. Water is liberated in the process, as shown in Figure 3.10.
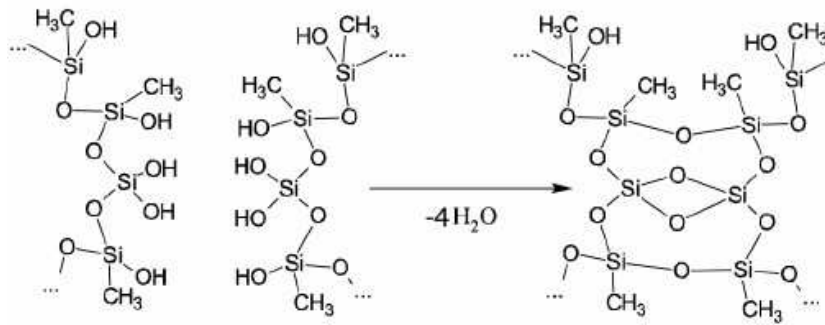
Figure 3.10: The surfaces of PDMS which were modified ($CH_3$ groups replaced by $OH$ groups) are put in contact and an oxygen bond is created, liberating $H_2O$.

## 3.2 Microfluidic flow control

The flow of a liquid inside the microfluidic channel can be controlled by several methods, for instance:

- Pressure difference;

- Flow rate;

- Capillarity.

The most commonly used method is the control of flow rate by means of a syringe pump. This apparatus consists of a syringe holder and a mobile part connected to the syringe piston which moves at a speed defined by the user. If the dimensions of the syringe are known, the flow rate can be defined by the piston velocity.

Syringe pumps are quite simple and inexpensive equipments used for most part of the basic microfluidics. However, a few drawbacks limit its applications:

- The number of channels (syringes which can be hold simultaneously) is often limited to 4 and are not independent, since they are controlled by the same moving piece. A fine adjustment of the flow rate in each channel is, thus, impossible;

- In order to determine the pressure applied in each channel, pressure gauges have to be connected to the system;

- The response time is high – from seconds to minutes – and can generate delays which are too long for "live" control of the systems.

The first tests in microfluidics for this project were performed using a KD Scientific Legato 100 syringe pump. The limitations, mainly related to the response time, were soon identified as a major concern for the separation of particles and the equipment was replaced.

The best alternative available was found to be a Fluigent MFCS (Microfluidic Flow Control System), described in the next section.

### 3.2.1 Pressure control

Fluigent is a french company which produces pressure-driven microfluidic flow controllers based on the patented FASTAB technology (developed in 2004). This technology was developed in order to overcome the high response time issue of the available flow controlling techniques. It insures quick response and settling combined with very high stability and precision (oscillations around the set pressure/flow rate are often observed in other systems).

The MFCS can contain up to 8 channels connected to flowmeters, the whole controlled with a graphical user interface (GUI). Each channel is independent, i.e., the desired pressure or flow rate can be set to a channel without influencing the others.
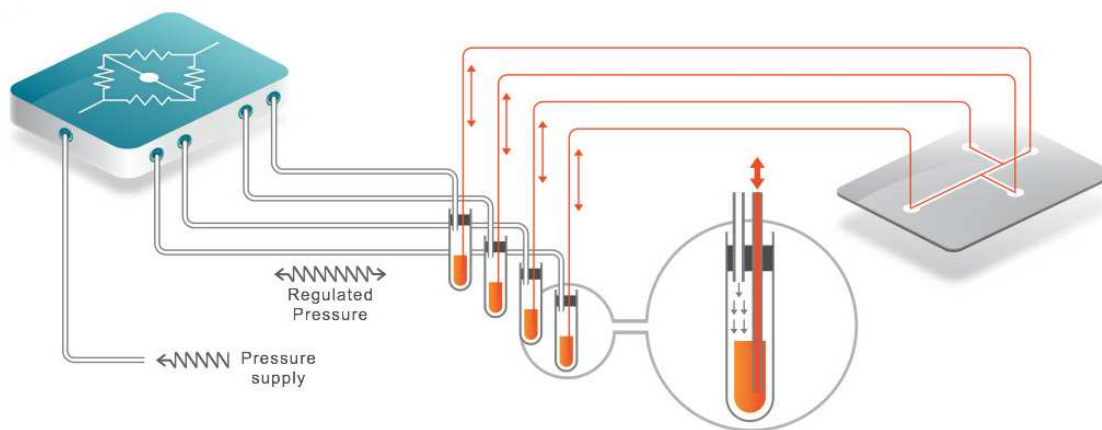


Figure 3.11: Schematic showing the ensemble of the MFCS: a computer controls the pressure system; air pressure pushes up the liquid in the recipients; the liquid flows through the microfluidic system. [86]

Figure 3.11 shows a schematic of the microfluidic apparatus. The GUI is used to set and observe the different pressures applied on each channel. The MFCS is connected to a pressure supply (usually air or argon) and to a sample holder, which is called FLUIWELL and consists of a pressure inlet and a liquid inlet/outlet. Finally, the FLUIWELL is connected to the microfluidic system. An optional flowmeter can be used in this last connection.

## 3.3   Complete setup

Using the techniques presented in this chapter, the micromagnets are integrated into PDMS-based systems containing microfluidic channels. Fluids are flown through these channels in a controlled fashion due to a pressure difference created by a pressure controller. A graphic interface with a computer allows real-time control of the pressures applied to channel inlets and outlets.

As mentioned, the micro-channel can be sealed with mechanical force during its use. A simple system for holding the micro-systems' parts together was developed and is shown in Figure 3.12. The aluminum pieces hold the magnetic system by applying a pressure via the screws, while a blue and a red liquid flow through the channel. These liquids can be seen flowing out of a single channel in separate outlets, again proving the interest of laminar flow for fluid and/or particle handling.
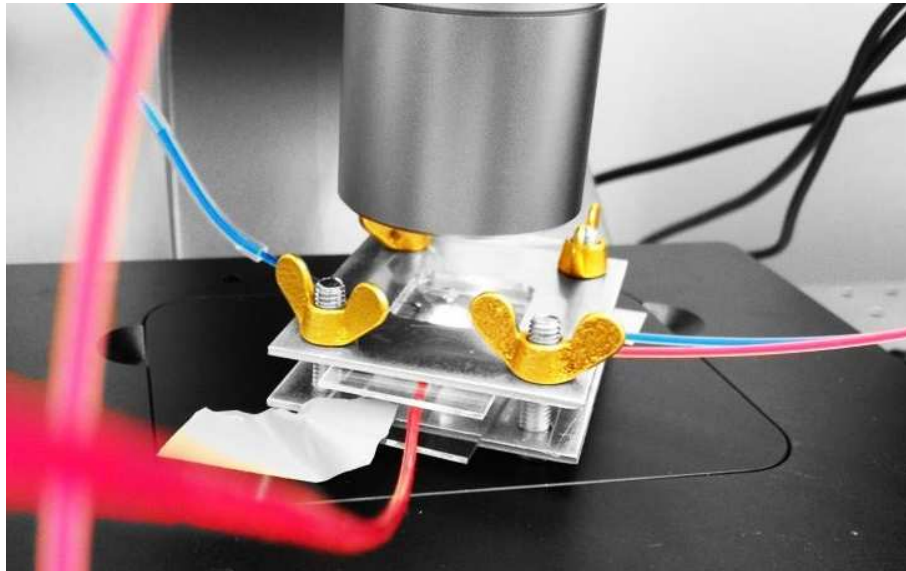


Figure 3.12: A mechanical force is sufficient to hold the PDMS parts together and sealing the micro-channel. Fluids flow normally through the channel without leaking.

The whole ensemble is shown in Figure 3.13, with a zoom on the microfluidic system presenting the results of the different integration steps.
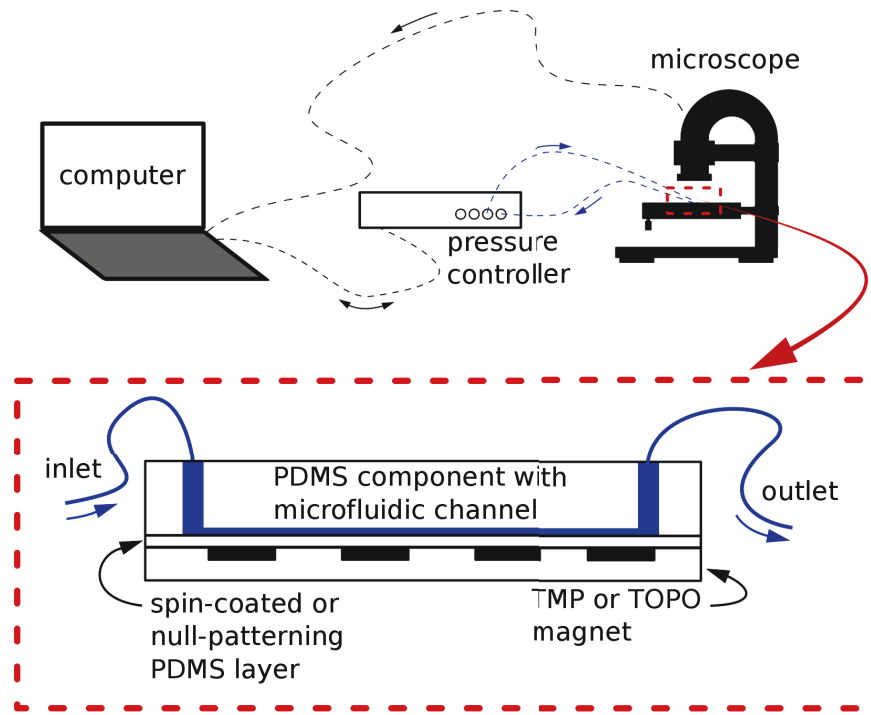
Figure 3.13: The different components used for the control and observation of the complete microfluidic systems. The system itself with its different parts is shown in the zoomed inset.

Once the microfluidic system with integrated micromagnets is ready and connected to the side-equipment, actual positioning and guiding of particles can occur. Before stepping into the experimental results (Chapter 5), a theoretical model is developed in the next chapter. This model is, in fact, used prior to the development of the system, as a tool for design and optimization of the dimensions and parameters.

# Chapter 4

# Modeling particle handling with microfluidics

In this chapter an analytical model of the complete device is developed both to achieve a better understanding of the phenomena involved in particle manipulation and as a tool for device optimization.

Different arrangements of micromagnets are considered, taking into account the previously discussed constraints of magnetic microstructuration for TMP and TOPO patterns. The magnetic fields and field gradients are calculated and plotted so as to characterize and select the adapted magnetic configuration for each application.

Particle responses to a magnetic field are also modeled with the non-linear Langevin law and compared to experimental magnetization curves, in the case of superparamagnetic particles. The forces acting on the particles and their displacement in a microfluidic system are simulated and particle attraction predicted.

The required conditions for particle capturing and continuous sorting are determined theoretically. The basic parameters to be used in experimental systems are listed so as to optimize the devices which are presented in Chapter 5.

## 4.1  Model of the magnetic stray fields

The magnetic fields generated by permanent magnets are usually calculated using one of two approaches: Coulombian or Amperian. The Amperian approach consists of representing the magnet by equivalent surface currents. Figure 4.1a and 4.1b show, respectively, a cuboid magnet and its Amperian equivalent. Surface charges (Figure 4.1c) are considered in the Coulombian approach. This second approach is chosen to calculate the stray field of the out-of-plane or in-plane magnetized, cuboid micro-magnets. Note that the field generated by a magnet which has a magnetization aligned with a given angle to one of the main axes of the cuboid solid can be calculated by superimposing two or three equivalent, axially magnetized solids.
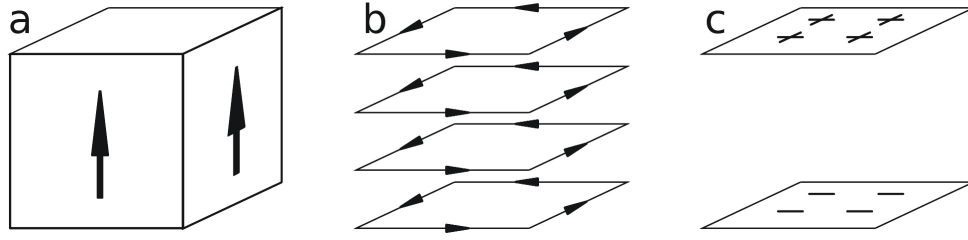
Figure 4.1: A (a) cuboid magnet can be modeled by (b) equivalent currents (Amperian approach) or (c) equivalent charges (Coulombian approach).

The magnetic field $dB$ created by a linear current element $I dl$ at a distance $r$ from it can be calculated by Biot-Savart's law, which states that

$$dB = \frac{\mu_0 I}{4\pi} \frac{dl \times \vec{r}}{r^2} \tag{4.1}$$

where $r$ is the displacement vector from current element to the point of interest and $\vec{r}$ its unit vector. This equation can be rewritten in the Coulombian form, where the current element is replaced by an equivalent "magnetic charge" element. The field created by this element – schematically shown in Figure 4.2 is thus

$$d^2 B = \frac{\mu_0 \vec{M} \vec{n}}{4\pi} \frac{\vec{r}}{r^2} dx\, dy \tag{4.2}$$

where $M$ is the magnetization of the magnet and $\vec{n}$ is the vector normal to its surface.
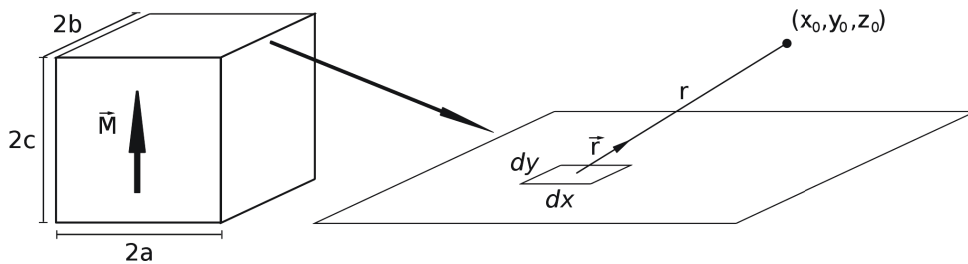


Figure 4.2: Schematic of the integration intervals for the Coulombian approach.

The $x$ component of the magnetic field created by the positive sheet can be, then, calculated by

$$B_x = \int_{-a}^{a} \int_{-b}^{b} \frac{M(x_0 - x)}{[(x_0 - x)^2 + (y_0 - y)^2 + (z_0 - c)^2]^2} dx\, dy \tag{4.3}$$

90

which yields

$$
\begin{aligned}
B_x &= \frac{\mu_0 M}{4\pi} \ln \left[ \frac{y_0 + b + \sqrt{(x_0 - a)^2 + (y_0 + b)^2 + (z_0 - c)^2}}{y_0 - b + \sqrt{(x_0 - a)^2 + (y_0 - b)^2 + (z_0 - c)^2}} \right. \\
&\quad \left. \times \frac{y_0 - b + \sqrt{(x_0 + a)^2 + (y_0 - b)^2 + (z_0 - c)^2}}{y_0 + b + \sqrt{(x_0 + a)^2 + (y_0 + b)^2 + (z_0 - c)^2}} \right]
\end{aligned}
\tag{4.4}
$$

The $B_y$ and $B_z$ components are calculated the same way, yielding

$$
\begin{aligned}
B_y &= \frac{\mu_0 M}{4\pi} \ln \left[ \frac{x_0 + a + \sqrt{(x_0 + a)^2 + (y_0 - b)^2 + (z_0 - c)^2}}{x_0 - a + \sqrt{(x_0 - a)^2 + (y_0 - b)^2 + (z_0 - c)^2}} \right. \\
&\quad \left. \times \frac{x_0 - a + \sqrt{(x_0 - a)^2 + (y_0 + b)^2 + (z_0 - c)^2}}{x_0 + a + \sqrt{(x_0 + a)^2 + (y_0 + b)^2 + (z_0 - c)^2}} \right]
\end{aligned}
\tag{4.5}
$$

and

$$
\begin{aligned}
B_z &= \frac{\mu_0 M}{4\pi} \left[ \arctan \frac{(x_0 + a)(y_0 + b)}{(z_0 - c)\sqrt{(x_0 + a)^2 + (y_0 + b)^2 + (z_0 - c)^2}} \right. \\
&\quad + \arctan \frac{(x_0 - a)(y_0 - b)}{(z_0 - c)\sqrt{(x_0 - a)^2 + (y_0 - b)^2 + (z_0 - c)^2}} \\
&\quad - \arctan \frac{(x_0 + a)(y_0 - b)}{(z_0 - c)\sqrt{(x_0 + a)^2 + (y_0 - b)^2 + (z_0 - c)^2}} \\
&\quad \left. - \arctan \frac{(x_0 - a)(y_0 + b)}{(z_0 - c)\sqrt{(x_0 - a)^2 + (y_0 + b)^2 + (z_0 - c)^2}} \right]
\end{aligned}
\tag{4.6}
$$

The three components of the field created by the negative sheet are calculated the same way and superposed to the components calculated above.

The magnetic field created by several magnets is calculated at any point in space using the previously shown equations. The magnetic field gradient can be, then, easily calculated. In order to determine the magnetic force acting on an object, its magnetic response in a given field has to be characterized. The magnetic responses of typical magnetic particles used in this work are modeled in the next section.

## 4.2   Particle responses

The superparamagnetic particles used in this report are mainly spherical (excepting the ⌀ 200 nm particles, as it will be discussed in Chapter 5) and polymer-based:

- Diamagnetic (also called here non-magnetic) particles: solid polymer-based spheres. The polymer is usually latex or polystyrene. The diamagnetic response relative to the negative magnetic susceptibility of these particles is very low ($10^{-5}$).

- Superparamagnetic (SPM or, simply, magnetic) particles: a spherical polystyrene matrix with iron oxide inclusions embedded in it. The inclusions are randomly dispersed in the matrix. The magnetic susceptibility in this case is in the range of 1 - 50, before saturation.

Iron oxide inclusions are, in general, found in the form of maghemite ($Fe_2O_3$) or magnetite ($Fe_3O_4$). The nanoinclusions are often in the dimension range of 1 to 10 nm, this dimension strongly influencing the global magnetization of the particle when submitted to a magnetic field. The dispersion in size of the nano-inclusion also plays a significant role in the global magnetization.

The calculations performed further in this Chapter show that several orders magnitude separate the forces acting on SPM and diamagnetic particles. This is due to the very different magnetic susceptibilities, as mentioned above. The force created by the magnet arrays on the diamagnetic particles is negligible compared to the one acting on the SPM particles. Hence, this force will not be considered in the further calculations. Magnetic responses of SPM particles only are considered.

In the presence of a magnetic field $H$, a magnetic particle is submitted to a global force, due to the action of the field on all the constituent nanoinclusions. On one inclusion ($i$), of radius $r_{np(i)}$ and volume $V_{np(i)}$, the magnetic force is given by

$$F_m = \mu_0 V_{np(i)} M_{(i)} \nabla H \tag{4.7}$$

where $M_{(i)}$ is the nanoparticle magnetization, given by the Langevin function

$$M = M_0 \, L(x_{(i)}) = M_0 \left\{ \coth(x_{(i)}) - \frac{1}{x_{(i)}} \right\} \tag{4.8}$$

$M_0$ represents the 0 K magnetization and

$$x = \frac{\mu_0 V_{np(i)} M_0 H}{k_B T} \tag{4.9}$$

For the particle as a whole, the average magnetization is obtained by summing up the moments of all ($n$) nanoparticles, and normalizing with respect to the total magnetic volume $V_{mag}$, i.e.,

$$M = \frac{M_0 \sum_{i=1}^{n} P(r_{np(i)}) V_{np(i)} L(x_{(i)})}{V_{mag}} \tag{4.10}$$

where

$$V_{mag} = \sum_{i=1}^{n} P(r_{np(i)}) V_{np(i)} \tag{4.11}$$

and $P(r_{np(i)})$ is the probability of a given nanoparticle to have the radius $r_{np(i)}$.

Magnetization measurements were performed in order to determine the properties (size and superparamagnetic behavior) of the Fe-oxide inclusions embedded in the polystyrene "magnetic" particles used in this work. Fig. 4.3 shows the normalized magnetization curves of ⌀ 2.8 $\mu$m and ⌀ 1.0 $\mu$m particles, in blue and red, respectively, taken as examples. Other particles used here do not show B(H) loops significantly different from these to justify a case-by-case study.
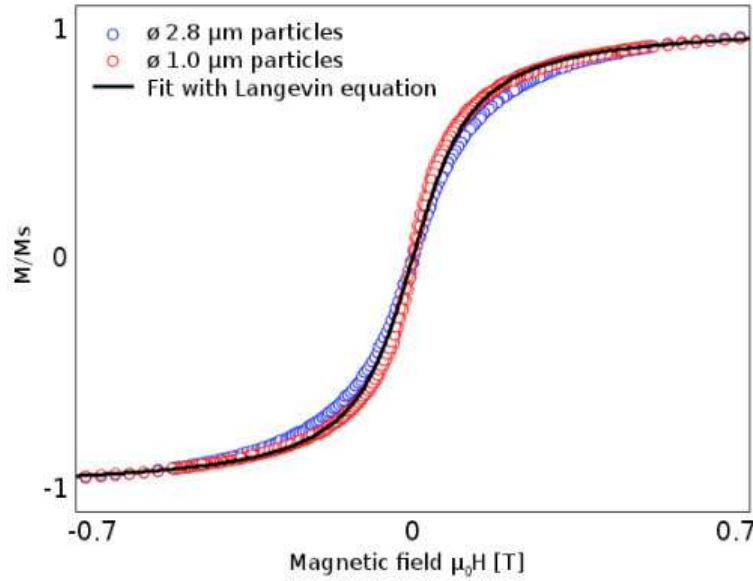


Figure 4.3: Magnetization curves of particles and fitting.

Fitting the curves with the previously mentioned equation gave an inclusion size of 3.3 nm with standard deviation 3 nm (2.8 $\mu$m particles) and an inclusion size of 3.6 nm with standard deviation 3 nm (1 $\mu$m particles). An average radius of 3.5 ± 3 nm is, thus, used in the further calculations. An average magnetization of 460 kA/m is calculated and taken as a fair approximation after the measurements performed for several particles.

## 4.3   TMP versus TOPO magnets

The constraints associated with the fabrication of TMP and TOPO magnets are quite different, inducing different possible dimensions for each type of magnet, as discussed in Chapter 2. However, the typical lateral dimensions used presently are quite similar, ranging from 50 to 200 $\mu$m. The thicknesses are, of course, very different: TMP magnets are, for the moment, limited to a depth of reversal of 1.3 $\mu$m, while TOPO magnets can be deposited with thicknesses up to 50 $\mu$m (even more, in some cases).

In this section the magnetic fields and field gradients created by both types of magnets are calculated and compared for a set of characteristic dimensions: TMP magnets with the typical thickness of 1.3 $\mu$m and TOPO magnets with thicknesses of 10 $\mu$m and 30 $\mu$m. The lateral dimensions of these magnets are varied in the three usual dimensions used experimentally: 50 $\mu$m, 100 $\mu$m and 200 $\mu$m. For the two cases the magnetization is considered to be $\mu_0 M_R = 1.2$ T.

The fields, field gradients and forces presented below are calculated above the central part of a set of stripe-like magnets as schematically shown in Figure 4.4. The calculations are performed at the centre section of the magnets, sufficiently far from the edges, in order to avoid any edges effects. A more detailed discussion on edge effects can be found in [87].
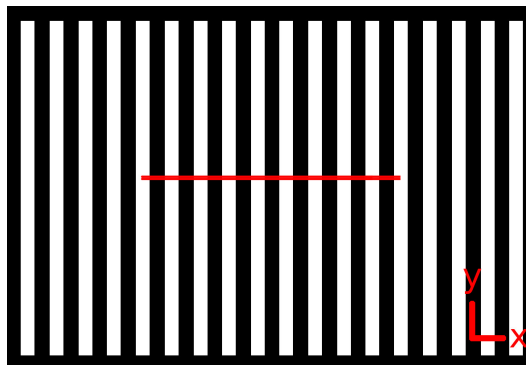


Figure 4.4: Schematic of the zone above which the fields, field gradients and forces are calculated. For TMP magnets the black and white zones correspond to up and down magnet orientations. In the case of TOPO magnets, these zones correspond to the magnets on the upper and lower layer.

### 4.3.1   Fields and field gradients

The first significant parameter to compare the different types of magnets is the magnetic field (or the induction) they generate at different distances. This field will dictate how the magnetic particles will be magnetized, as observed in Section 4.2. The particles used here present high susceptibility and are nearly saturated in the presence of low fields. However, a magnetic configuration optimized for the obtention of high field at long distances is

desirable. The second parameter is the variation of the magnetic field along an horizontal line perpendicular to the magnetic stripes. This gradient gives an idea of how the particle will be attracted horizontally towards the magnets. Finally, the vertical variation of the field is studied in order to estimate the downwards magnetic force.

Note that the induction $B$ and the induction gradients $\partial B/\partial x$ and $\partial B/\partial z$ are used here, for the sake of simplicity. It allows the use of the Tesla and the Tesla per meter as units for comparison, which are much straightforward than the $A/m$ and the $A/m^2$.

In Figure 4.5 the induction $B$ and the gradients $\partial B/\partial x$ and $\partial B/\partial z$ are shown. The columns correspond, from left to right, to 1.3 $\mu$m-thick TMP magnets, 10 $\mu$m-thick TOPO magnets and 30 $\mu$m-thick TOPO magnets. The colors correspond to the different widths of the magnetic stripes: red for 50 $\mu$m, green for 100 $\mu$m and blue for 200 $\mu$m. In every configuration, one of the interfaces of the micromagnets is positioned at x = 0 $\mu$m.

It is important to notice that the curves in red present peaks every 50 $\mu$m, while those in green present the peaks every 100 $\mu$m. These are sometimes masked by the superposed curves, especially in this first case, very close to the micromagnets, where the fields and gradients are similar.

At close distances, varying the feature size does not significantly affect the maximum values of fields and field gradients. This is explained by the small influence of the magnetic field created by one magnetic interface on the vicinities of another interface at such close distance to the magnet. However, TOPO magnets present a clear advantage as regards the field which can be generated at this distance. For the thicker TOPO magnets the field can reach around twice the values obtained with TMP magnets, since it is related to both the lateral dimension and the thickness of the magnet.
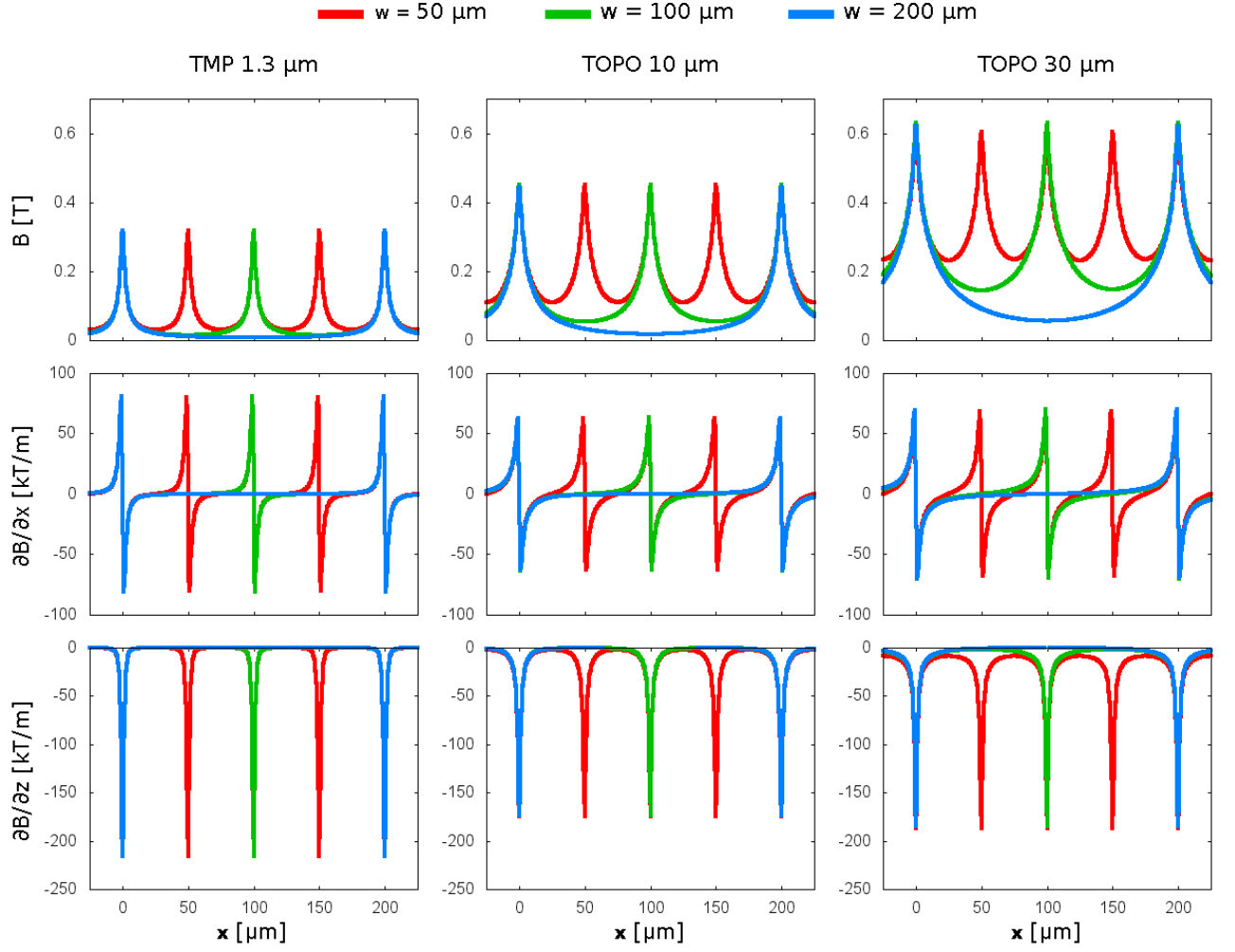
Figure 4.5: Plots of magnetic fields and gradients at a distance of 1 $\mu$m above the magnets.

An advantage can be observed when dealing with 50 $\mu$m-wide stripes, since the field does not decrease as low as in the case of wider features between the interfaces of the magnets. In the cases where a high field is desirable everywhere, narrower features are more adapted.

The field gradients 1 $\mu$m above TOPO magnets, on the other hand, are not significantly increased with the increase of magnet thickness. TMP magnets are best suited in this case, since both the gradients are more intense in every configuration. Given that the particles saturate at very low fields – which are obtained with all three types of magnets – TMP magnets are more adapted for particle attraction at the vicinities of the magnets.
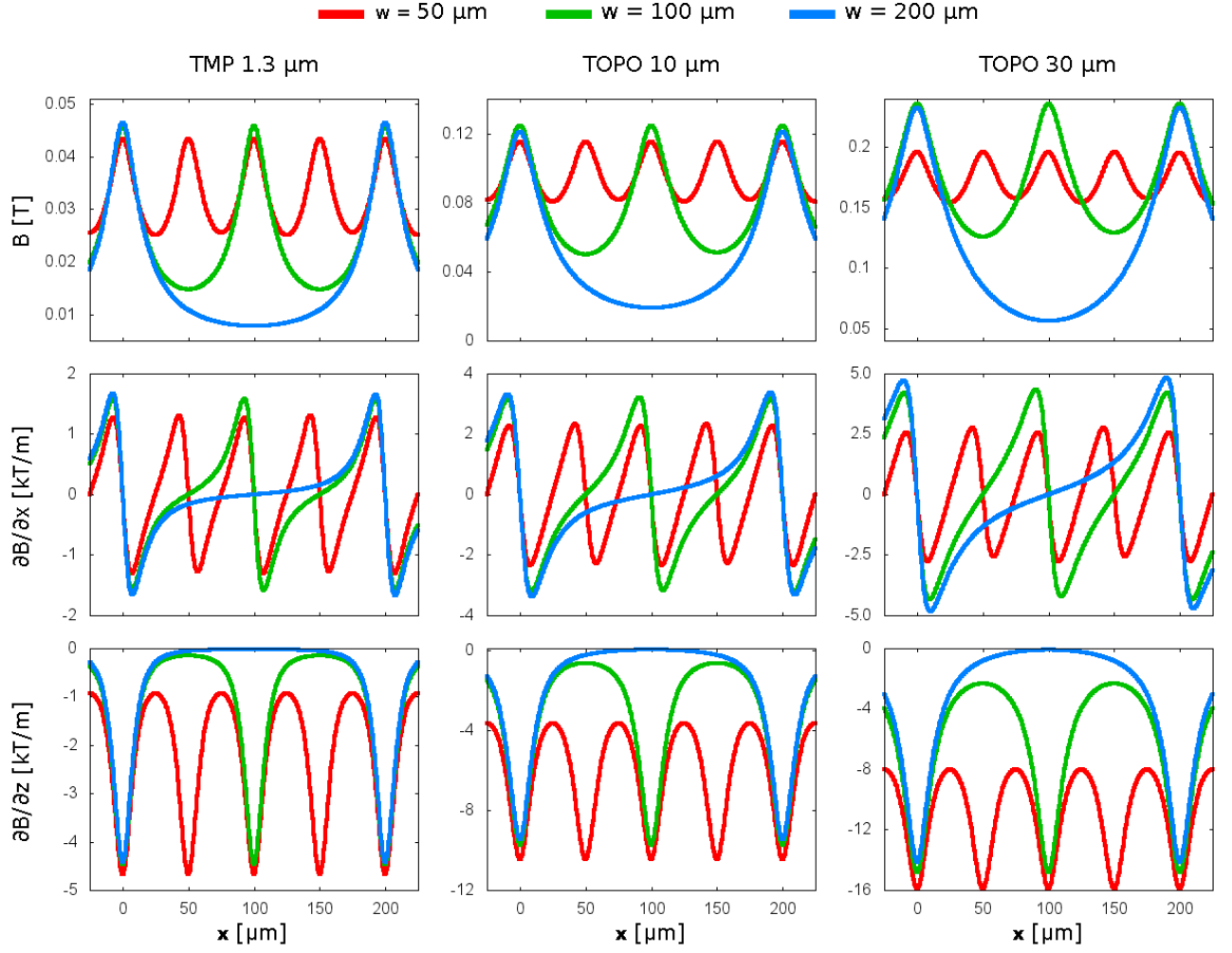
Figure 4.6: Plots of magnetic fields and gradients at a distance of 10 $\mu$m above the magnets.

At a distance of 10 $\mu$m from the magnets (Fig. 4.6) the thicker TOPO magnets seem to be more adapted for particle attraction. The values of magnetic field are significantly higher than those observed with the other magnets (around 5 times higher than for the TMP magnets, for instance). The use of narrower features in this case avoids the significant differences in the values obtained in the peaks and valleys of the curve. The 50 $\mu$m-wide features maintain the field around the highest values both above the edges and the center of the micro-magnets. The larger features, on the other hand, induce peak-to-valley differences 2 to 5 times higher.

As regards the field gradients along the x-axis, the homogeneity is again an advantage of the narrow features, though its maximum values are lower than the observed on other features. In the case of the gradients along the z-axis the advantage of the 50 $\mu$m-wide features is clear. The gradients are not only more homogeneous, but also more intense than in the other cases. Thicker TOPO magnets present higher field and field gradients and are, therefore, more adapted for particle attraction at long distance.
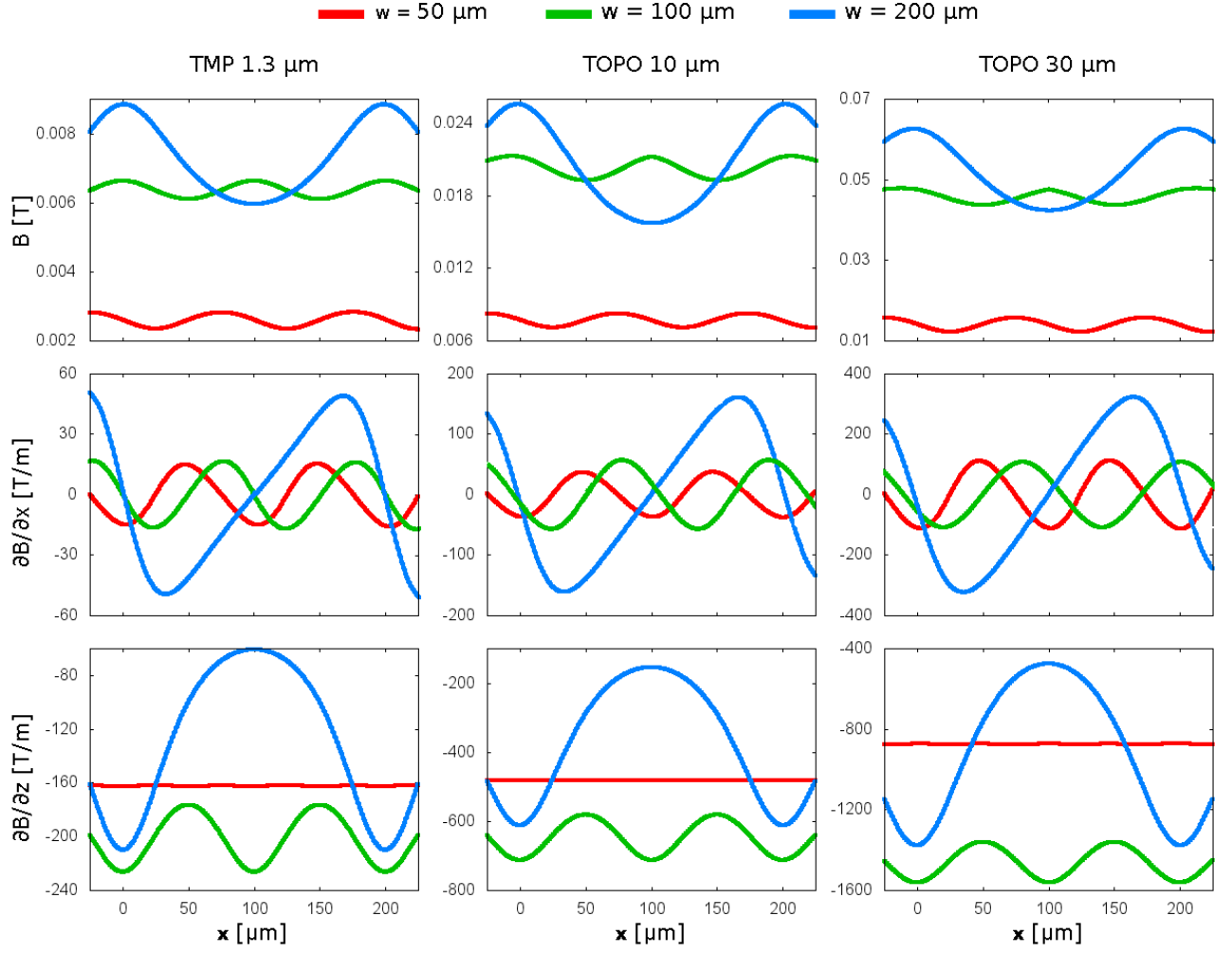
Figure 4.7: Plots of magnetic fields and gradients at a distance of 50 $\mu$m above the magnets.

Finally, when observing the magnetic fields at a considerable distance from the magnets (50 $\mu$m, Fig. 4.7), the narrow features lose their interest. The values of field are much lower than the observed for 100 and 200 $\mu$m-wide stripes, the latter presenting higher fields above the magnet interfaces, but lower on the center of the stripes. The observations of the fields gradients result in a split conclusion: even though much higher gradients can be obtained with the wider stripes along the x-axis, the gradients along the z-axis can be significantly lower than those created by 100 $\mu$m stripes. These stripes generate a $\partial B/\partial x$ very similar to those created by 50 $\mu$m stripes, but the $\partial B/\partial z$ is much higher.

As a conclusion, one can observed that at a zone very close to the magnets (comparable to the typical particle sizes) the fields are similar for every magnet type, but the gradients are favored with the use of TMP magnets. On the other hand, if attraction is needed at higher distances, the TOPO magnets are more adapted, due to their much higher field and fairly higher field gradients in this situation.

The choice of feature width is straightforward: the closer the particle will be to the

magnets, the smaller the features can be. A combination of big and small features would be the ideal configuration for the attraction of distant magnetic particles and strong pinning.

## 4.4 Microfluidics

Once the magnetic fields, gradients, particles responses and, thus, the forces acting on the particle are known, microfluidic systems can be designed and combined with micromagnets. In this section, the circulation of magnetic/non-magnetic particles inside a microfluidic channel is analyzed. The flow of a liquid in the channel and its influence on the movement of a particle are described. The equations are then associated to those concerning gravity and particle-magnet interactions so as to simulate the ensemble of forces acting on the particles and their induced displacements. Note that, since the calculations indicate a Reynolds number lower than 1 for all the systems used in this thesis, the related aspects of fluid flow are considered.

Dynamic simulations of particle trajectory are performed in order to better understand the influences of isolated parameters of the system on particle attraction. The conditions for particle capture are then established and the requirements for the design of an optimized device determined. A more complex system based on continuous flow sorting is discussed and simulated, prior to its fabrication and testing, shown in Chapter 5.

### 4.4.1 Particle flow in a microfluidic channel

A particle of radius $r_{part}$ and mass density $\rho_{part}$ in a medium of density $\rho_{med}$ is constantly submitted to two forces, gravity and buoyancy, which can be expressed, respectively, as

$$F_g = \frac{4}{3} \pi \, r_{part}^3 \, \rho_{part} \, g \tag{4.12}$$

and

$$F_b = \frac{4}{3} \pi \, r_{part}^3 \, \rho_{med} \, g \tag{4.13}$$

Particles are also submitted to a Brownian motion caused by the thermal energy of the system. This motion depends on the temperature of the medium, its viscosity $\eta$, and the radius of the particle and is generally expressed by a diffusivity coefficient, $D$. This coefficient is calculated by

$$D = \frac{k_B \, T}{6 \, \pi \, \eta \, r} \tag{4.14}$$

$k_B$ being Boltzmann's constant. The influence of Brownian motion is usually negligible in the cases where $r_{part} > 40$ nm [11]. In the present work the minimum particle size is 200

nm, thus, the term related to this motion is not considered any further.

Figure 4.8 schematically shows a microfluidic channel produced above a set of micromagnets. Notice that the $(x, y, z)$ axes positions are used in the further discussions and simulations. The microfluidic channel and, thus, the direction of fluid flow are aligned to the y-axis, a positive displacement meaning that the fluid or particle is moving towards the increasing positive y values.
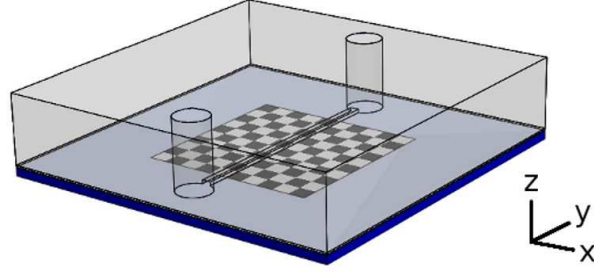


Figure 4.8: Schematic of the microfluidic system and selection of axes of reference.

A micro-channel with rectangular section is used in all the situations discussed here. The fluid velocity along the y-axis at a point $(x, z)$ inside the channel is calculated by Poiseuille's equation, reproduced in Eq. 4.15. Here, the height and width of the channel are represented by $h$ and $w$, respectively, while $L$ represents its length.

$$v_y(x, z) = \frac{4h^2 \Delta p}{\pi^3 \eta L} \sum_{n,odd}^{\infty} \frac{1}{n^3} \left[ 1 - \frac{cosh\left(n\pi \frac{x}{h}\right)}{cosh\left(n\pi \frac{w}{2h}\right)} \right] sin\left(n\pi \frac{z}{h}\right) \qquad (4.15)$$

The difference in pressure between the extremities of the channel, which is the reason for the fluid flow in this case, is represented by $\Delta p$. The normalized fluid velocity profile plotted for a cross-section along the $(x, z)$ plane of a given channel is shown in Figure 4.9.
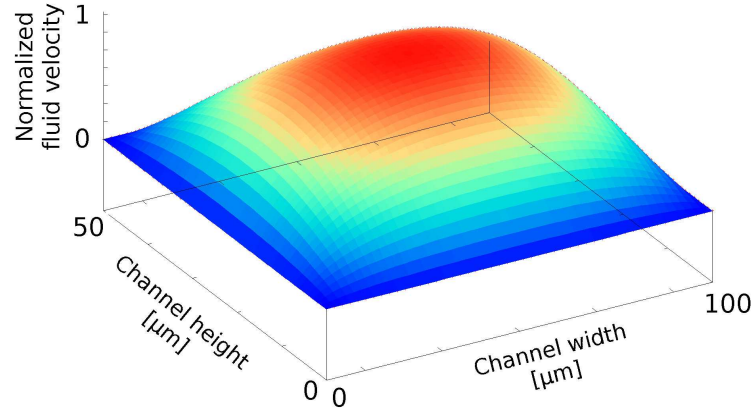
Figure 4.9: Normalized fluid velocity profile (the so-called Poiseuille profile) for a given channel of rectangular section. The velocity decreases from its maximum at the center of the channel to its minimum (zero) at the edges.

The velocity reaches its maximum at a point in the center of the channel and its minimum at all the edges, where it is null. This profile is considered to be constant for every position from the inlet to the outlet of the channel. The perturbations caused by the deviations of fluid and variations in the section area of the channel are not taken into account in this case, since the particle-magnet interactions are simulated in the areas where the microfluidic channel is straight.

A particle flowing in the channel is submitted to a drag force, $F_d$, which is calculated as shown in Eq. 4.16. In this case, the initial velocity of the particle is given by $v_{part}$ and $v_y(x, z)$ is calculated at its center, i.e., the particle is considered to be punctual.

$$F_d = 6\,\pi\,\eta\,r_{part}\,(v_y(x, z) - v_{part}) \tag{4.16}$$

This equation for the force, also known as Stoke's drag, comes from the resolution of the Navier-Stokes' equation (Eq. 1.7) for small Reynolds numbers. The balance of all forces acting on a particle is thus given by the equation of dynamics

$$\frac{4}{3}\pi\,r_{part}^3\,\rho_{part}\,\frac{dv_{part}}{dt} = F_d + F_g + F_m \tag{4.17}$$

For the cases considered here, the inertia of the particles can be neglected due to the time scale of inertial events compared to other movements of the particles. Note that the magnetic buoyancy force is also neglected, since it is around 5 orders of magnitude lower than the attractive magnetic forces in the system. Also, experimental results indicate that friction and chemical interactions can be neglected. Thus, the particles can be considered to move at their limiting velocity given by

$$v_x \quad = \quad \frac{F_{mx}}{6\,\pi\,\eta\,r_{part}} \tag{4.18}$$

$$v_y \quad = \quad v_{fluid} + \frac{F_{my}}{6\,\pi\,\eta\,r_{part}} \tag{4.19}$$

$$v_z \quad = \quad \frac{F_g + F_{mz}}{6\,\pi\,\eta\,r_{part}} \tag{4.20}$$

where $F_{mx}$, $F_{my}$, and $F_{mz}$ are the components of the magnetic force along the x, y, and z-axis, respectively. The displacement of the particles is thus derived using $\partial x/\partial t = v_x(t)$, $\partial y/\partial t = v_y(t)$, and $\partial z/\partial t = v_z(t)$.

### 4.4.2 Particle attraction and capturing

In order to perform particle capturing two conditions must be fulfilled:

- The particles entering the microfluidic channel have to be attracted towards the magnets quickly enough, i.e., they must reach the bottom of the channel before reaching the outlet;

- There must be a pinning magnetic force (when the particle reaches the bottom of the channel) equal in modulus but opposing in direction the drag force created by the fluid flow.

In the static case a particle would be captured right above the interface of oppositely magnetized zones. Considering that the fluid pushes the particle away from this interface, the position of equilibrium will no longer be the one where the magnetic force is vertical. In this case, the particle will be slightly dragged to a position where a magnetic force is created with a certain angle to the vertical axis. The new equilibrium position is the one where the component of the magnetic force along the y-axis is equal in modulus to the drag force ($|F_d| = |F_{my}|$).
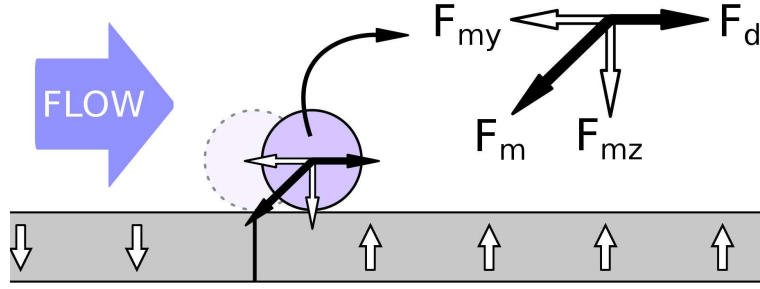
Figure 4.10: Equilibrium position for a particle captured inside a microfluidic channel. The particle is pushed by the drag force until the position where $|F_d| = |F_{my}|$. The dashed particle is in the equilibrium position above the up/down magnetic interface in the case where no fluid flow is present.

The two conditions listed above often have to be optimized separately, as regards the magnetic configuration, as discussed in section 4.3. In order to attract particles which are far away from the magnetic film to the bottom of the channel, big magnetic patterns have to be used. However, high pinning forces are obtained close to the interfaces of differently oriented magnets. Particle trapping is, thus, optimized by the maximization of the number of magnet interfaces, i.e., the reduction of the micromagnet's dimensions.

Other parameters can, obviously, be modified to improve particle capturing. These are listed below:

- Flow rate: the one parameter which can be easily modified during the experiments, after the whole system is finished. A lower flow rate improves particle capturing, since the particles are submitted to the magnetic field for a longer time and the pinning force required to maintain the particle trapped is lowered;

- PDMS cover layer thickness: an increase in this thickness will lower the maximum magnetic force which can be reached once the particle is in the bottom of the channel, thus reducing the performance of particle capturing;

- Micro-channel dimensions: keeping the flow rate constant, a reduction in the channel dimensions yields an increase in the velocity of the liquid and, consequently, in the drag force. Larger channels, on the other hand, favor the pinning force/drag force equilibrium, but increase the average distance between the particles and the magnets, thus increasing the time required for capture;

- Magnetic content and properties of the particles: considering the radius of a particle is maintained constant, an increase in its magnetic content will increase its global density ($F_g$ increases) and, obviously, increase the magnetic force to which the particle will be submitted. The more magnetic material a particle contains, the easier (faster and/or stronger) it will be attracted towards the magnets. The magnetic properties of the iron oxide nanoinclusions can also play a significant role: the magnetic force can be favored by an increase in the saturation magnetization and/or in the magnetic susceptibility.

It can be observed that a whole set of dimensions, properties and parameters of process have to be considered in order to optimize particle capturing. Evidently, more complex arrangements can be designed, such as the use of wide magnetic patterns close to the inlet of the channel, favoring the downward motion of the particles, followed by a set of smaller patterns which increase the density of pinning sites. In the next chapter the considerations developed here are taken into account in order to design a device for particle capturing.

### 4.4.3    Particle deviation

It has been shown in section 1.3 that deviating particles continuously can be of great interesting for several applications. In the section above particle capturing has been presented, with a pinning force opposing a drag force. However, these two forces can be combined in order to perform particle guiding along specifically designed magnetic rails.

Consider the two oppositely oriented magnets shown in Figure 4.11a (top-view). A magnetic particle put in their vicinities will be submitted to a magnetic force as indicated by the arrows. Once the particle reaches the interface between the magnets, it stops at an equilibrium position (Fig. 4.11b). Now consider the medium in which the particle is immersed moves, creating a drag force on the particle, as indicated by $F_d$ in Fig. 4.11c. This force can be decomposed in two:

- A component which is perpendicular to the magnetic interface. If this force overcomes the maximum magnetic force acting on the particle on the opposite direction, the particle is unpinned. Otherwise, the equilibrium position is slightly moved away from the magnets interface, somewhere between the initial equilibrium position and the position of maximum magnetic force, as previously shown in Fig. 4.10.

- A component which is parallel to the magnetic interface. Since no force opposes this component (neglecting particle/PDMS friction or adherence), the particle can move, pushed by the drag force and guided by the magnetic rails.
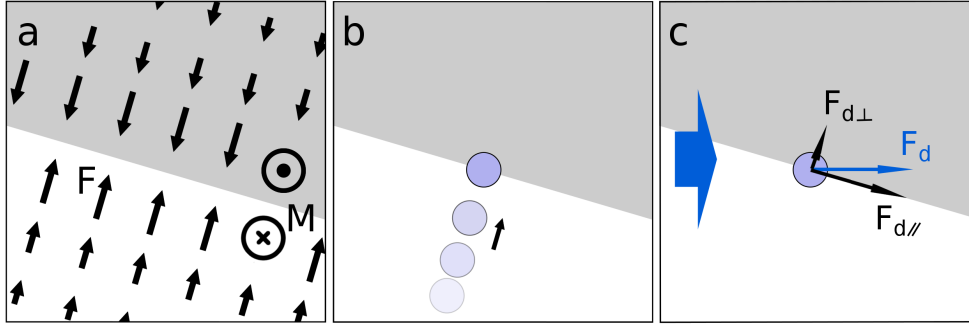
Figure 4.11: Schematic representation of a system with up and down magnets, shown in gray and white. (a) The direction of the magnetic force which acts on an object on the vicinities of the interface between the magnets. (b) A particle initially positioned above one of the magnets is attracted towards the interface, the equilibrium position. (c) A fluid flow (big blue arrow) induces a drag force $F_d$ (small blue arrow), which can be decomposed in parallel and perpendicular components, as regards the magnetic interface.

A few parameters can be adjusted in order to modify the way particles interact with the magnetic rails. The system can be designed so as to optimize the attraction towards a single line, i.e., passing from a 3D dispersion of particles to a 1D disposition with particles flowing one after the other. Observation of a succession of objects or controlled reactions with well-defined times can be performed with this arrangement.

Notice that not only guiding can be useful. If a particle is successively submitted to the force created by the rails, being just deviated by each one of them towards a certain direction without following a single rail until its end, it can be separated from other magnetic or non-magnetic objects. Figure 4.12 exemplifies how different the trajectories of a particle can be according to certain parameters. The trajectory gradually changes from the case 4 towards the case 1, i.e., the particle is more easily deviated, when one or more of the following occur:

- The magnetic content of the particle is increased;

- The PDMS layer thickness is decreased;

- The flow rate is decreased;

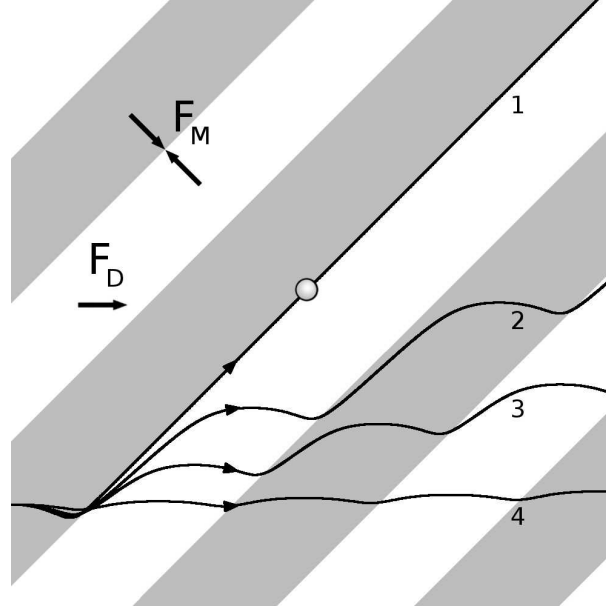- The angle between the rails and the direction of flow is decreased.

Figure 4.12: The particle trajectory is highly influenced by the factors mentioned in the previous list. Easier deviation (from the case 4 gradually to the case 1) can be achieved controlling these parameters. The resulting trajectory is a combination of the drag force and the magnetic force, as indicated.

From the first item of the previous list it is obvious that if two particles with different magnetic content flow through the same channel with the same conditions, they will be differently deviated. This principle can be used to sort magnetic from non-magnetic objects or, yet, to sort multiple types of magnetically labelled objects. In the next chapter, an experimental example of continuous sorting based on these simulations will be presented.

## 4.5   Partial conclusion

A complete model of the coupled fluidic/magnetic micro-device has been developed in this chapter. Particle attraction is predicted to occur, in the static case, on the interfaces between up and down (or differently oriented) magnets, where the magnetic field gradient is the highest. Furthermore, the influences of each parameter have been analyzed in the dynamic case. The basic requirements for best particle capturing conditions have been listed. Flow rate is found to play one of the main roles on the success of particle capturing. A slight decrease in the flow rate can allow a significant increase in the capturing rate, due to its influence in the equilibrium position of the particles above the magnet arrays.

Other main roles are played by the PDMS layer thickness – a small reduction in the thickness leading to a major increase in the maximum magnetic force acting on the particles – and the dimensions of the magnets. Final pattern characteristics will be a trade-off between long range capture and pinning conditions. Pattern design needs a case-by-case analysis of the system in order to be optimized, since large lateral dimensions favor attraction of

particles at a long distance, while small lateral dimensions favor the density of pinning sites.

In the case of continuous particle sorting all the previously mentioned conditions are valid. However, the most practical parameter for sorting optimization is found to be the flow rate, as it can be adapted in real-time according to the objects present in the system.

The possibility of particle capturing and sorting is shown theoretically and a set of hints for the design of actual devices are given so as to boost their performance. In the next Chapter the model presented here is used for well-determined conditions and compared to experimental results.

# Chapter 5

# Bio-Mag-MEMS

In Chapter 4 the micromagnetic and microfluidic systems were modeled based on the specificities defined in Chapters 2 and 3. In this Chapter actual systems are used in test applications in order to characterize their usability for real lab-on-chip and point-of-care devices.

The first observations of magnetic attraction are performed using spherical magnetic microparticles. These particles are chosen due to their similarities to most of the commonly studied biological entities:

- The density of the particles' polymeric matrix is close to the density of the aqueous medium used in the experiments, usually around 1;

- The magnetic inclusions are homogeneously dispersed in the matrix and the amount of magnetic material in the particles can be selected according to the supplier.

Additionally, no significant adherence is observed between the particles and PDMS, which is important to insure that no extra interactions (specially those which are hardly measurable) are present. In this case, adherence of cells to a substrate, for instance, can be studied by observing the difference in the balance of forces acting on these objects, as compared to magnetic particles. Further research on this topic is being developed at the moment.

Particle-magnet interactions are analyzed, at first, statically, using magnetic patterns of different types (magnetization in-plane or out-of-plane, geometrical or complex shapes). A set of magnetic particles ranging in diameter from 200 nm to 10.4 $\mu$m is used in order to analyze their spatial distribution on the magnets. The cooperation with the Ampère Laboratory allowed, in parallel, the study of static positioning of magnetically labelled liposomes, cells and bacteria. Endocytosis processes were also studied.

Dynamic capture and positioning is experimentally studied using the polymer-based microfluidic channels built above the micromagnets. Different magnetic particles are used to compare the simulations of in-flow capture. Sorting of magnetic and non-magnetic particles is, then, performed by two methods:

- trapping of magnetic particles;

- continuous sorting.

Both methods successfully sort initially mixed solutions with high efficiency.

More complex systems which are now being developed are presented, followed by a discussion of their potential applications.

## 5.1 Static capture

Preliminary tests of capture are performed using magnetic microspheres. The goal is to observe qualitatively how magnetic attraction and capture occur, then, if unpinning captured particles is possible. Particles consisting of a polymeric matrix with embedded magnetic nanoinclusions (see Figure 1.4) are chosen for their similarities in shape, density and dimensions with the biological elements of interest. They serve as a fair model, for instance, for a cell labeled with a certain amount of magnetic nanoparticles. Also in the biological and medical applications, the capture of functionalized particles itself is of foremost importance.

A flat magnetic film is used, part of it patterned by TMP, thus presenting magnetic field and gradients. The rest left in the saturated state (magnetization out of the film plane), equivalent to a non-magnetized layer: no fields or gradients are provided. Water containing $\varnothing$ 3 $\mu$m magnetic particles in low concentration is poured on the film and the solution is left to settle for a few minutes. Figure 5.1a shows the resulting distribution of magnetic particles. The particles which sediment above the non-patterned zone – the right side of the film – are randomly distributed. On the left side the magnetic squares produced by TMP are outlined by the particles. This simple experiment confirms the predictions that the strongest capture occurs on the interfaces of up/down magnets, where fields and gradients are most intense.
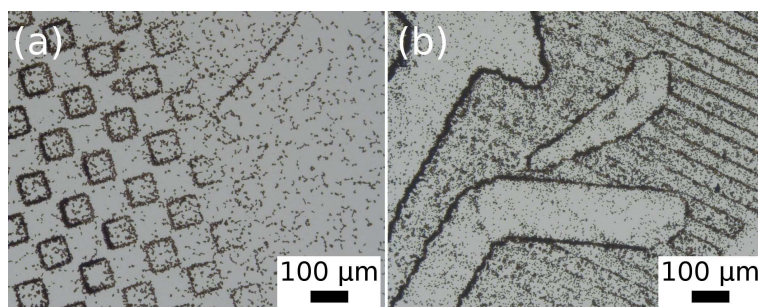


Figure 5.1: (a) SPM particles above a magnetic film. The particles are randomly distributed on the right side of the film, which is in the magnetically saturated state, while they outline the TMP pattern on the left side. (b) A more complex pattern produced by TMP and outlined by the SPM particles. Zones of low magnetic force are also created in between the patterns, as proven by the random distribution of particles.

One can also observe that some particles are randomly positioned inside the squares or between them. This positioning away from the interfaces of TMP patterns can be caused by two factors: the particles are not submitted to a strong enough magnetic force while settling

and are not sufficiently deviated towards the interfaces; the particles are trapped by a local magnetic gradient. In this last case, the local gradient is generally caused by an irregularity of the magnetic film: a variation in chemical composition, an oxidation spot, a non-magnetic or less-magnetic inter-granular phase, etc.

The same phenomenon is observed in Figure 5.1b which shows the SPM particles distributed above an array of magnetic stripes superposed with part of a more complex pattern. The larger amount of particles in this case make even more clear the attraction to zones away from magnetic interfaces. The edges of the complex pattern generate a stronger magnetic force as compared to the stripes, as proven by the larger amount of particles attracted on their edges. This is caused by the higher fluence used to produced the complex patterns, which generates deeper patterns and, thus, stronger magnetic forces. Moreover, a higher edge effect occurs in such configurations.

It is also observed in these preliminary studies that the amount of particles on the patterns can be controlled by a fluid flow. Figure 5.2a shows the distribution of particles above an array of squares. A thick outline of the square is produced by the particles which are captured by edges of the features. Once a fluid flow is induced by agitation with a pipette, the particles which are less strongly attracted to the magnets are removed with the drag force. Figure 5.2b shows the particles remaining on the magnets after the system is submitted to agitation. Only the strongly trapped particles are still present on the magnets.
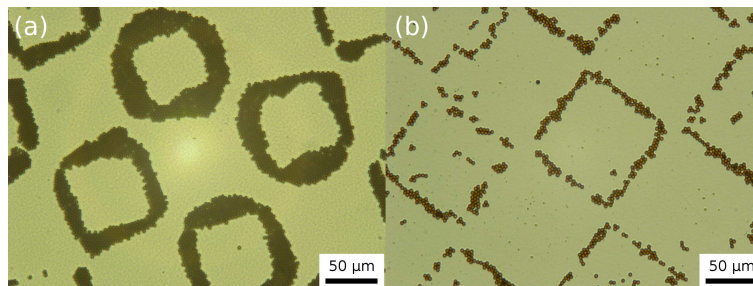


Figure 5.2: (a) A large amount of SPM particles is captured above an array of magnetic squares. (b) Most of the particles are removed by the drag force once a strong fluid flow is induced.

The control of particle capture by fluid flow is already a hint for the possible use of these micromagnets in microfluidic applications.

### 5.1.1 Static positioning

Based on the previous results on attraction a more controlled positioning of particles is performed. Triode sputtering is used to produce 5 $\mu$m thick high performance hard magnetic films (NdFeB and SmCo). The NdFeB films are out-of-plane (oop) textured ($\mu_0 H_C = 2.0$ T, $B_R = 1.2$ T), while the SmCo films are in-plane (ip) textured ($\mu_0 H_C = 1.3$ T, $B_R = 0.8$

T). These hard magnetic films are magnetically structured using the TMP method. Stripes, chessboards and grid-like magnetic patterns with lateral dimensions ranging from 100 down to 7 $\mu$m are prepared.

Uniaxial and planar MOIFs (U-MOIF and P-MOIF, respectively) are used to characterize the stray magnetic field produced above the hard magnetic micropatterns. Stripe and chessboard patterns magnetized out-of-plane (oop) produced in NdFeB films are revealed by magneto-optical (MO) imaging of an overlying U-MOIF (Figs. 5.3a and 5.3b). These binary images (dark/light contrast) confirm that the direction of magnetization is reversed during the TMP process. A MO image of a P-MOIF overlaid on an in-plane (ip) magnetized SmCo film patterned with a chessboard mask is shown in Fig. 5.3c. The image is coded in 256 colors and the zones of intense dark/light contrast which appear at the edges of the squares, are perpendicular to the axis of magnetization, where the oop component of the stray magnetic field is highest. Much smaller oop magnetized patterns produced in a NdFeB film using a grid with holes of size 7×7 $\mu$m$^2$, spaced by 5 $\mu$m, revealed using a U-MOIF, are shown in Fig. 5.3d. The magnetic patterns appear rounded due to the limited spatial resolution of the imaging technique, as well as the MOIF-magnet distance.
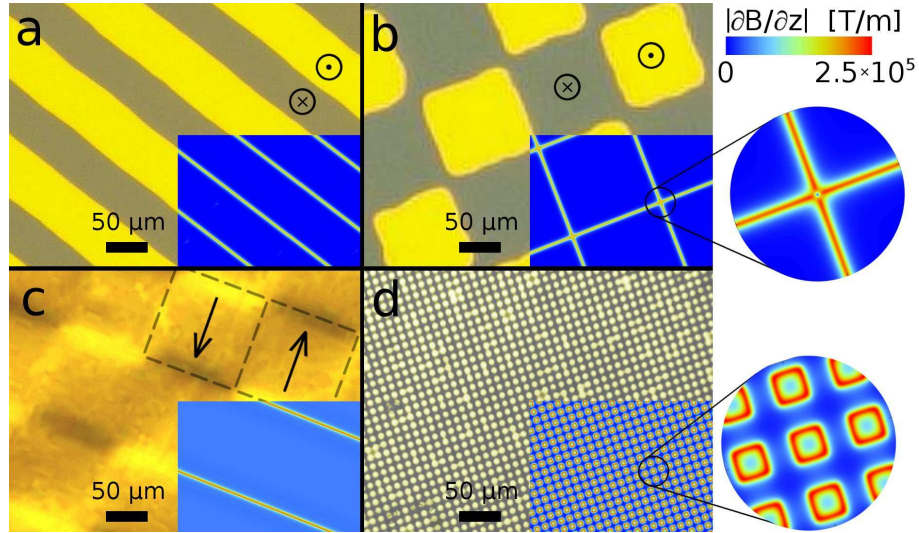


Figure 5.3: U-MOIF images of (a) stripe and (b) chessboard oop patterns in NdFeB; (c) P-MOIF image of an ip chessboard pattern in SmCo; (d) NdFeB film patterned oop with a mask that consists of square array (7×7 $\mu$m$^2$) motifs. The insets represent the modulus of the magnetic field gradient $\partial B/\partial z$. [88]

The spatial distribution of the magnetic field and the magnetic field gradients of idealized structures (assuming the thermomagnetically reversed sections to be parallelepipeds of depth 1.3 $\mu$m) are calculated analytically. The modulus of the magnetic field gradient along the z-axis ($\partial B/\partial z$) calculated 1 $\mu$m above the patterned films are shown in the insets of Fig. 5.3 (this distance corresponds to the estimated gap between the magnetic film and the active layer of the MOIF). The most intense gradients are found on the edges of the magnetic patterns.

Commercial superparamagnetic fluorescent nano/microparticles (Chemicell GmbH: ⌀ 200 nm; Micro Particles GmbH: ⌀ 1.4 and ⌀ 4.9 $\mu$m) and non-fluorescent microparticles (Micro Particles GmbH: ⌀ 10.3 $\mu$m), which are dispersed in an aqueous solution, are imaged using scanning electron microscopy (SEM) and shown in Figure 5.4. The smallest particles, of nominal size 200 nm (Fig. 5.4a), are in fact agglomerates of particles of much smaller size ($\sim$ 10 nm). The coarser particles (1.4, 4.9, and 10.3 $\mu$m, Figs. 5.4b, 5.4c and 5.4d, respectively) consist of superparamagnetic iron-oxide nanoparticles dispersed in a polystyrene matrix. They are spherical in shape and show a narrow size distribution.
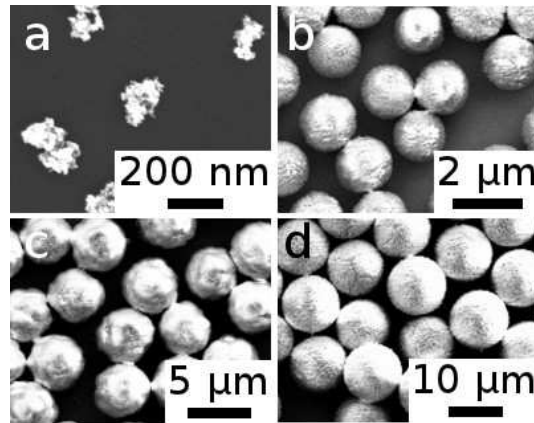


Figure 5.4: SEM images of the superparamagnetic particles: (a) nominal diameter 200 nm; (b) ⌀ 1.4 $\mu$m; (c) ⌀ 4.9 $\mu$m; and (d) ⌀ 10.3 $\mu$m.

Small volumes of water-diluted microparticle solutions are dropped onto micromagnet arrays and their positioning onto precise patterns is imaged using conventional and fluorescence optical microscopy. Such particles show a very high suceptibility in low fields ($\mu_0 H$) (up to a few hundreds of mT) followed by saturation in higher fields. The force is thus calculated using $M(H)$, as fitted to the experimental magnetization curves of each type of particle. As a result, when an aqueous solution containing superparamagnetic particles is dropped onto a micromagnet array, the particles are magnetically attracted to the regions of highest field gradient, i.e., to all the interfaces between oop magnetized structures. For in-plane structures attraction occurs at the interfaces perpendicular to the direction of magnetization (Fig. 5.5).

The attractive force acting, for instance, on a ⌀ 1.4 $\mu$m bead, in which the superparamagnetic inclusions account for 30% of its mass, in direct contact with the film is estimated as $\sim$13.6 nN. Note that the liquid solution is maintained in place by positioning the micromagnet array in a small container and deionized water is flushed through the solution to displace particles that are not trapped strongly enough by the micromagnets.
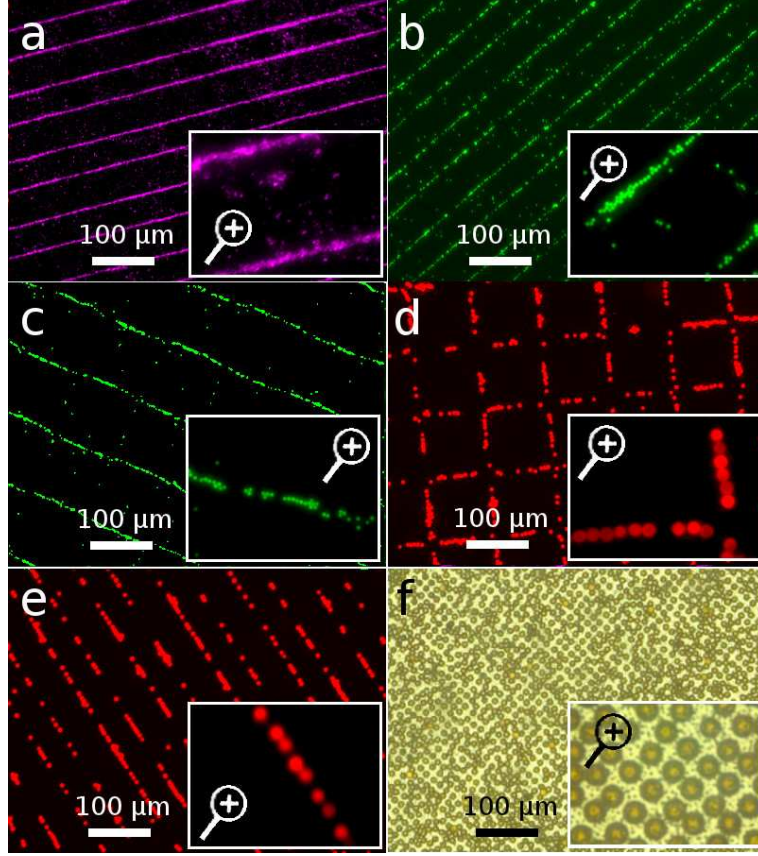
Figure 5.5: Fluorescence images of the superparamagnetic particles trapped by micromagnets [(a): 200 nm above oop magnetized NdFeB; (b): 1.4 $\mu$m above oop magnetized NdFeB; (c): 1.4 $\mu$m above ip magnetized SmCo; (d), (e): 4.9 $\mu$m above oop magnetized NdFeB]; (f) 10.3 $\mu$m particles individually positioned in a square lattice above an oop magnetized NdFeB film (the reversed magnets are $7 \times 7$ $\mu$m$^2$ in surface area, separated by 5 $\mu$m). The insets present a zoom on the particles positioned above each magnetic configuration.

In the case of the smaller particles (200 nm, 1.4 $\mu$m), capture occurs with several particles around the interface, without a precise alignement (Figs. 5.5a, 5.5b and 5.5c). It is also observed that some of these particles may be pinned at sites away from the micromagnet interfaces. As stated above, this can be explained by local variations of the magnetic field gradient caused by inhomogeneities in the magnetic film. The very localized nature of these variations explains the fact that only the smaller particles are trapped at these zones. The particles of size 4.9 $\mu$m form relatively straight chains (Figs. 5.5d and 5.5e). In this case the lateral extent of the field gradient is insufficient to form chains more than one particle wide.

In Fig. 5.5f single particle positioning is shown. A mask with holes of size $7 \times 7$ $\mu$m$^2$, separated by 5 $\mu$m is used to produced a very small, isolated TMP pattern on a oop NdFeB film. Superparamagnetic particles on the dimension range of the individual magnetic features ($\varnothing$ 10.3 $\mu$m) are used in this case. As only one particle can be captured by each magnetic feature, a periodic particle array is formed.

These simple experiments demonstrate the possibility to accurately position/align

superparamagnetic nano and microparticles using arrays of permanent micromagnets. The type of pattern achieved can be tailored by varying the size of the particles and the size/orientation of the micromagnets. These results can be, evidently, extended to the positioning of magnetically labeled elements, such as cells, bacteria or proteins.

## 5.1.2   Positioning of biological elements

In order to demonstrate the interest of such structures for biological applications, the TMP magnets are used to trap cells which have internalized superparamagnetic nanoparticles via endocytosis[1]. Endocytosis is an essential biological process by which cells internalize macromolecules and particles into transport vesicles invaginated from the plasma membrane. In non phagocytic cells (such as the cells used here), the uptake of particles is driven by an endocytic mechanism called pinocytosis, or fluid-phase uptake, which itself encompasses different pathways, depending on cell and particle type.

Human embryonic kidney cells (HEK293, ATCC No.  CRL-1573, $\varnothing$ $\sim$10 $\mu$m) are magnetically functionalized with 100 nm superparamagnetic particles (Ademtech) by endocytosis. Note that the cell-to-particle diameter ratio is around 100, while the volume ratio is on the order of $10^6$. For instance, endocytosis of 1000 particles will only account for 1/1000 of the cell volume. This is an important information related to biocompatibility and impact on cell behavior. A systematic study remains to be done on the influence of the particle's surface properties, magnetic properties and quantity in the cell. It is not, however, the scope of this work. Preliminary experiments have shown that cell can be manipulated with particles without an apparent impact on their intrinsic characteristics. It is important to stress here that the use of *micro*magnets allows a significant increase in the magnetic force acting on the particles. The amount of particles in the cells can be considerably reduced for a succesful magnetic attraction.

Up to now, the average number of internalized particles per cell and, thus, the corresponding magnetic force acting on the cell are not precisely known. More extensive studies are needed to clarify the endocytotic pathway and to estimate the average number of particles taken up by such cells. The cells having taken up $\varnothing$ 100 nm particles are purified by centrifugation [washed twice in phosphate buffer solution (PBS)] and resuspended in PBS. A drop of solution is deposited on an oop magnetized NdFeB film ($50 \times 50$ $\mu$m$^2$ squares).

The cells are observed to align along the edges of the magnetic patterns (Fig 5.6a). Due to biological cellular adhesion, some cell clusters also formed. Similar experiments have been performed by Pivetal et al. using magnetically labelled liposomes[75] (Fig 5.6b) and bacteria (Fig 5.6c). In the case of bacteria, the magnetic particles adhere to their membrane, instead of being internalized by endocytosis.

---

[1]The experiments using biological elements were performed in the Ampère Laboratory by J. Pivétal and O. Osman, under the supervision of M. Frénéa-Robin, N. Haddour and P. Simonet.
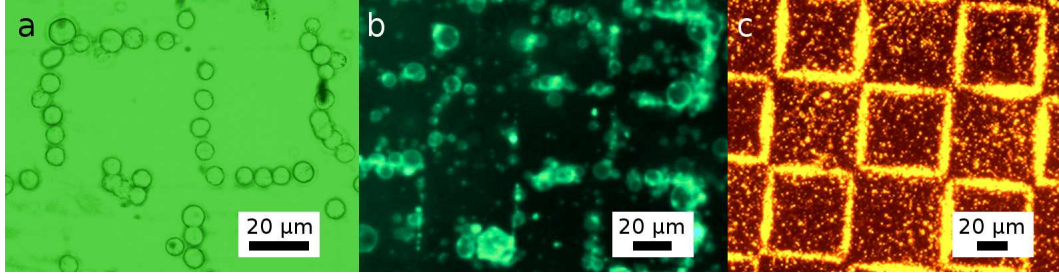
Figure 5.6: (a) HEK293 cells, (b) liposomes and (c) bacteria functionalized with magnetic nanoparticles trapped on chessboard-like magnetic patterns ($50 \times 50$ $\mu$m$^2$ squares). Results obtained by O. Osman and J. Pivetal, from Ampère Laboratory, Lyon.

The trapping and precise positioning of these biological entities, together with the possibility of making the micromagnet structures biocompatible by the deposition of an appropriate protective layer (polymer, oxide...) opens the possibility for a vast range of new biological applications. An example of such applications was reported by Osman et al. [76] and is discussed in the next section.

### 5.1.3   Study of endocytotic uptake by cell capturing

Osman et al. studied the endocytotic uptake of 100 nm magnetic nanoparticles by HEK293 cells. The influence of both the nanoparticle concentration in the extracellular medium and the incubation time is observed based on cellular distribution above TMP magnets [76].

The endocytosis process of nanoparticles is studied by the observation of cell distribution above the TMP magnets. HEK293 cells are incubated in a medium containing different concentrations of magnetic nanoparticles for 24h at 37 °C. Cell distribution is observed in Figure 5.7 for mixtures containing an equivalent ratio of 0 (5.7a), 325 (5.7b), 3000 (5.7c) and 7500 (5.7d) particles per cell. Note that this is the concentration of the incubation solution and not necessarily the amount of particles per cell. The actual number of particles in the cells may be significantly different from the average in the medium.
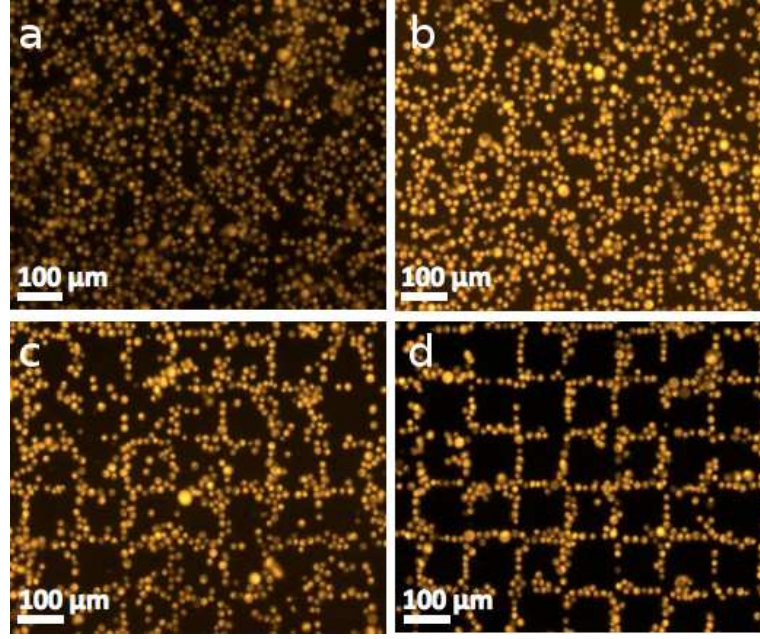
Figure 5.7: Distribution of cells above TMP magnets after incubation for 24 hours in a medium containing a ratio equivalent to (a) 0, (b) 325, (c) 3000 and (d) 7500 particles per cell. Results obtained by O. Osman, from Ampère Laboratory, Lyon.

As expected, cells containing no magnetic particles are randomly distributed above the magnets. However, as the concentration of particles in the incubation medium increases, the outlining of magnetic interfaces becomes more evident. For a concentration of 325 particles per cell an ordered distribution is hardly seen, while at 3000 particles per cell a clear attraction is observed. At 7500 particles per cell a virtually perfect attraction is achieved, with very few cells positioned away from the edges of the magnets. It indicates that the amount of nanoparticles internalized by the cells overcomes the critical amount for attraction and positioning.

The influence of incubation time is also studied, keeping fixed the ratio of 7500 particles per cell in the incubation medium. The distribution of cells is observed in Figure 5.8 after incubation during (a) 1, (b) 2, (c) 4 and (d) 6 hours. For incubation times shorter than 2 hours no clear alignment is observed, while above this threshold time, the outlining of squares becomes more evident. Above four hours of incubation, however, no further improvement of the cell positioning is observed, for all particles are already captured by the magnetic pattern.
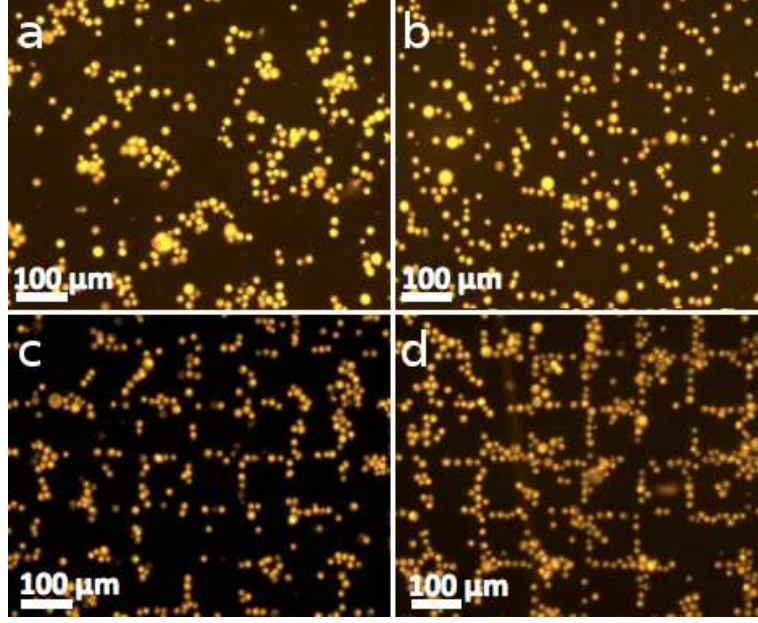
Figure 5.8: Distribution of cells above TMP magnets after incubation in a medium containing 7500 particles per cell for (a) 1, (b) 2, (c) 4 and (d) 6 hours. Results obtained by O. Osman, from Ampère Laboratory, Lyon.

The quantification of the amount of particles internalized by the cells is yet to be studied, but a clear applicability of the micromagnets on the biological field is proven. The method presented in the Osman's article [76] is a simple and fast way to monitor particle uptake by cells. It can be exploited to establish the threshold amount of particles required for magnetic trapping, thus reducing issues related to particle toxicity. Actual applications include, for instance, medical diagnosis based on the difference in particle uptake between healthy and malignant cells.

## 5.2   Capture with microfluidics

The capture of magnetic particles is also studied in a dynamic fashion, i.e., using a micro-fluidic channel above the magnetic film. Preliminary tests were performed using ∅ 1 $\mu$m magnetic particles and a magnetic film in which chessboard-like patterns were produced. These tests showed that the attraction occurs as predicted by the simulations performed in Chapter 4. As the particles start to flow inside the channel the first magnetic squares are revealed due to particle capturing (the flat magnetic patterns are not optically visible). Once the particles saturate the first capturing squares they start to roll over and fill the subsequent squares, creating a gradient of captured particles which is evidenced by the "thickness" of the outline squares. This evolution of particle capturing is observed in the sequence of images shown in Figure 5.9. In general, the particles can be unpinned using a high flow rate, at the order of hundreds of $\mu$l/s. However, it has been observed that unpinning is impossible in some cases, mostly when the particles are small (the drag force, related to particle radius,

also decreases) and the PDMS layer above the magnets is thin (few $\mu$m).
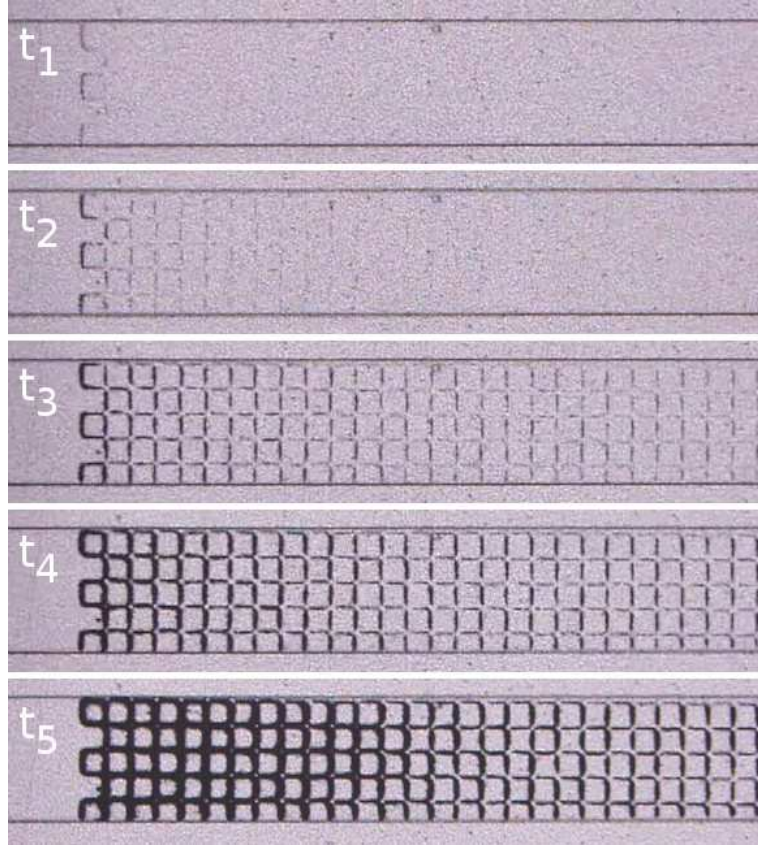


Figure 5.9: Evolution of the capture of magnetic microparticles ($\varnothing$ 1 $\mu$m) by a chessboard-like magnet array inside a microfluidic channel.

## 5.2.1  Sorting by capture

Magnetic separation, as discussed in Chapter 4, exploits the difference in the balance of forces acting, on the one side, on non-magnetic objects submitted to gravity (including buoyancy) and viscous forces (neglecting Brownian motion) and on the other side, on magnetic objects (e.g., magnetic particles), additionally submitted to a magnetic force (Fig. 5.10a).
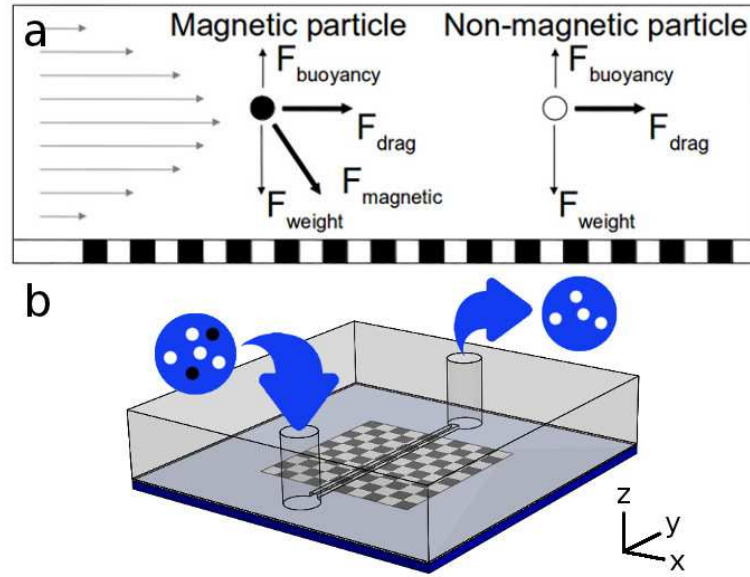
Figure 5.10: (a) Forces acting on magnetic and non-magnetic particles flowing in a micro-channel integrated above a micromagnet array. (b) Schematic of a micromagnet/micro-channel device for magnetic separation.

A magnetic separation device (micromagnets and microfluidic channel) is modeled and optimized. The technical constraints concerning micromagnet and microfluidic channel fabrication are taken into account. Two types of magnetic particles (Micro Particles GmbH, ∅ 2.8 $\mu$m and Sigma Aldrich, ∅ 1.0 $\mu$m) consisting of magnetic nanoinclusions embedded in a polymeric matrix are considered. For data analysis, the particle magnetization at 0 K is taken to be $\mu_0 M_S = 0.6$ T. In accordance with the manufacturers' specifications, it was assumed that the magnetic nanoinclusions account for 30% of the total particle weight. Fitting of the magnetization curves gives an inclusion size of 3.3 nm ± 3 nm (standard deviation) for the ∅ 2.8 $\mu$m particles and 3.6 nm ± 3 nm for the ∅ 1 $\mu$m particles (see Chapter 4). Based on these values, an average inclusion diameter of 3.5 nm ± 3 nm is assumed in the calculations.

The following considerations are assumed in the simulations:

- 5 $\mu$m-thick NdFeB films

- Magnetization of $\mu_0 M_R = 1.2$ T oriented out of the film plane.

- 500 $\mu$m-wide microfluidic channels.

- Maximum capture length of 10 mm.

- Two channel heights: 38 $\mu$m and 76 $\mu$m (corresponding to, respectively, one and two sheets of the dry-film photoresist used for micro-channel fabrication.)

- Magnets are pre-coated with a PDMS layer of 6 $\mu$m.

See Fig. 5.10b for a schematic of the complete device. Particles entering the channel are distributed all over the cross-section of the channel and are captured at different positions above the magnets. These capture position depends on the initial (x,z) position of the particle. However, the least-favorable capture conditions are considered. The particle:

- is initially at the top of the channel, where the magnetic force is the weakest and sedimentation to the bottom of the channel takes longer to occur;

- flows in the center of the channel, where the fluid velocity is the highest and the particle is dragged towards the outlet more quickly;

- passes through the center of a row of squares, minimizing the trajectory above the zones where the magnetic edge effects take place.

Initial simulations indicate that magnetic structures with very small features (few $\mu$m) and very large features (several hundreds of $\mu$m) are the least efficient in trapping particles. Thus, detailed calculations are performed for chessboard structures with feature sizes ranging from 50 $\mu$m to 200 $\mu$m. Fig. 5.11a shows the simulated trajectories of magnetic particles flowing in 38 $\mu$m-high and 76 $\mu$m-high microfluidic channels. Three different chessboard magnetic patterns ($50 \times 50\ \mu m^2$, $100 \times 100\ \mu m^2$, and $200 \times 200\ \mu m^2$) and a constant flow rate of 15 $\mu$l/min are considered. The least-favorable position considered in the simulations, as described above, is schematically represented in Fig. 5.11b.

In the case of 38 $\mu$m-high channels, both types of particles, ($\varnothing$ 1 $\mu$m and $\varnothing$ 2.8 $\mu$m) are predicted to be captured by the $100 \times 100\ \mu m^2$ chessboard structure within the maximum length of 10 mm. With the same channel height, the particles are not captured by either the $50 \times 50\ \mu m^2$ or by the $200 \times 200\ \mu m^2$ structures. For the case of 76 $\mu$m-high channels, the systems with the larger features ($100 \times 100\ \mu m^2$ and $200 \times 200\ \mu m^2$) are predicted to capture the $\varnothing$ 2.8 $\mu$m particles, but not the $\varnothing$ 1 $\mu$m particles. The system with feature dimensions of 50 $\mu$m is not suited to capture either of the particles.
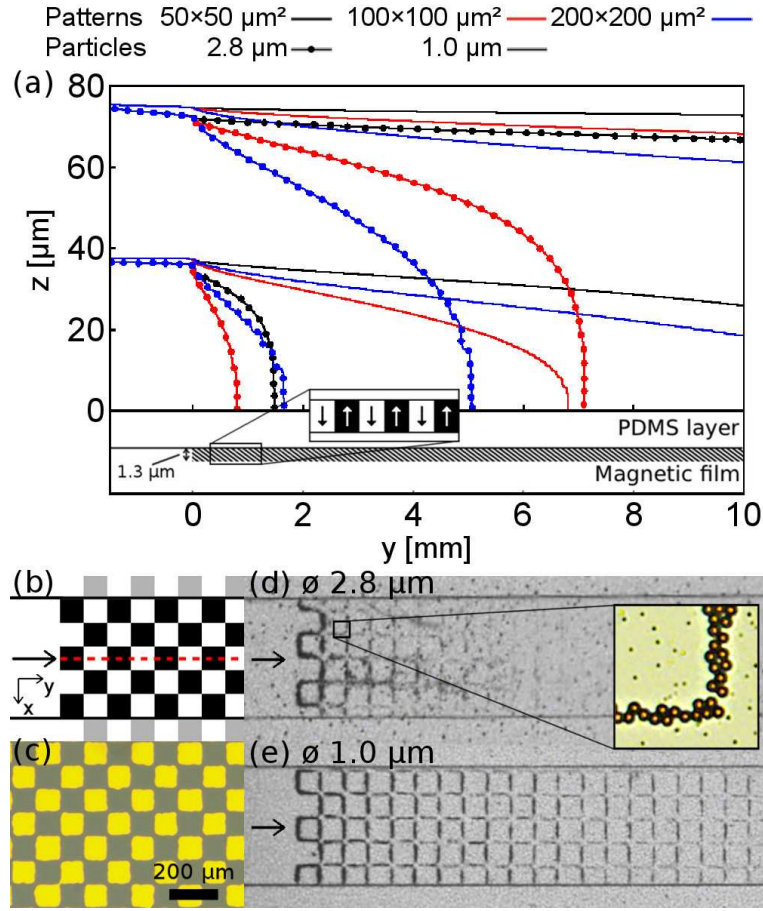
Figure 5.11: (a) Simulated trajectories of magnetic particles travelling through microfluidic channels above arrays of micromagnets of different size, starting from the top of a 38 $\mu$m or 76 $\mu$m thick channel; (b) schematic of the least-favorable lateral position for attraction considered here; (c) Magneto-optical image of an array of $100 \times 100$ $\mu m^2$ magnets. (d,e) Optical images of magnetic particles trapped above such arrays in 38 $\mu$m thick channels. Inset (d) : zoom on particles attracted to the zones of highest magnetic field gradient. The randomly positioned dark specks observed in (d) are due to cracks in the Ta capping layer which have no adverse effects on the magnets on the time-scale of these experiments.[89]

The results above show that, among the analyzed configurations, the structures which are the most efficient to capture the particles of interest are those having a feature size of 100 $\mu$m. The actual magnetic separation devices are produced based on these results. Arrays of chessboard-like $100 \times 100$ $\mu m^2$ micro-magnets are produced by thermo-magnetic-patterning over an area of $10 \times 10$ $mm^2$ of an out of plane textured 5 $\mu$m thick NdFeB film. In the magneto-optic image of the chessboard pattern (Fig. 5.11c), the black and yellow squares represent magnetization pointing out of the film plane and into the film plane, respectively. A 6 $\mu$m-thick layer of PDMS is spin-coated onto the magnetic film. Parallelepipedic microfluidic channels (width = 500 $\mu$m, height = 38 $\mu$m, and length = 15 mm) produced by replica molding are then sealed onto the PDMS layer above the micromagnet array.

Solutions containing the magnetic particles are pumped through the device. The flow

rate in the channel is fixed at 15 $\mu$l/min. Optical images of the trapped particles are shown in Figures 5.11d ($\varnothing$ 2.8 $\mu$m) and 5.11e ($\varnothing$ 1.0 $\mu$m). These were obtained after the solutions were pumped through the channels for 20 s. The particles are trapped at the bottom of the channel at the interfaces between oppositely magnetized sections of the film, where the field gradient and thus the attractive magnetic force is maximum (inset of Fig. 5.11d). The difference in the distance required to trap the particles is reflected in their distribution along the channel length. The $\varnothing$ 2.8 $\mu$m particles are trapped at the beginning of the pattern, over a distance of approximately 600 $\mu$m (the simulations in Fig. 5.11a predicted trapping at a distance of 700 $\mu$m). For $\varnothing$ 1 $\mu$m particles, trapping occurs over a distance of a few millimeters, in agreement with the above simulations (trapping predicted at 7 mm). Unpinning of the particles can be achieved by increasing the flow rate and thus the drag force.

The efficiency of the system for separating magnetic particles from non-magnetic ones is then studied. Two initial solutions are used, solution A0 containing the $\varnothing$ 2.8 $\mu$m magnetic particles and $\varnothing$ 3.0 $\mu$m non-magnetic particles (Sigma Aldrich) and solution B0 containing the $\varnothing$ 1.0 $\mu$m magnetic particles and $\varnothing$ 2.0 $\mu$m non-magnetic particles (Sigma Aldrich). In both cases, the magnetic particles count for approximately one third of the total number of particles. These solutions are passed through the channel at a flow rate of $\sim$15 $\mu$l/min and the resulting solutions (A1 and B1) of the non-trapped particles are collected at the outlet. Distilled water is then pumped through the channel at a very high flow rate ($\sim$1000 $\mu$l/min) to unpin the trapped particles, which are then collected at the outlet (A2 and B2). Figure 5.12 shows the flow cytometry analysis of all solutions. The measured initial ratios of magnetic to non-magnetic particles are in agreement with their expected concentrations (A0 and B0) while the high purity of solutions A1 and B1 (99.9% of non-magnetic particles) confirms that the magnetic particles are very effectively trapped. The solutions of the trapped particles are also relatively pure (94.7% and 99.5% for A2 and B2, respectively). The presence of non-magnetic particles in these solutions is attributed to a steric effect, as the trapped magnetic particles may block the movement of the non-magnetic particles along the bottom of the channel. This effect is less noticeable for solution B, since the barrier created by the 1 $\mu$m magnetic particles is smaller.[89]
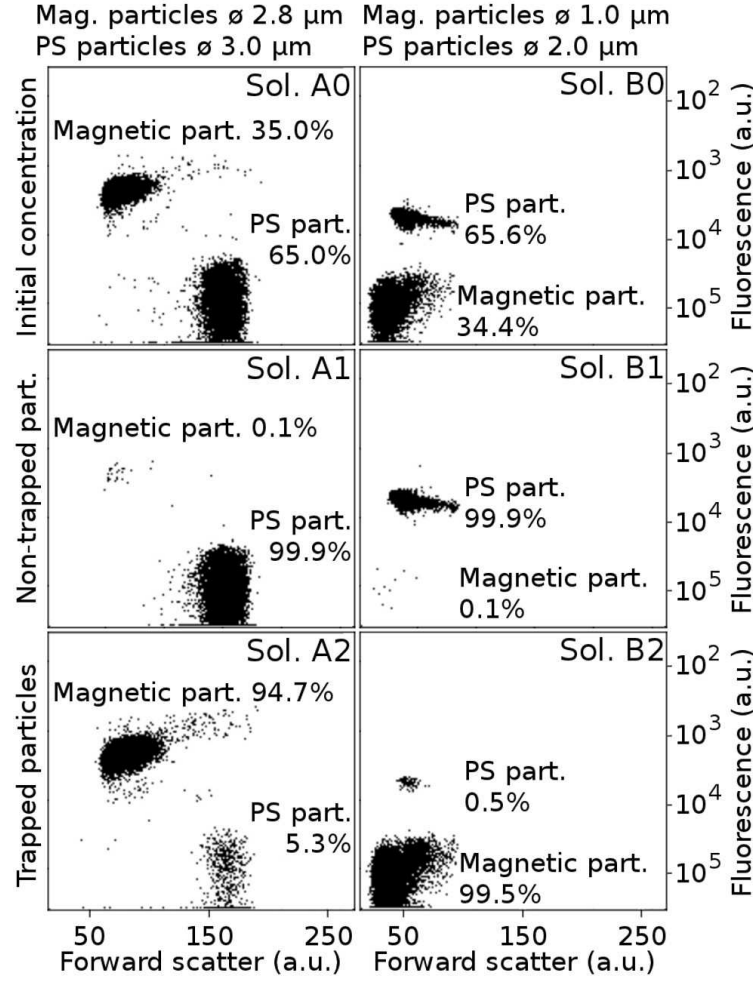
Figure 5.12: Cytometric analysis of the starting solutions containing both magnetic and non-magnetic particles (solutions A0, B0—first row), those containing the non-trapped particles (solutions A1, B1—second row) and those containing the trapped particles (solutions A2, B2—third row).

## 5.3 Guiding

Micromagnets present many advantages for microfluidics: high forces, no need of power supply, full integration and potential low cost. However, they also present a major drawback: the magnetic field - and, as a consequence, the force - is not variable and cannot be turned off. Applications such as static capture are straightforward when using micromagnets. Systems for dynamic capture, on the other hand, can be quite difficult to design. Unpinning or sequential operations are not easy tasks when powerful micromagnets are present.

As discussed in Chapter 1, such functions are successfully achieved with micro-systems integrating coils, soft magnets, etc. Here, continuous separation is shown using permanent magnets. Particle guiding towards specific positions can be performed using adapted magnets

and a dynamic driving force. Magnetic stripes are used as *rails* for the particles, while a microfluidic drag force pushes the particles forward. As discussed in Section 4.4.3, two conditions are necessary for the particle to follow the rail:

- There must be a component of the drag force which is aligned with the axis of the rail in order to induce movement;

- The component which is perpendicular to the axis of the rail has to be weaker than the magnetic force in the same axis, otherwise the particle is unpinned.

The conditions presented above assume that friction or any interactions between the particles and the PDMS layer are negligible. These hypothesis were confirmed experimentally, as no significant influence of surface forces were observed. However, several types of the most commonly studied biological elements present certain adhesion to the substrate. In this case, these factors have to be taken into account, for they can be very significant.

The second condition presented on the previous list is necessary for guiding particles, but not for particle deviation. As presented in Figure 4.12, even though a particle can be unpinned from a rail, the force generated by the magnets can be used to deviate the particle towards a certain region of the channel.

Particle guiding and deviation is presented experimentally in this section. Based on the positive results obtained, continuous magnetic/non-magnetic particle separation is also performed.

## 5.3.1   Particle guiding with parallel-to-flow lines

As a first demonstration of the possibility of guiding (instead of blocking) particles, a system with magnetic rails parallel to the channel is designed. The goal is to attract the particles towards the lines then, by rolling or sliding, guide them towards the outlet of the channel. Since the rails are aligned with the channel, no magnetic blocking force is present on the axis of the flow.

This system is also useful to estimate how the particles interact with the PDMS layer. Particle flow is observed at different flow rates (particle velocity) in order to determine the threshold of particle-to-PDMS pinning force. Since no significant force is identified (no particles are blocked), one can assume that guiding is determined only by magnetic and drag forces.

Next, a system in which the magnetic rails oriented with a very small angle to the microfluidic channel is tested. This system serves to maximize the drag force along the rails and minimize the unpinning force, optimizing the chances of particle guiding. Figure 5.13a shows a schematic representation of the device on top-view. The magnetic stripes are shown in gray and white and the edges of the microfluidic channel are represented in black. The arrow represents the direction of fluid flow.
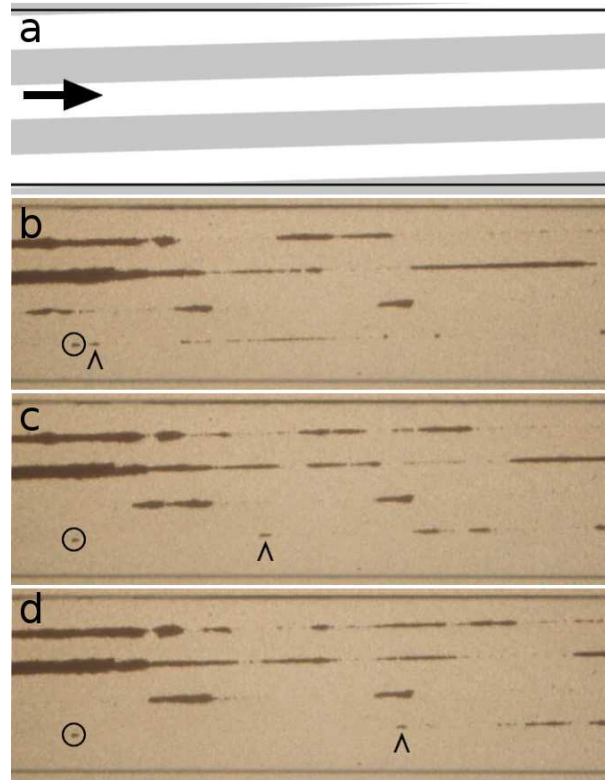
Figure 5.13: (a) Schematic representation of a system in which the guiding rails are parallel to the microfluidic channel and, thus, to the fluid flow. The experimental setup at different times is shown in (b), (c) and (d). A particle agglomerate moves along a magnetic rail, as indicated by the small arrow. The circle indicates another agglomerate which is pinned to a zone o high magnetic field gradient.

Magnetic particles with diameter around 1 $\mu$m are pumped through the microchannel. In the beginning they are dispersed at every point as regards the channel section and start to slowly sediment, since the only acting force is their weight. The density of commercially available particles is usually close to 1.3. As they approach the magnetic stripes, a magnetic force rapidly pulls the particles towards the bottom of the channel and towards the edges of the stripes. As previously dicussed, the magnetic force can be several orders of magnitude larger than the weight.

The images shown in Figures 5.13b, c and d show a point close to the channel of the center at different times. The first thing which can be noticed is that all particles are attracted to the interfaces of the magnets. No particle is found elsewhere. Moreover, the displacement of the particles occurs following the magnetic rails, as it can be observed by the group of particles indicated by the small arrow moving towards the right side of the picture.

A frame-to-frame analysis of particle position indicates that there are also "pinpoints", where the particles get stuck, which are generated by local variations in the magnetic field. A small group of particles pinned on one of these points is circled in Figure 5.13b. This group remains at the same position in Figures 5.13c and 5.13d. However, further analysis of the experiment indicate that the particles can still be unpinned if a sufficient amount of

particles agglomerate at the same point. In this case, the drag force acting on the ensemble can be sufficiently high to push all the particles as a whole.

The success of this first dynamic and continuous parallel-to-flow guiding opens the way to more complex functions, as demonstrated further ahead. However, in itself it is already a very useful function. It allows continuous extraction of particles from a volume (3D) towards a lines on a surface (1D). As a potential application, one can imagine putting cells in a reactive medium and, then, having them disposed on a single line for observation. This line can be also functionalized in order to perform further manipulations and reactions. Furthermore, counting cells and analysis are improved, since the cells can be arranged to pass by the same point sequentially.

## 5.3.2 Continuous deviation

Particle guiding is confirmed by the use of parallel-to-flow magnetic rails, opening the possibility of more complex applications. A system similar to the one showed in the previous section is designed. The difference here is that the angle between the rails and the channel is approximately 45°. The goal is to guide the particles from one side of the channel to the other. Figure 5.14a shows a schematic of the system, where the arrow indicates the direction of fluid flow.

Again in this case, particles of diameter close to 1 $\mu$m are used for the test. The particles are dispersed everywhere in the channel at the beginning and are, then, pulled down to the bottom of the channel by the first magnetic lines. Figure 5.14b, 5.14c and 5.14d show three different positions in the same microfluidic channel: close to the inlet, the center part and close to the outlet, respectively. The magnetic particles are observed to be widely dispersed along the lines, but mainly concentrated on the lower part of Figure 5.14b. The particles are captured by the line and guided to the same side of the channel, which induces a large amount of particles to accumulate on the edge of the channel. This accumulation leads to an unpinning of some particles since they start to be positioned above others and far away from the magnetic lines. The fluid flow can, then, drag these particles further on the channel.
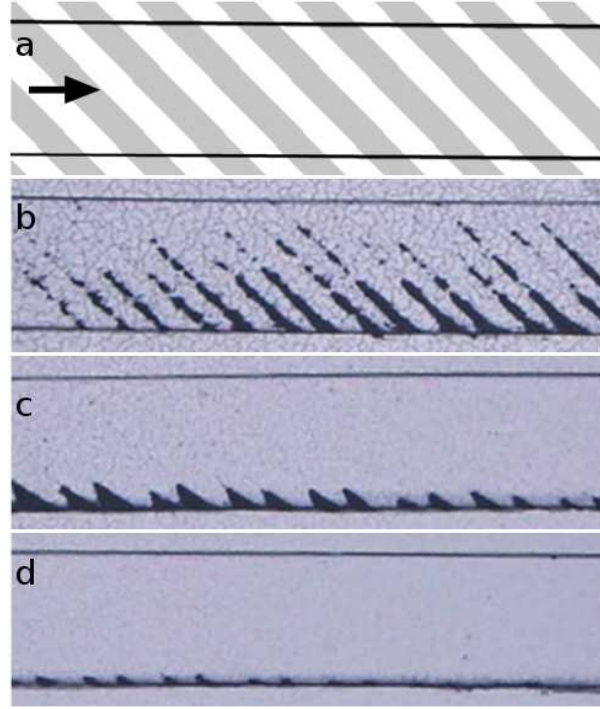
Figure 5.14: (a) Schematic of the system showing a microfluidic channel limited by the black lines with angled magnetic stripes below. The arrow indicates the direction of fluid flow. Magnetic particles deviated by the rails (b) close to the inlet, (c) in the middle of the channel and (d) close to the outlet. The particles are gradually deviated towards one edge of the channel and follow a thin streamline towards the outlet.

The middle section of the channel shows that virtually all particles are concentrated on the same edge of the channel. Deviation is achieved with a few magnetic rails (around 20). No particle can be spotted on the center or the opposite edge, proving that a highly efficient particle deviation is performed. Even further in the channel, close to the outlet, it can be observed that the last few magnetic rails increase the concentration of particles and unpinning occurs in such a way that all particles follow the streamline close to the edge of the channel towards the outlet.

If one considers that the outlet of the channel is divided in two parts, a solution free of particles could be collected in on side, while another solution containing all the particles would be collected on the other outlet. In the next section a system based on this principle is presented and qualitatively and quantitatively analyzed.

### 5.3.3  Continuous sorting

Based on the previous experiments of deviation a system which can perform particle sorting is designed. A schematic is shown in Figure 5.15. The system is composed of a 1500 $\mu$m-wide, 38 $\mu$m-high channel with two inlets and two outlets. In one of the inlets a buffer solution is pumped, while a solution containing magnetic (black) and non-magnetic (white)

particles is pumped in the other, with a lower pressure. The difference in pressure is used to limit the particle-charged solution to a thin line on one side of the channel. The outlets are maintained at the flow rate (same pressure) in order to collect the same amount of liquid. Note that part of the buffer solution flows out of the channel through the upper outlet. A 12 $\mu$m-thick PDMS layer separates the channel from a set of magnetic stripes. Five 50 $\mu$m-wide stripes separated by 50 $\mu$m were produced by TMP, resulting in ten magnetic rails (ten interfaces between up and down oriented magnets). The angle between the axis of the channel and the stripes is 30°.
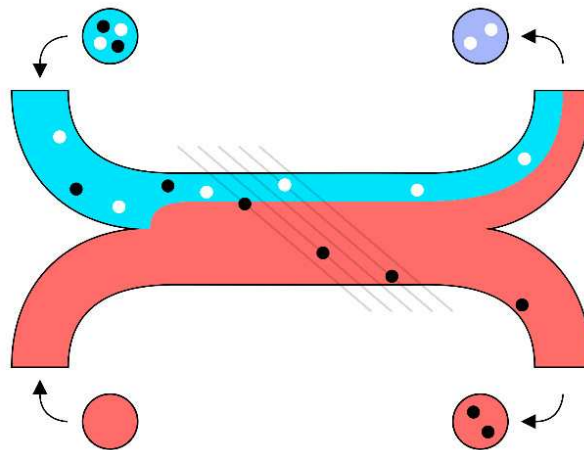


Figure 5.15: Schematic of the system used for continuous magnetic sorting, composed of one channel with two inlets and two outlets. Non-magnetic and magnetic particles are pumped in, concentrated at first on one side of the channel. Magnetic particles are deviated by the magnetic rails and collected on one outlet, while non-magnetic particles follow their initial streamlines and are collected on the other outlet.

Non-magnetic particles flow through the channel without being affected by the magnetic field created by the micro-magnets. These particles follow the streamlines of the blue liquid towards the outlet of the channel. Magnetic particles, however, are attracted by the magnetic stripes and deviated from their initial streamlines. A combination of drag force and magnetic force deviates the black particles in the figure from one side of the channel to the other. In this case, the purple and red solutions collected from the outlets will contain non-magnetic (non-deviated) and magnetic (deviated) particles, respectively.

Using the model developed in Chapter 4, the system described above is simulated for commercial magnetic particles purchased from MicroParticles GmbH. These particles are composed by up to 30% wt of iron oxide (magnetite or maghemite) dispersed as nanoparticles in a polystyrene medium. The whole particle diameter is 2.8 $\mu$m. The simulations show that in the main channel a flow rate up to approximately 25 $\mu$l/min can be used to deviate the particles towards the opposite side of the channel. With this flow rate particle are not guided by the first magnetic rail, but deviated by each rail towards the opposite side (see Figure 4.12).

Actual experiments show that, due to the pinning of the first particles on the magnetic rails and subsequent deviation of the following particles from the main path, the simulated flow rate of 25 $\mu$l/min cannot be used. A much lower flow rate has to be used in order to sufficiently deviate the particles. In this case, the average flow is approximately 15 $\mu$l/min. In order to prove the possibility of particle sorting, $\varnothing$ 1 $\mu$m polystyrene particles are pumped in along with the magnetic particles.

Figure 5.16 shows the center zone of the channel, where particle deviation occurs. The upper blue part initially containing the particles and the lower red buffer can be identified, as already schematically shown. The rails are outlined by the magnetic particles: both particle pinpoints and the thick line of particles which accumulate and are guided by the rails are observed. The first magnetic line on the left is clearly more charged with particles, indicating the high efficiency of particle attraction and capture. The lines on the right tend to be less charged in particles, since the latter are released and re-captured until they reach the edge of the channel.
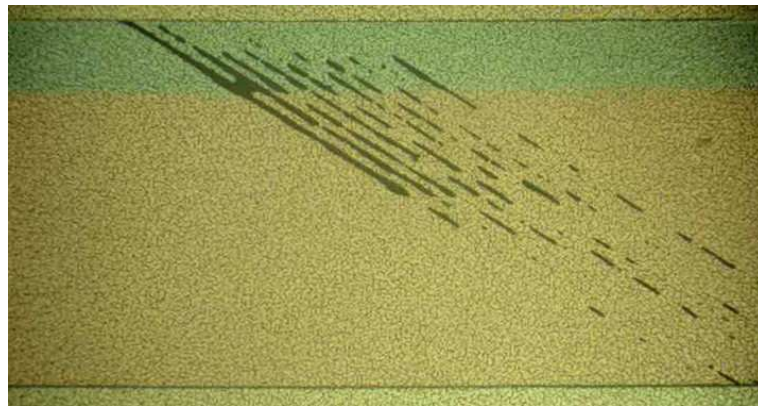


Figure 5.16: A microfluidic channel below which magnetic stripes are positioned. The stripes are outlined by magnetic particles which enter the channel on the upper left of the figure (blue liquid) and are deviated towards the bottom right. Non-magnetic particles – not visible in the figure - follow the streamlines without being deviated by the magnetic field.

Non-magnetic particles flow in the blue liquid towards the upper outlet of the channel. These particles cannot be observed in the previous picture, but are clearly discerned from the magnetic particles during the actual experiment. The resulting solutions are collected for particle counting in flow cytometry.

Figure 5.17 presents the resulting concentrations of particles measured by flow cytometry. The blue solution contained initially 27.3% of magnetic particles and 72.7% of non-magnetic particles, almost a ratio of 1:2. In the solution shown in purple in Fig. 5.15, i.e., the one containing the non-deviated particles, the amount of non-magnetic particles (92.8%) highly overcomes the amount of magnetic ones (7.2%). This increase in concentration indicates a very high efficiency in magnetically deviating the particles inside the microfluidic channel. On the other hand, the outlet containing the red solution presents 99.3% of magnetic

particles, while the non-magnetic particles account for 0.7%. The presence of non-magnetic particles in the "deviated group" is associated to the formation of a barrier of magnetic particles on the rails and the subsequent deviation of non-magnetic particles towards the other side of the channel. Notice that the initial amount of non-magnetic particles in the mixed solution is much higher than the amount of magnetic particles, which explains their non-negligible presence in the deviated group.
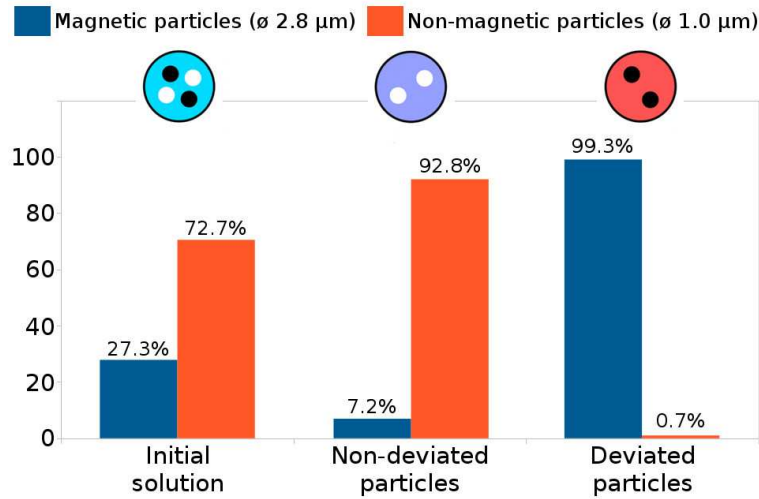


Figure 5.17: Particle counting performed by flow cytometry in the initial solution (blue) containing both magnetic and non-magnetic particles, the solution containing the non-deviated particles (purple) and the solution containing the deviated particles (red).

The system presented here has proven the possibility of autonomous particle sorting in continuous flow. High efficiency on particle sorting was obtained. Though not all the particle have been sorted, this can be improved by an optimization in the design of the system. For instance, the number of rails can be increased and their angle can be reduced, with a consequent increase in the length of the channel.

These results are very interesting for a number of applications. The fields of medicine and biology, for instance, can benefit from a significant improve in dimensions, performance and autonomy of lab-on-chip and point-of-care systems based on permanent micro-magnets. This first example of selective particle deviation gives also a hint of the many other, more complex, configurations which can be obtained using such devices. A few of the idealized and in-development systems are shown in the next section.

## 5.4   Microfluidics with TOPO magnets

Recent efforts have been done on the integration of topographic magnets to microfluidic systems, as shown in Chapter 3. These so-called TOPO magnets are thick (5 to 50 $\mu$m)

magnetic films deposited on a silicon wafer pre-etched by DRIE. The main advantage, as compared to TMP magnets, is the higher fields and gradients which can be achieved at a considerable distance from the magnetic layer.

The final experiments of P.-C. Filippou's internship between Institut Néel and G2Elab concerned the use of these magnets in microfluidics. Early qualitative results which already indicate success in pinning and guiding particles are shown below.

Figure 5.18a shows a top view of a microfluidic channel built above a set of topographically patterned magnetic circles. Note that the microfluidic channel is placed above the central row of circles. The upper and lower rows are outside the channel. The circles have a diameter of 100 $\mu$m and are spaced by 400 $\mu$m. A capping layer of PDMS with 5 $\mu$m in thickness separates the bottom of the channel from the magnets.

It can be observed that the $\varnothing$ 1 $\mu$m magnetic particles pumped in the channel are attracted to the edges of the circles. The higher magnetic force observed in these zones is clearly evidenced by the large amount of particles outlining each magnetic feature. A zoom in one of the circles (Fig. 5.18b) shows that a thick line of magnetic particles accumulate on the same magnetic feature and apparently no particles remain elsewhere.
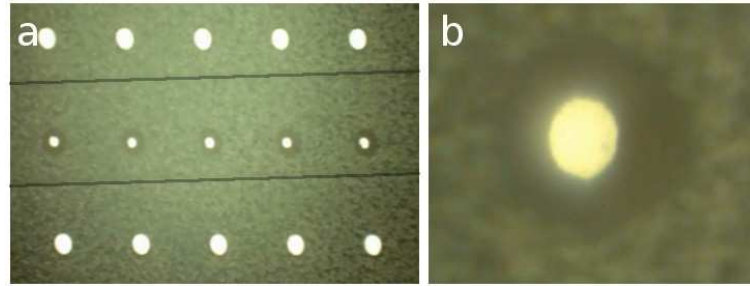


Figure 5.18: (a) Magnetic particles flown through a channel built above topographically patterned magnets are attracted to the edges of the circles. (b) A zoom in one of the circles shows that the particles follow the zones of highest magnetic force, i.e. the edges of the patterns.

Successful guiding is also observed using TOPO magnets. Figure 5.19a shows a set of 100 $\mu$m-wide magnetic stripes with a microfluidic channel, which is separated from the magnets by a 5.5 $\mu$m-thick PDMS layer. The fluid flows from left to right and the angle of 30° deviates the $\varnothing$ 2.8 $\mu$m particles towards the right edge of the channel.
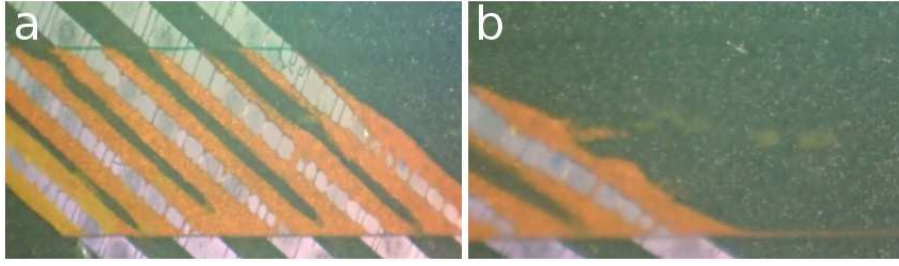
Figure 5.19: (a) Magnetic particles flowing in a microfluidic channel and being deviated by the magnetic stripes. (b) Zoom in: The thin line of particles flowing away from the stripes indicates the high efficiency of particle deviation.

Once again the particles outline the magnetic features. The wide distribution of particles on the lines is an indicator of the very high magnetic forces obtained with the TOPO magnets, especially at such close distances. This corresponds to the model developed in Chapter 4, which showed that a larger force can be obtained around the edges of the magnets, both horizontally and vertically.

A zoom in the edge of the channel, close to the last magnetic stripe (Fig. 5.19b) indicates that the particle are indeed deviated, as proven by the accumulation of particles on this zone. A thin line of particle leaving the magnetic features and following the fluid flow direction can be observed, indicating strong particle guiding.

The qualitative results obtained with TOPO magnets indicate that they are suited for particle capturing and guiding with very high efficiency. The wide distribution of particles outlining the magnetic features gives an idea of the strong magnetic force which can be obtained in a fairly large area. These characteristics make TOPO magnets very promising not only for the applications discussed here, but for many other applications in the MEMS field.

Further work is in development at the moment in order to quantify the efficiency of microfluidic systems based on TOPO magnets and to push down the limits of particle sizes which can be captured, while pushing up the speed of capturing.

## 5.5 Towards more complex configurations

Based on the quantitative results obtained with both static (particle positioning) and dynamic (sorting by capture and continuous flow sorting) system, a few more complex configurations have been designed. Some of these configurations have been qualitatively tested and the preliminary results are shown below.

## 5.5.1 Particle focusing

A schematic of a system designed to focus particles is shown in top-view in Figure 5.20a. The edges of the microfluidic channel are shown in black, while the up and down magnetic patterns are shown in gray and white. The direction of fluid flow is once again represented by a black arrow. The goal of this configuration is to bring particles dispersed in three dimensions to a single line on the bottom of the channel.

The particles are, at first, attracted to the magnetic lines and, thus, guided towards the final point of the line. In this case the final point is positioned in the center of the channel and guiding rails are produced in both sides, as a V-shaped pattern. Obviously, the final line can be positioned anywhere in the channel – close to an edge, for instance – but in this case the middle point is chosen so as to demonstrate that the magnetic particles can be collected in an outlet positioned in the center of the channel.
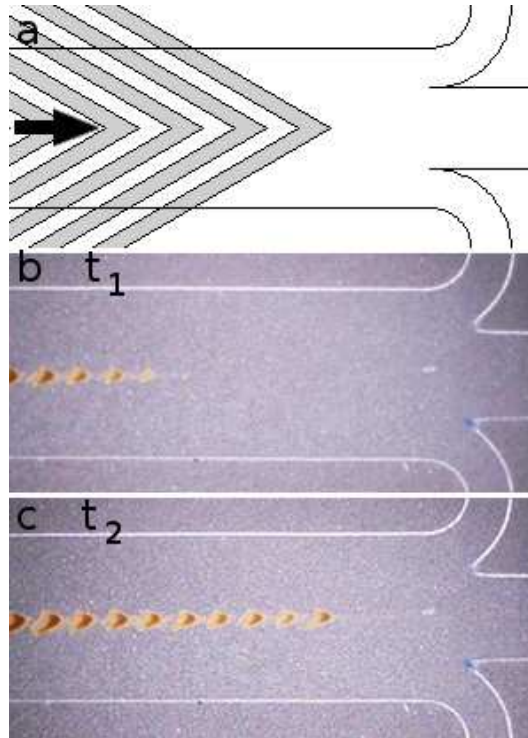


Figure 5.20: (a) Schematic of a particular configuration of the device designed to focus magnetic objects on a single line. The actual experiment shows that the particles are (b) concentrated in the center of the channel and (c) follow the magnetic patterns until the end of the channel, where the fluid flow pushes them towards the outlet.

Figures 5.20b and c show $\varnothing$ 1 $\mu$m magnetic particles attracted to the V-shaped patterns in the end of the channel, close to the outlets, at two subsequent times during an actual experiment. As it can be observed, the first magnetic rails successfully attract and guide the particles to the center of the channel, which are then pushed by the fluid flow to the

next pattern. The particles follow this process of saturation of a line and attraction by the subsequent line until they reach the last line in the group. At this point, once the particles are released, they follow a thin streamline towards the outlet, as observed in the right-hand side of Fig. 5.20c.

It has been successfully shown that focusing of particles is also possible using microfluidics and autonomous micro-magnets. The possibility of aligning objects side-by-side in a single line can be widely used, for instance, in cell biology to study cell growth or horizontal transfers. It is also very interesting to limit the continuous scanning of a chip while observing magnetically tagged objects, due to the possibility of observing a single point above the final line of objects with very high precision.

## 5.5.2   Selective unpinning

Another possibility of particle sorting can be exploited once all particles are focused in a single line. In the system present here, a continuous magnetic rail is added after the focusing patterns. This rail is parallel to the microfluidic channel up to a certain point, where it becomes perpendicular to the channel with a gradual transition - a rounded corner. The balance between the drag force and the magnetic force allows the control of the unpinning site. This control is possible due to the balance between the drag force (varying along the cross-section of the channel) and the magnetic force (the pinning component, parallel to the drag force, varies along the angle of the magnetic rail).
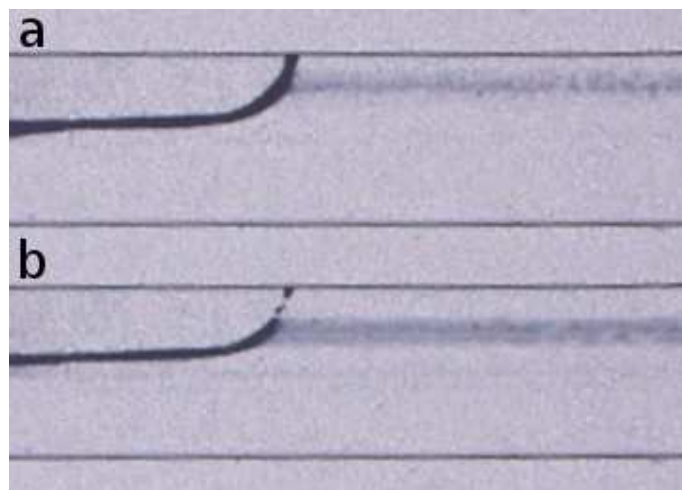


Figure 5.21: After being focused in a single line, a curve developed in the magnetic pattern can be used to unpin the particles at different sites. A low flow rate induces unpinning close to the edge of the channel, while a high flow rate unpins the particles in the beginning of the curve.

It can be observed that at low flow rate (Figure 5.21a) the particles are guided by the parallel line and, in average, follow the rounded corner until close to the edge of the channel.

At this point, the drag force overcomes the magnetic force which keeps the particles pinned to the rail and they are dragged by the flow. A thick line of dragged particles can be observed, indicating that unpinning occurs at a relatively wide zone of the curve. Increasing the flow rate induces the particles to be unpinned closer to the beginning of the curve, as shown in Fig. 5.21b. In this case the force which deviates the particles is not sufficiently strong to keep them pinned to the rail after the angle increases of a few degrees, thus, the drag force becomes dominant.

Considering that two objects labelled with different amounts of magnetic material will interact differently with the micro-magnets, the magnetic configuration can be engineered so that the unpinning sites will be different. The difference in the drag force acting on the object can also play a role, if their sizes and/or shapes are different. In this manner, continuous selective sorting can be obtained with the system presented here for two or more labelled objects.

### 5.5.3 Multiple particle sorting

Another configuration proposed for multiple particle sorting is based on a set of magnetic rails disposed at a certain angle related to the micro-channel. The idea is basically what has been shown in Figure 4.12 and adapted in Figure 5.22. All the magnetically labelled objects are, at first, concentrated on one side of the channel, then flow above the set of magnetic patterns. Particles containing more magnetic material will be strongly influenced by the magnetic force and highly deviated, while a lower magnetic content will result in a less-pronounced deviation. Preliminary experimental results with this configuration have been obtained but are not sufficiently evolved.
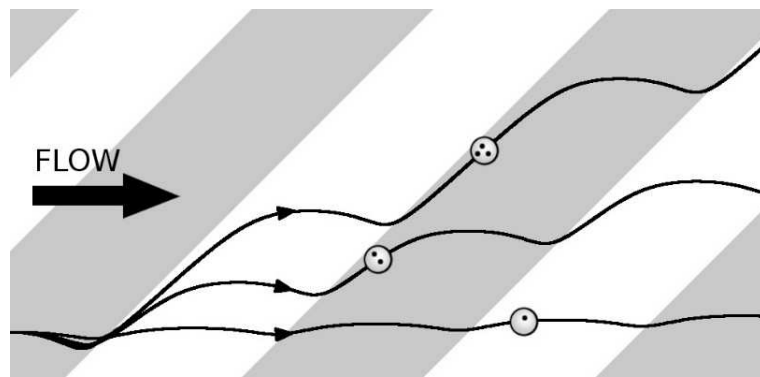


Figure 5.22: Schematic of a microfluidic channel above a set of magnetic patterns (gray and white). Objects labelled with different amounts of magnetic materials are more or less deviated by the magnets and can be collected at specific regions of the channel.

The principle of exploiting the difference in the force created by a same set of magnets acting on different magnetically labelled objects has been shown by Pamme et al. and Adams

et al., for instance. The advantages brought by the system proposed here, as regards the other reported systems, are the autonomy of the magnetic field and the significantly reduced dimensions of the final device.

## 5.6 Partial conclusion

In this chapter flat magnetic films patterned by TMP have been used to demonstrate particle attraction and alignement. Precise positioning has been performed using individual magnetic features with dimensions similar to those of the particles. The great potential of this proofs of concept have been confirmed with biological entities which were capture on the same type of magnets. In a collaboration with the Ampère Laboratory, specific biological processes were studied. Endocytosis of particles by HEK293 cells were analyzed as a function of particle concentration and time of exposure. Encouraging results on cell biology were obtained by the simple cell positioning above TMP magnets.

In a step towards integration to microsystems, the magnets were integrated to microfluidic channels. At first, TMP magnets with chessboard patterns were used to capture and sort magnetic/non-magnetic particles in a fluidic flow. A controlled capture was obtained, with particles being captured on the first few magnetic squares and slowly filling the subsequent squares. The size of the particles has been observed as a major point on the determination of the parameters of the experiment. A compromise between flow rate and the thickness of the PDMS cover layer had to be established for successful particle capture. Very good agreement was obtained between the experimental results and the model developed in Chapter 4. Particle separation was predicted and the system was optimized prior to its actual development. High sorting efficiency was obtained with different dimensions of magnetic and non-magnetic particles.

Continuous sorting was also performed using magnetic rails. A set of magnetic stripes was developed parallel to the fluidic flow. Particles were extracted from a 3D dispersion towards isolated lines on the bottom of the channel (1D). Then, they were guided by the rails towards the outlet using the fluidic force. Continuous particle deviation was performed using magnetic stripes disposed with a given angle related to the fluidic flow. Particles were pumped in one side of the channel and guided to the other side using magnetic rails. Optical observations showed that all particles were concentrated at a thin line close the edge of channel.

In order to quantify this deviation, particle sorting was performed. Magnetic and non-magnetic particles were pumped in the same inlet of a microfluidic channel. Magnetic stripes integrated to this channel were responsible for guiding the magnetic particles towards the opposite edge of the channel. The two types of particles were collected on two different outlets. Flow cytometry analysis showed that very high purity was obtained with this method of sorting.

Preliminary results on the use of TOPO magnets for particle capture and sorting were shown. Successful capture was performed using magnetic disks planarized with a PDMS layer. Rapid attraction and saturation with particles was observed on the edges of the disks,

proving the good quality of such magnets. The first results of particle deviation were also encouraging. A very large amount of particles was attracted and deviated by the magnetic stripes. However, the pinning force was observed to be too strong and part of the particles remained stuck. This is another indicator of the high performance of the TOPO magnets. An increase in the PDMS cover layer thickness can be enough to adjust the pinning and the guiding forces.

Other potential functions and applications have also been showed as perspectives for the Bio-Mag-MEMS. Single-line focusing can be very interesting for a sequential study of magnetically labeled objects or, simply, for counting. Selective unpinning is also an integrated way of performing extraction of cells from the volume, focus on a single line for observation and further sorting to obtain isolated populations. These applications are shown experimentally with a few first tests with magnetic particles. Finally, multiple particle sorting is demonstrated theoretically based on the previously developed simulations. Different types of objects can be sorted using magnetic stripes based simply on their size or the amount of magnetic material they are carrying.

All these models and experimental results present significant potential on Chemistry, Biology and Medicine. Most of the systems discussed here have been developed, tested with model particles and quantified, showing that their real application can be straightforward. Furthermore, the tests performed with living cells and bacteria prove that the micromagnets can be rendered biocompatible and do not influence (at least at the time-scale of the tests) the normal biological activity.

The autonomous nature of the micromagnets, which require neither external magnetic field nor power source, enables the use of such devices in combination with analytical equipment where sample space is restricted (e.g., microscopes, spectrometers...). The stray fields of micromagnets are essentially restricted to the region of interest, the microfluidic channel, thus undesirable stray fields in the environment of the device are negligible. Beyond lab-on-chip applications in biology, the micromagnet arrays studied here could also be exploited in the fields of chemistry (e.g., migration-based analytical methods) and physics (e.g., atom chips).

# Conclusion

This report presents part of the effort of a group of laboratories in developing autonomous microsystems for micro-object handling. Due to the previous expertise of Institut Néel on the fabrication and application of permanent micro-magnets, the main actuation force selected for this purposed was magnetic. These micro-magnets present a series of positive characteristics. First of all, they can generate an autonomous magnetic field, which induces a permanent force on a magnetic object nearby. Since no external power source is needed, they can be integrated to autonomous systems, which can have reduced dimensions.

Another major advantage of magnetic actuation is that no direct contact with the target object is needed. As a consequence, micro-magnets can be covered with a protective layer and placed near the object of interest, even in an aggressive environment. They can also be rendered biocompatible for bio-medical applications, or simply covered by a layer with specific functions.

The *permanent* character of magnets can be seen as an advantage or a drawback, depending on the situation. In the cases where complete autonomy is required, this feature is an advantage, as mentioned. On the other hand, when a magnetic object has to be captured and released, this last step may not be as straightforward as the first.

In this work the magnetic actuation forces are coupled with a fluidic drag force. This force was produced within microfluidic channels. Microfluidics present numerous advantages, such as the minute amounts of liquid which can be handled, the precise control of mixing reactions obtained inside the channels, etc. In this work, the most relevant feature of microfluidics was the laminar flow regimes. It significantly enhanced the way the particle-magnet and particle-fluid interactions were observed. The predictability of particle trajectory allowed not only modeling of the complete system, but also its optimization.

The first part of this work consisted of developing micro-magnetic flux sources. Triode sputtering has been presented as the most adapted technique for the deposition of thick, high-quality magnetic films (NdFeB, SmCo and FePt). NdFeB films were preferred, with remanence around $\mu_0 M_R = 1.2$ T and coercivity around $\mu_0 H_C = 2.0$ T. Adapted magnetic characterization techniques (magneto-optic imaging and magnetic force microscopy) were briefly introduced. Two techniques for the microstructuration of the films were developed and discussed. The first technique consists of creating physical irregularities in the film in order to produce local magnetic field gradients. This can be achieved by etching a flat deposited film in order to create topographic patterns or by etching the substrate prior to the deposition of the film. Both methods result in the so-called *topographic magnets* or *TOPO magnets*. The thickness of these magnets are usually in the range of 5 to 100 $\mu$m, with lateral feature dimensions down to 5 $\mu$m. Due to the considerable thickness, a significant magnetic actuation force can be obtained at a distance up to 100 $\mu$m, depending on the object of interest.

The second technique exploits the temperature-dependance of coercivity to create

micro-patterns in a flat magnetic film. At the same time a patterned laser beam locally heats the magnets, an external field reorients the magnetization on the sufficiently heated zones. This process result in the *thermo-magnetically patterned magnets* or *TMP magnets*. Thicknesses of 1 to 1.5 $\mu$m are obtained in this case. The magnetic force is, thus, much more concentrated in a zone close to the magnetic film. Very high magnetic field gradients can be produced in these zones. A great advantage of this technique is the possibility to produce very complex magnetic patterns, since the magnetization can be locally reoriented in any direction (for isotropic films). The lateral feature dimensions are mostly limited by heat diffusion (1 $\mu$ in 20 ns), thus resulting in a minimum feature width of about 2 $\mu$m.

Another technique worth discussing, but which was not used in the systems presented here, is the *micro-magnetic imprinting* or *$\mu$MI*. Hard magnetic powders (or soft magnetic powder, or yet superparamagnetic particles) are precisely positioned, aided by a micro-patterned magnet. Note that this magnet is ideally a TOPO or TMP magnet for their high magnetic field gradients which improves particle positioning. Once the magnetic powder or particles are positioned, a polymeric matrix is applied on the system. This polymer embeds the particles and, once peeled off, results in a magnetic system which can be flexible, transparent and biocompatible.

The next step consisted in integrating the TMP and TOPO magnets to the microfluidic devices. A first effort has been done in applying a protective PDMS layer above the magnets. In the case of TMP magnets, this layer served both to protect the magnets from the attack of the liquid medium in the micro-channels and to protect any biological elements from the magnets. For TOPO magnets this first layer served also as a way to obtain a flat surface, since the topographic features would not be adapted to microfluidics.

The fabrication of microchannels using a dry film photoresist was presented. The micro-channel fabrication techniques presented here have the advantage of being simple and cheap. No toxic material was used, and all the steps could be developed in a standard working environment, without the need of an actual clean room. The methods used to assemble the systems were described and the microfluidic flow control equipment was presented.

A model of the different parts of the devices was developed separately and, then, assembled in order to predict particle trajectory in the microfluidic channels. At first, the superparamagnetic responses of particles was measured experimentally and fitted with a Langevin model. Then, the magnetic fields and gradients generated by TMP and TOPO magnets were calculated and compared. The microfluidic flow was also simulated. These three parts were integrated in a single, dynamic model and particle attraction was simulated. At first capture using chessboard-like magnets was studied. The conditions for pinning and unpinning particles could be determined. An optimized magnetic configuration was determined based both on simulations and experimental results. A more complex arrangement of magnets was also simulated, considering stripe-like magnets disposed with a certain angle, related to the flow direction. Particle deviation and guiding was simulated with this model.

Finally, experimental results were obtained with the attraction of particles and biological elements. At first, static capture was performed using magnetic particles. The distribution and alignment of particles with different dimensions was studied using various magnetic

patterns. Different capture modes could be observed for each particle size. The smaller particles were more susceptible to local field gradients, while bigger particles were aligned only around the magnetic features. Single particle positioning was shown with isolated magnetic features with dimensions comparable to those of the particles.

Biological elements (cells and bacteria) were used to demonstrate the potential applications of the micro-magnets to biology. Magnetically labeled, living elements were placed above the magnets and their distribution was observed. As predicted, they outlined the magnetic pattern as previously observed with magnetic particles. Endocytosis processes of cells were analyzed using magnetic nanoparticles. Cells were exposed to the particles for different times and at different concentrations. Their particle uptake ability was measured by observing how the cells were aligned on the magnetic pattern. A saturation point for both the concentration of particles (3000 particles/cell) and the exposure time (4 h) could be estimated.

Once static capture was performed, the next step was to capture particles in a microfluidic channel. Using the integrated magnets, particles of different size were pumped through the channels and captured by the magnets. The parameters for capture could be observed and confirmed the predictions of the model. Particle sorting was also performed, using magnetic and non-magnetic particles. A very high sorting efficiency (up to 99.9% of purity) was obtained with different sizes of particles.

More complex system were developed to validate the simulation particle deviation and guiding. Magnetic stripes parallel to the channel were produced, at first, in order to observe any possible particle-PDMS interactions. Since no significant friction force was identified, angles lines were produced for deviation. Particles were pumped through the channel and deviated by the magnetic stripes, resulting in a concentration of particles close to the edge of the channel.

A similar system was produced in order to perform continuous flow separation. Magnetic and non-magnetic particles entering the micro-channel close to one of its edges were submitted to the force created by a set of magnetic stripes. The magnetic particles were deviated to the other side of the channel, while the non-magnetic particles were not affected by the field. The two resulting solutions collected on separate outlets were measured by flow cytometry and confirmed a very high sorting efficiency (at least 92.8% of purity).

As a perspective for future applications, preliminary experimental results are shown for different systems. Particle capture and deviation is performed with TOPO magnets. A strong attraction force is evidenced by the amount of particles outlining the magnetic features and the resistance to the drag force. More complex functions involving TMP magnets are also presented. Particle focusing in a single line is experimentally demonstrated using V-shaped magnets. Size- or content-selective sorting based on the balance of magnetic and drag forces is shown with a curved line. Finally, sorting of particles with different sizes or different magnetic contents in a single channel is theoretically demonstrated.

The multidisciplinary research presented here leaves very promising hints for the development of autonomous micro-systems. First of all, the micro-magnets developed so far can be fully integrated to devices fabricated with standard micro-fabricated techniques. The magnetic fields and gradients they generated are completely autonomous and restricted

to the few hundreds of micrometers around the magnetic pattern. This characteristic allows the design of devices compatible to other equipment, such as microscopes, without interfering in the normal operation of the latter.

Furthermore, the possibility to position particles or magnetically labeled objects without the need of external power supply allows the development of system which can be stored for an indefinite time. In this manner, biological elements can be precisely position and store in an adapted environment for further analysis. Applications inside the human body can be envisaged, since the micro-magnets can be rendered biocompatible. In the framework of collaborations with the CEA Grenoble Clinatec and the GIN laboratory (Grenoble Institut de Neurosciences), tests were already performed. Implants were successfully placed inside rats and pigs and trapped 10 nm MRI nanoparticles which were previously injected in the animals.

The functions presented here which include fluidic flow are also promising, due to the complete compatibility with the most standard microfluidics. In what concerns the use of an assembled system, only a pressure source is required. Numerous functions can be developed using plug-and-play systems, due to their simplicity. Several applications in the field of micro-total-analysis-systems ($\mu$TAS) and point-of-care (POC) devices are possible.

The results presented here are, in summary, the first few steps on the development of fully integrated and highly performing autonomous micro-devices. Bio-Mag-MEMS have a great, but yet unexploited, potential for the bio-medical and several other fields.

# Annex A - Analysis of Thermo-Magnetic Patterning

Anisotropic, high-quality NdFeB films are used for an analysis of the process' parameters on the final lateral dimensions of the magnetic pattern. Note that the TMP process was carried out in the SPCTS, Limoges, prior to the installation of the laser equipment in Institut Néel. Hence the laser pulse duration is 25 ns, and not 20 ns as in the standard TMP previously presented in this report.

An adapted apparatus is used in this case, as schematically represented in Figure 1. The sample is placed on top of an electromagnet which produces a magnetic field pulse opposing the film's initial magnetization. In certain cases, a heating plate consisting of a circuit printed on a silicon wafer is used to heat the sample. A KrF excimer laser pulse with 25 ns duration and 248 nm wavelength locally irradiate the film. An attenuator is used to adjust the fluence (energy per unit area) of the laser. TEM grids are used to produce patterns with matrices of 7 $\mu$m-sided squares separated by 5 $\mu$m. Synchronization of the laser and the magnetic pulses is achieved using a delay generator (Stanford DG535) connected to both equipments.
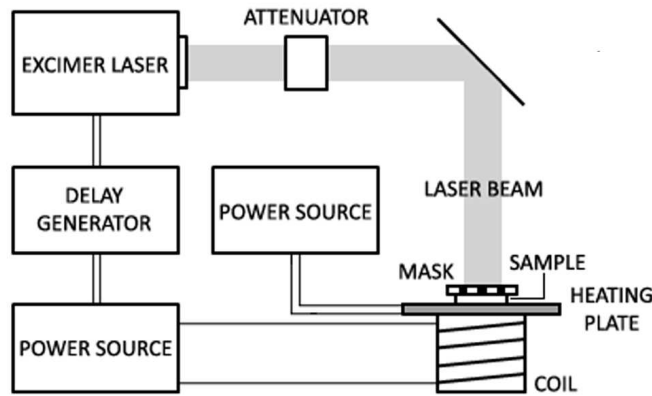


Figure 1: Schematic representation of the TMP apparatus.

Figure 2 shows MFM images of the resulting micro-magnets when the parameters of TMP are varied. Figures 2a and b present the patterns obtained with an applied field of 1.6 T, a fluence of 270 mJ/cm$^2$ and a temperature of, respectively, 50 °C and 120 °C. The increase in temperature does not result in an increase of the width of the reversed squares (8.0 $\pm$ 0.4 $\mu$m for Fig. 2a and 7.9 $\pm$ 0.3 $\mu$m for Fig. 2b). Nevertheless, reversal of the non-irradiated zones is observed in both cases and increases as the temperature increase, due to the action of heat and the external field acting on the film. Laser irradiation in the absence of a magnetic field also results in patterning of the films, as shown in Fig. 2c. In

this case, the obtained squares are not saturated, as one can see by the black and white features inside the irradiated zones. The heat introduced by the laser is sufficiently high to demagnetize the film, resulting in such features, which have been also observed in completely demagnetized samples. Increasing the fluence (400 mJ/cm$^2$) increases the size of the squares to $8.8 \pm 0.1$ $\mu$m. The pattern shown in Fig. 2d has been produced under the same conditions as the previous pattern, but in the presence of an external field of 1.6 T. The size of the squares remains unchanged ($8.9 \pm 0.2$ $\mu$m) and confirms that the dimension of the features depends mostly on the used fluence. In this case, due to the application of an external field, the squares are completely reversed. Reversal of non-irradiated zones is also observed. A high fluence was applied, thus extra heat diffused into the film and the external magnetic field reversed the sufficiently heated zones.

Note that the stronger black or white phase contrast observed on the edge of the squares is attributed to an in-plane component of the magnetization of the tip used on the MFM. At the interfaces between the features, i.e. where the magnetization changes from up to down, the field generated by the magnet in the in-plane direction is significant and interacts with the in-plane magnetic component of the tip. Reversal of non-irradiated zones is also observed, as a consequence of the action of the external field on low coercivity grains.
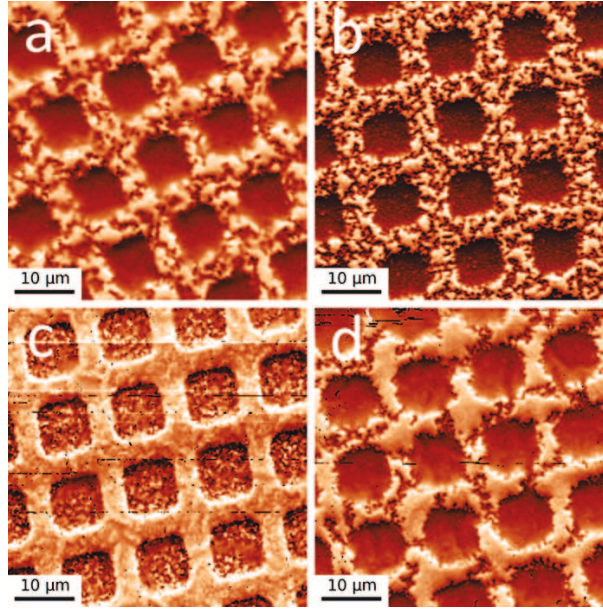


Figure 2: MFM analysis of the patterned features. TMP was performed using different parameters, as discussed in the text.

A finite element heat diffusion model is developed using COMSOL Multiphysics[2]. A standard {Ta (100 nm) / NdFeB (5 $\mu$m) / Ta (100 nm)} film on a Si / SiO$_2$ substrate is modeled. The properties used for each layer are shown in Table 1. The energy from the laser is considered to be absorbed and heat a zone of $7 \times 7 \times 0.1$ $\mu m^3$ at the surface of the film.

---

[2]A detailed description of the model can be found in [90]

Note that the laser penetration depth is estimated to be around 8 nm. However, very similar temperature profiles are obtained using 8 nm and 100 nm. The penetration depth in the model is increased so that the number of elements of calculation, and thus the calculation time, can be reduced. All the layers are considered to have isotropic thermal conductivities and the interface between them is considered to be non-resistive.

| Property | Ta | NdFeB | $SiO_2$ | Si |
|---|---|---|---|---|
| Thermal conductivity, k $[Wm^{-1}K^{-1}]$ | 54.40 | 8.95 | 1.40 | 141.00 |
| Specific heat, c $[J\,kg^{-1}K^{-1}]$ | 140 | 440 | 740 | 700 |
| Density, $\rho$ $[kg\,m^{-3}]$ | $16.60 \cdot 10^3$ | $7.5 \cdot 10^3$ | $2.20 \cdot 10^3$ | $2.33 \cdot 10^3$ |
| Emissivity, $\varepsilon$ | 0.78 | - | - | - |
| Reflectivity, R | 0.49 | - | - | - |

Table 1: Materials' properties

Figure 3a shows a plan-view of the feature sizes obtained for different combinations of parameters. For instance, if one parameters is varied at a time, the increasing feature dimensions indicated by the arrow would be related to:

- Increasing initial temperature of the sample;

- Increasing external applied field;

- Increasing laser fluence;

- Decreasing coercivity of the magnetic film.

Figure 3b presents a side-view of the features related to the same parameters. As it can be observed, an increase in the depth of reversal is obtained with a simultaneous increase in the lateral dimensions. In some cases, it can be interesting to have magnetic features with high aspect ratios, i.e., deep reversal in a narrow zone. The simulations shown here considered isotropic materials and clearly in this case high aspect ratios with deep reversal cannot be achieved. However, simulations considering anisotropic materials have shown that deeper heat diffusion can be obtained. Also, given that a whole grain is magnetically reoriented once reversal is nucleated, columnar grain structures could be used to increase the depth of reversal without necessarily increasing the depth of heat diffusion.
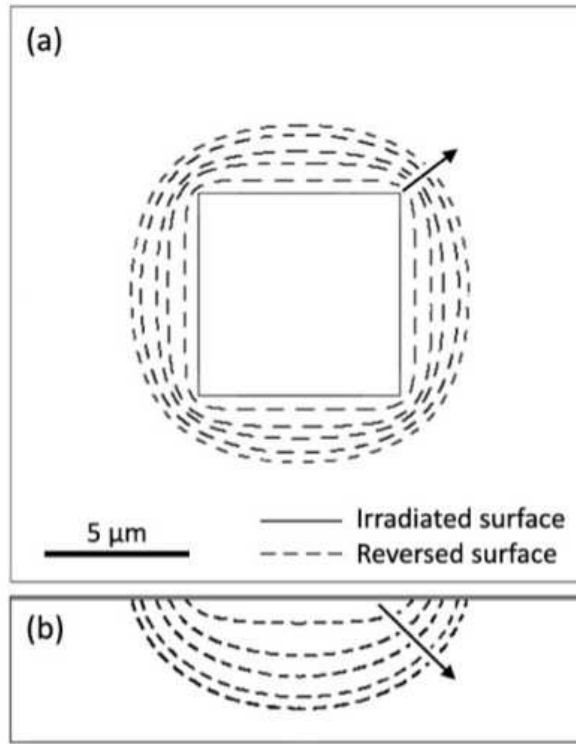
Figure 3: (a) Plan-view (b) and side-view of different reversal patterns related to the parameters used for TMP. The arrows indicate how the profile changes as the temperature of the sample, the laser fluence and/or the applied field are increased, or when the initial coercivity of the sample is decreased.

# Annex B - Heat diffusion model

A heat diffusion model is used to calculate the temperature profile due to irradiation and thus to estimate the depth of the magnetically reversed patterns. MATLAB is used to carry out 1D simulations for the sample structure represented in Figure 1. The silicon substrate is considered to be a semi-infinite medium due to its large thickness (525 $\mu$m) compared to the other layers. The upper surface of the block is irradiated with a 248 nm-wavelength laser pulse of fluence 240 mJ/cm$^2$. The energy is considered to be equally distributed over the pulse duration of 25 ns. We consider the distribution of energy in space to be laterally homogeneous. The contact region between different layers is considered to be non-resistive. Neither grain boundaries nor lattice defects were taken into account for the simulations, thus the material is considered to be spatially homogeneous.
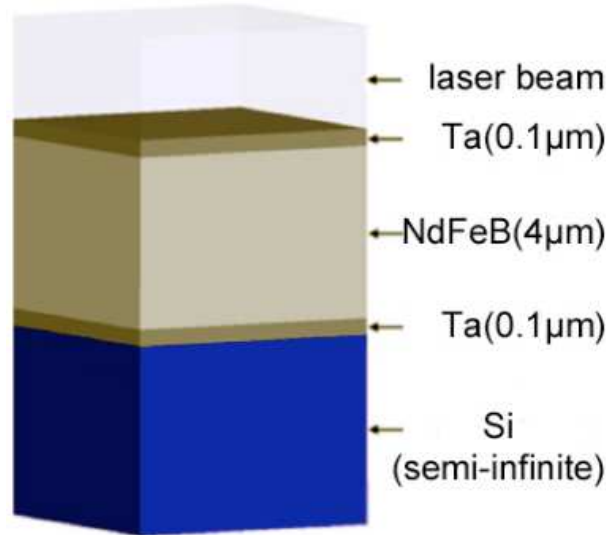


Figure 1: Schematic representation of the film structure considered in the 1D heat diffusion model.

Fourier's law for heat conduction with the energy present in the system gives

$$\rho c \frac{\partial T}{\partial t} = k \frac{\partial^2 T}{\partial x^2} + q \tag{1}$$

where $\rho$ is the materials' density, $c$ its heat capacity, and $k$ its thermal conductivity, while $q = q_L + q_R$ with $q_L$ and $q_R$ representing the heat input from the laser pulse and heat loss due to radiation, respectively. As heat transfer to or from the sample occurs at the surface, the following equations are only valid there ($x_0$) and for the rest of the sample $q$ is zero at all times.

$$q_L = \frac{(1-R)F}{gt_p} \left[\frac{J}{m^3 s}\right] \forall\, t \in [t_1, t_p]\, and\, \forall\, x \in [x_0, g] \tag{2}$$

$$q_R(x_0) = \frac{\varepsilon \sigma T^4}{\Delta x} \left[\frac{J}{m^3 s}\right] \forall\, t \in [t_1, t_p] \leftrightarrow T(x_0) > 300K \tag{3}$$

where $F$ represents the laser pulse fluence (energy per unit area), $R$ the reflectivity of the top layer at the specific wavelength used, $g$ is the depth of penetration of the laser light into the film, $t_p$ is the pulse duration, $\varepsilon$ is the top layer's emissivity and $\sigma$ is the Stefan-Boltzmann's constant $(5.67 \cdot 10^{-8} W m^{-2} K^{-4})$. The material properties used to simulate the heat diffusion are shown in Table 1, in Annex A.

Calculating $q_L$ and $q_R$ shows that the temperature at the sample's surface must be over 1500 K for $q_R$ (heat loss through radiation) to be significant. Using the experimental fluence, the surface's temperature doesn't exceed 1000 K, which allows radiation loss $q_R$ to be neglected. The heat equation can be rewritten as

$$\rho c \frac{\partial T}{\partial t} = k \frac{\partial^2 T}{\partial x^2} + q_L \tag{4}$$

Results for the simulation of heat diffusion in one dimension are plotted in the following graph.
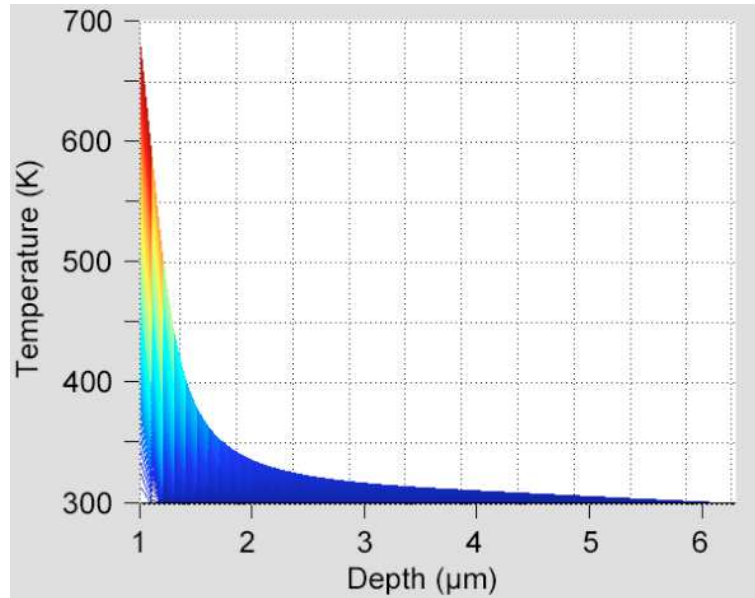


Figure 2: Maximum temperature achieved as a function of the depth in the film.

# Scientific Papers

1   N. M. Dempsey, L. V. Cuong, L. F. Zanini, M. Kustov and F. Dumas-Bouchiat.
    **Micro-magnetic imprinting of high field gradient magnetic flux sources**
    (submitted)

2   G. Blaire, A. Masse, L. F. Zanini, S. Delshadi, V. Gaude, T. Honegger, D. Peyrade,
    M. Weidenhaupt, N. M. Dempsey, F. Dumas-Bouchiat, F. Bruckert, O. Cugat and
    G. Reyne.
    **Magnetic microfluidic microsystem (Bio-Mag-MEMS) combining
    magnetophoresis and dielectrophoresis for biological applications**
    *European Physical Journal B*, (accepted)

3   O. Osman, L. F. Zanini, M. Frénéa-Robin, F. Dumas-Bouchiat, N. M. Dempsey,
    G. Reyne, F. Buret and N. Haddour.
    **Monitoring the endocytosis of magnetic nanoparticles by cells using
    permanent micro-flux sources**
    *Biomedical Microdevices*, 14, 974-954 (2012) [doi:10.1007/s10544-012-9673-4]

4   L. F. Zanini, O. Osman, M. Frénéa-Robin, N. Haddour, N. M. Dempsey, G. Reyne
    and F. Dumas-Bouchiat.
    **Micromagnet structures for magnetic positioning and alignment**
    *Journal of Applied Physics*, 111, 07B312 (2012) [doi:10.1063/1.3675067]

5   L. F. Zanini, N. M. Dempsey, D. Givord, G. Reyne and F. Dumas-Bouchiat.
    **Autonomous micro-magnet based systems for highly efficient magnetic
    separation**
    *Applied Physics Letters*, 99, 232504 (2011) [doi:10.1063/1.3664092]

6   F. Dumas-Bouchiat, L. F. Zanini, M. Kustov, N. M. Dempsey, R. Grechishkin, K.
    Hasselbach, J. C. Orlianges, C. Champeaux, A. Catherinot and D. Givord.
    **Thermomagnetically patterned micromagnets**
    *Applied Physics Letters*, 96, 102511 (2010) [doi:10.1063/1.3341190]

# Bibliography

[1] G. M. Whitesides, "The origins and the future of microfluidics," *Nature*, vol. 442, pp. 368–373, 2006.

[2] S. Amiri and H. Shokrollahi, "The role of cobalt ferrite magnetic nanoparticles in medical science," *Materials Science and Engineering: C*, vol. 33, no. 1, pp. 1 – 8, 2013.

[3] J. P. Sumner, E. M. Shapiro, D. Maric, R. Conroy, and A. P. Koretsky, "In vivo labeling of adult neural progenitors for mri with micron sized particles of iron oxide: Quantification of labeled cell phenotype," *NeuroImage*, vol. 44, no. 3, pp. 671 – 678, 2009.

[4] J. Suh, M. Dawson, and J. Hanes, "Real-time multiple-particle tracking: applications to drug and gene delivery," *Advanced Drug Delivery Reviews*, vol. 57, no. 1, pp. 63 – 78, 2005. Advances in Fluorescence Imaging: Opportunities for Pharmaceutical Science.

[5] K. Hadinoto, K. Zhu, and R. B. Tan, "Drug release study of large hollow nanoparticulate aggregates carrier particles for pulmonary delivery," *International Journal of Pharmaceutics*, vol. 341, no. 102, pp. 195 – 206, 2007.

[6] A. Jayalekshmi, S. P. Victor, and C. P. Sharma, "Magnetic and degradable polymer/bioactive glass composite nanoparticles for biomedical applications," *Colloids and Surfaces B: Biointerfaces*, vol. 101, pp. 196 – 204, 2013.

[7] J. Chen, Z. Guo, H.-B. Wang, M. Gong, X.-K. Kong, P. Xia, and Q.-W. Chen, "Multifunctional fe3o4@c@ag hybrid nanoparticles as dual modal imaging probes and near-infrared light-responsive drug delivery platform," *Biomaterials*, vol. 34, no. 2, pp. 571 – 581, 2013.

[8] M. A. M. Gijs, F. Lacharme, and U. Lehmann, "Microfluidic applications of magnetic particles for biological analysis and catalysis," *Chem. Rev.*, vol. 110, no. 3, p. 1518–1563, 2009.

[9] J. K. Oh and J. M. Park, "Iron oxide-based superparamagnetic polymeric nanomaterials: Design, preparation, and biomedical application," *Progress in Polymer Science*, vol. 36, no. 1, pp. 168 – 189, 2011.

[10] M. Zborowski and J. Chalmers, *Magnetic cell separation.* Laboratory techniques in biochemistry and molecular biology, Elsevier, 2008.

[11] S. Khashan and E. Furlani, "Effects of particle–fluid coupling on particle transport and capture in a magnetophoretic microsystem," *Microfluidics and Nanofluidics*, vol. 12, pp. 565–580, 2012.

[12] H. Bruus, *Theoretical microfluidics.* Oxford master series in condensed matter physics, Oxford University Press, 2008.

[13] S. Hardt and F. Schönfeld, *Microfluidic Technologies for Miniaturized Analysis Systems.* Springer, 2007.

[14] A. Givan, *Flow cytometry: first principles.* Wiley-Liss, 2001.

[15] D. Di Carlo, D. Irimia, R. G. Tompkins, and M. Toner, "Continuous inertial focusing, ordering, and separation of particles in microchannels," *Proceedings of the National Academy of Sciences*, vol. 104, no. 48, pp. 18892–18897, 2007.

[16] C. Wang, S. V. Jalikop, and S. Hilgenfeldt, "Size-sensitive sorting of microparticles through control of flow geometry," *Applied Physics Letters*, vol. 99, no. 3, p. 034101, 2011.

[17] T. Laurell, F. Petersson, and A. Nilsson, "Chip integrated strategies for acoustic separation and manipulation of cells and particles," *Chem. Soc. Rev.*, vol. 36, pp. 492–506, 2007.

[18] J. D. Adams and H. T. Soh, "Tunable acoustophoretic band-pass particle sorter," *Applied Physics Letters*, vol. 97, no. 6, p. 064103, 2010.

[19] J. D. Adams, P. Thevoz, H. Bruus, and H. T. Soh, "Integrated acoustic and magnetic separation in microfluidic channels," *Applied Physics Letters*, vol. 95, no. 25, p. 254103, 2009.

[20] F. Petersson, A. Nilsson, C. Holm, H. Jonsson, and T. Laurell, "Continuous separation of lipid particles from erythrocytes by means of laminar flow and acoustic standing wave forces," *Lab Chip*, vol. 5, 2005.

[21] R. Pethig, "Review article—dielectrophoresis: Status of the theory, technology, and applications," *Biomicrofluidics*, vol. 4, no. 2, p. 022811, 2010.

[22] U. Kim, C.-W. Shu, K. Y. Dane, P. S. Daugherty, J. Y. J. Wang, and H. T. Soh, "Selection of mammalian cells based on their cell-cycle phase using dielectrophoresis," *Proceedings of the National Academy of Sciences*, vol. 104, no. 52, pp. 20708–20712, 2007.

[23] S.-I. Han, S.-M. Lee, Y.-D. Joo, and K.-H. Han, "Lateral dielectrophoretic microseparators to measure the size distribution of blood cells," *Lab Chip*, vol. 11, 2011.

[24] K.-H. Han and A. B. Frazier, "Lateral-driven continuous dielectrophoretic microseparators for blood cells suspended in a highly conductive medium," *Lab Chip*, vol. 8, 2008.

[25] M. Nieto-Vesperinas, J. Sáenz, R. Gómez-Medina, and L. Chantada, "Optical forces on small magnetodielectric particles.," *Optical Express*, vol. 11, no. 18, p. 11428, 2010.

[26] A. Rohrbach and E. H. K. Stelzer, "Three-dimensional position detection of optically trapped dielectric particles," *Journal of Applied Physics*, vol. 91, no. 8, pp. 5474–5488, 2002.

[27] A. Rohrbach, "Stiffness of optical traps: Quantitative agreement between experiment and electromagnetic theory," *Phys. Rev. Lett.*, vol. 95, p. 168102, Oct 2005.

[28] M. M. Wang, E. Tu, D. E. Raymond, J. M. Yang, H. Zhang, N. Hagen, B. Dees, E. M. Mercer, A. H. Forster, I. Kariv, P. J. Marchand, and W. F. Butler, "Microfluidic sorting of mammalian cells by optical force switching," *Nature Biotechnology*, vol. 23, pp. 83–87, 2004.

[29] S.-K. Hoi, Z.-B. Hu, Y. Yan, C.-H. Sow, and A. A. Bettiol, "A microfluidic device with integrated optics for microparticle switching," *Applied Physics Letters*, vol. 97, no. 18, p. 183501, 2010.

[30] S. Miltenyi, W. Müller, W. Weichel, and A. Radbruch, "High gradient magnetic cell separation with macs," *Cytometry*, vol. 11, no. 2, pp. 231–238, 1990.

[31] M. Biotec, "Miltenyi biotec website, http://www.miltenyibiotec.com," Aug. 2012.

[32] K. Hoshino, Y.-Y. Huang, N. Lane, M. Huebschman, J. W. Uhr, E. P. Frenkel, and X. Zhang, "Microchip-based immunomagnetic detection of circulating tumor cells," *Lab Chip*, vol. 11, 2011.

[33] G. R. Souza, J. R. Molina, R. M. Raphael, M. G. Ozawa, D. J. Stark, C. S. Levin, L. F. Bronk, J. S. Ananta, J. Mandelin, M.-M. Georgescu, J. A. Bankson, J. G. Gelovani, T. C. Killian, W. Arap, and R. Pasqualini, "Three-dimensional tissue culture based on magnetic cell levitation," *Nature Nanotechnology*, vol. 5, pp. 291–296, 2010.

[34] J. V. I. Timonen, C. Johans, K. Kontturi, A. Walther, O. Ikkala, and R. H. A. Ras, "A facile template-free approach to magnetodriven, multifunctional artificial cilia," *ACS Applied Materials and Interfaces*, vol. 2, no. 8, pp. 2226–2230, 2010.

[35] P. Tseng, D. Di Carlo, and J. W. Judy, "Rapid and dynamic intracellular patterning of cell-internalized magnetic fluorescent nanoparticles," *Nano Letters*, vol. 9, no. 8, pp. 3053–3059, 2009. PMID: 19572731.

[36] M. Bu, T. B. Christensen, K. Smistrup, A. Wolff, and M. F. Hansen, "Characterization of a microfluidic magnetic bead separator for high-throughput applications," *Sensors and Actuators A: Physical*, vol. 145-146, pp. 430–436, 2008. Special Issue: Transducers 07 Eurosensors XXI, The 14th International Conference on Solid State Sensors, Actuators and Microsystems and the 21st European Conference on Solid-State Transducers.

[37] A. Sinha, R. Ganguly, and I. K. Puri, "Magnetic separation from superparamagnetic particle suspensions," *Journal of Magnetism and Magnetic Materials*, vol. 321, no. 14, pp. 2251 – 2256, 2009. Current Perspectives: Modern Microwave Materials.

[38] Y. Moser, T. Lehnert, and M. A. M. Gijs, "Quadrupolar magnetic actuation of superparamagnetic particles for enhanced microfluidic perfusion," *Applied Physics Letters*, vol. 94, no. 2, p. 022505, 2009.

[39] B. Teste, F. Malloggi, J.-M. Siaugue, A. Varenne, F. Kanoufi, and S. Descroix, "Microchip integrating magnetic nanoparticles for allergy diagnosis," *Lab Chip*, vol. 11, pp. 4207–4213, 2011.

[40] B. Teste, F. Malloggi, A.-L. Gassner, T. Georgelin, J.-M. Siaugue, A. Varenne, H. Girault, and S. Descroix, "Magnetic core shell nanoparticles trapping in a microdevice generating high magnetic gradient," *Lab Chip*, vol. 11, pp. 833–840, 2011.

[41] S. S. Guo, C. C. Zuo, W. H. Huang, C. Peroz, and Y. Chen, "Response of super-paramagnetic beads in microfluidic devices with integrated magnetic micro-columns," *Microelectron. Eng.*, vol. 83, pp. 1655–1659, April 2006.

[42] K. Ino, M. Okochi, N. Konishi, M. Nakatochi, R. Imai, M. Shikida, A. Ito, and H. Honda, "Cell culture arrays using magnetic force-based cell patterning for dynamic single cell analysis," *Lab Chip*, vol. 8, 2008.

[43] M. Tanase, E. J. Felton, D. S. Gray, A. Hultgren, C. S. Chen, and D. H. Reich, "Assembly of multicellular constructs and microarrays of cells using magnetic nanowires," *Lab Chip*, vol. 5, 2005.

[44] D. H. Kim, U. K. Cheang, L. Kohidai, D. Byun, and M. J. Kim, "Artificial magnetotactic motion control of tetrahymena pyriformis using ferromagnetic nanoparticles: A tool for fabrication of microbiorobots," *Applied Physics Letters*, vol. 97, no. 17, p. 173702, 2010.

[45] Q. Ramadan, V. Samper, D. Poenar, and C. Yu, "On-chip micro-electromagnets for magnetic-based bio-molecules separation," *Journal of Magnetism and Magnetic Materials*, vol. 281, no. 2-3, pp. 150 – 172, 2004.

[46] Q. Ramadan, D. Poenar, and C. Yu, "Customized trapping of magnetic particles," *Microfluidics and Nanofluidics*, vol. 6, pp. 53–62, 2009.

[47] K. Smistrup, O. Hansen, H. Bruus, and M. F. Hansen, "Magnetic separation in microfluidic systems using microfabricated electromagnets - experiments and simulations," *Journal of Magnetism and Magnetic Materials*, vol. 293, no. 1, pp. 597 – 604, 2005. Proceedings of the Fifth International Conference on Scientific and Clinical Apllications of Magnetic Carriers.

[48] K. Smistrup, P. T. Tang, O. Hansen, and M. F. Hansen, "Microelectromagnet for magnetic manipulation in lab-on-a-chip systems," *Journal of Magnetism and Magnetic Materials*, vol. 300, no. 2, pp. 418 – 426, 2006.

[49] K. Smistrup, H. Bruus, and M. F. Hansen, "Towards a programmable magnetic bead microarray in a microfluidic channel," *Journal of Magnetism and Magnetic Materials*, vol. 311, no. 1, pp. 409 – 415, 2007. Proceedings of the Sixth International Conference on the Scientific and Clinical Applications of Magnetic Carriers - SCAMC-06.

[50] H. Rostaing, H. Chetouani, M. Gheorghe, and P. Galvin, "A micromagnetic actuator for biomolecule manipulation," *Sensors and Actuators A: Physical*, vol. 135, no. 2, pp. 776 – 781, 2007.

[51] B. B. Yellen, O. Hovorka, and G. Friedman, "Arranging matter by magnetic nanoparticle assemblers," *Proceedings of the National Academy of Sciences of the United States of America*, vol. 102, no. 25, pp. 8860–8864, 2005.

[52] M. A. Tahir, L. Gao, L. N. Virgin, and B. B. Yellen, "Transport of superparamagnetic beads through a two-dimensional potential energy landscape," *Phys. Rev. E*, vol. 84, p. 011403, Jul 2011.

[53] D. Issadore, H. Shao, J. Chung, A. Newton, M. Pittet, R. Weissleder, and H. Lee, "Self-assembled magnetic filter for highly efficient immunomagnetic separation," *Lab Chip*, vol. 11, 2011.

[54] P. Vavassori, M. Gobbi, M. Donolato, M. Cantoni, R. Bertacco, V. Metlushko, and B. Ilic, "Magnetic nanostructures for the manipulation of individual nanoscale particles in liquid environments (invited)," *Journal of Applied Physics*, vol. 107, no. 9, p. 09B301, 2010.

[55] H.-T. Huang, C.-Y. Chen, and M.-F. Lai, "Cells positioning using magnetic domain walls of ferromagnetic zigzag thin film," *Journal of Applied Physics*, vol. 109, no. 7, p. 07B315, 2011.

[56] G. Ruan, G. Vieira, T. Henighan, A. Chen, D. Thakur, R. Sooryakumar, and J. O. Winter, "Simultaneous magnetic manipulation and fluorescent tracking of multiple individual hybrid nanostructures," *Nano Letters*, vol. 10, no. 6, pp. 2220–2224, 2010. PMID: 20450169.

[57] M.-F. Lai, C.-Y. Chen, C.-P. Lee, H.-T. Huang, T.-R. Ger, and Z.-H. Wei, "Cell patterning using microstructured ferromagnetic thin films," *Applied Physics Letters*, vol. 96, no. 18, p. 183701, 2010.

[58] N. Pamme, J. Eijkel, and A. Manz, "On-chip free-flow magnetophoresis: Separation and detection of mixtures of magnetic particles in continuous flow," *Journal of Magnetism and Magnetic Materials*, vol. 307, no. 2, pp. 237–244, 2006.

[59] N. Pamme and C. Wilhelm, "Continuous sorting of magnetic cells via on-chip free-flow magnetophoresis," *Lab Chip*, vol. 6, 2006.

[60] M. D. Tarn, S. A. Peyman, D. Robert, A. Iles, C. Wilhelm, and N. Pamme, "The importance of particle type selection and temperature control for on-chip free-flow magnetophoresis," *Journal of Magnetism and Magnetic Materials*, vol. 321, no. 24, pp. 4115 – 4122, 2009.

[61] D. Robert, N. Pamme, H. Conjeaud, F. Gazeau, A. Iles, and C. Wilhelm, "Cell sorting by endocytotic capacity in a microfluidic magnetophoresis device," *Lab Chip*, vol. 11, 2011.

[62] M. D. Tarn, N. Hirota, A. Iles, and N. Pamme, "On-chip diamagnetic repulsion in continuous flow," *Science and Technology of Advanced Materials*, vol. 10, no. 1, p. 014611, 2009.

[63] R. Afshar, Y. Moser, T. Lehnert, and M. A. M. Gijs, "Magnetic particle dosing and size separation in a microfluidic channel," in *Sensors And Actuators B-Chemical*, vol. 154, pp. 73–80, 2011.

[64] K.-H. Han and A. B. Frazier, "Diamagnetic capture mode magnetophoretic microseparator for blood cells," *Journal of Microelectromechanical Systems*, vol. 14, no. 6, pp. 1422–1431, 2005.

[65] K.-H. Han and A. B. Frazier, "Continuous magnetophoretic separation of blood cells in microdevice format," *Journal of Applied Physics*, vol. 96, no. 10, pp. 5797–5802, 2004.

[66] D. W. Inglis, R. Riehn, R. H. Austin, and J. C. Sturm, "Continuous microfluidic immunomagnetic cell separation," *Applied Physics Letters*, vol. 85, no. 21, pp. 5093–5095, 2004.

[67] J. D. Adams, U. Kim, and H. T. Soh, "Multitarget magnetic activated cell sorter," *Proceedings of the National Academy of Sciences*, vol. 105, no. 47, pp. 18165–18170, 2008.

[68] D. W. Inglis, R. Riehn, J. C. Sturm, and R. H. Austin, "Microfluidic high gradient magnetic cell separation," *Journal of Applied Physics*, vol. 99, no. 8, p. 08K101, 2006.

[69] J. Jung and K.-H. Han, "Lateral-driven continuous magnetophoretic separation of blood cells," *Applied Physics Letters*, vol. 93, no. 22, p. 223902, 2008.

[70] H. Lee, J. Jung, S.-I. Han, and K.-H. Han, "High-speed rna microextraction technology using magnetic oligo-dt beads and lateral magnetophoresis," *Lab Chip*, vol. 10, 2010.

[71] R. Fulcrand, A. Bancaud, C. Escriba, Q. He, S. Charlot, A. Boukabache, and A.-M. Gué, "On chip magnetic actuator for batch-mode dynamic manipulation of magnetic particles in compact lab-on-chip," *Sensors and Actuators B: Chemical*, vol. 160, no. 1, pp. 1520 – 1528, 2011.

[72] S. S. Shevkoplyas, A. C. Siegel, R. M. Westervelt, M. G. Prentiss, and G. M. Whitesides, "The force acting on a superparamagnetic bead due to an applied magnetic field," *Lab Chip*, vol. 7, 2007.

[73] C. Derec, C. Wilhelm, J. Servais, and J.-C. Bacri, "Local control of magnetic objects in microfluidic channels," *Microfluidics and Nanofluidics*, vol. 8, pp. 123–130, 2010. 10.1007/s10404-009-0486-6.

[74] T. M. Vogel, *Natural Bioremediation of chlorinated compounds, In Norris. R. D., In-Situ Bioremediation of Ground Water and Geological Material: A Review of Technologies*, ch. 10. Diane Publishing Company, 1995.

[75] J. Pivetal, O. Osman, C. Vézy, M. Frenea-Robin, F. Dumas-Bouchiat, N. M. Dempsey, D. Givord, P. Simonet, F. Buret, G. Reyne, and N. Haddour, "Trapping of magnetically-labelled liposomes on flat micro-patterned hard magnetic films," *AIP Conference Proceedings*, vol. 1311, no. 192, pp. 192–197, 2010.

[76] O. Osman, L. Zanini, M. Frénéa-Robin, F. Dumas-Bouchiat, N. Dempsey, G. Reyne, F. Buret, and N. Haddour, "Monitoring the endocytosis of magnetic nanoparticles by cells using permanent micro-flux sources," *Biomedical Microdevices*, vol. 14, pp. 947–954, 2012.

[77] B. Kapitanov, N. Kornilov, Y. Linetsky, and V. Tsvetkov, "Sputtered permanent nd-fe-b magnets," *Journal of Magnetism and Magnetic Materials*, vol. 127, no. 3, pp. 289 – 297, 1993.

[78] N. M. Dempsey, A. Walther, F. May, D. Givord, K. Khlopkov, and O. Gutfleisch, "High performance hard magnetic ndfeb thick films for integration into micro-electro-mechanical systems," *Applied Physics Letters*, vol. 90, no. 9, p. 092509, 2007.

[79] A. Walther, D. Givord, N. M. Dempsey, K. Khlopkov, and O. Gutfleisch, "Structural, magnetic, and mechanical properties of 5 $\mu$m thick smco films suitable for use in microelectromechanical systems," *Journal of Applied Physics*, vol. 103, no. 4, p. 043911, 2008.

[80] A. Walther, C. Marcoux, B. Desloges, R. Grechishkin, D. Givord, and N. Dempsey, "Micro-patterning of ndfeb and smco magnet films for integration into micro-electro-mechanical-systems," *Journal of Magnetism and Magnetic Materials*, vol. 321, no. 6, pp. 590 – 594, 2009. Current Perspectives: Perpendicular Recording.

[81] F. Dumas-Bouchiat, L. F. Zanini, M. Kustov, N. M. Dempsey, R. Grechishkin, K. Hasselbach, J. C. Orlianges, C. Champeaux, A. Catherinot, and D. Givord, "Thermomagnetically patterned micromagnets," *Applied Physics Letters*, vol. 96, no. 10, p. 102511, 2010.

[82] M. Kustov, P. Laczkowski, D. Hykel, K. Hasselbach, F. Dumas-Bouchiat, D. O'Brien, P. Kauffmann, R. Grechishkin, D. Givord, G. Reyne, O. Cugat, and N. M. Dempsey, "Magnetic characterization of micropatterned ndfeb hard magnetic films using scanning hall probe microscopy," *Journal of Applied Physics*, vol. 108, no. 6, p. 063914, 2010.

[83] N. M. Dempsey and F. Dumas-Bouchiat, "Procédé de fabrication d'un film comprenant des microstructures magnétiques tridimensionnelles," *Patent FR1254667*, 2012.

[84] N. M. Dempsey, L. V. Cuong, L. F. Zanini, M. Kustov, and F. Dumas-Bouchiat, "Micro-magnetic imprinting of high field gradient magnetic flux sources," *submitted*, 2013.

[85] C. Vézy, N. Haddour, N. Dempsey, F. Dumas-Bouchiat, and M. Frénéa-Robin, "Simple method for reversible bonding of a polydimethylsiloxane microchannel to a variety of substrates," *Micro and Nano Letters*, vol. 6, pp. 871 – 873, Oct. 2011.

[86] Fluigent, "Fluigent website, http://www.fluigent.com," Sept. 2012.

[87] M. Kustov, *Characterisation and design of micro-magnets for the diamagnetic levitation of micro- and nanoparticles.* PhD thesis, Institut National Polytechnique de Grenoble, 2010.

[88] L. F. Zanini, O. Osman, M. Frenea-Robin, N. Haddour, N. M. Dempsey, G. Reyne, and F. Dumas-Bouchiat, "Micromagnet structures for magnetic positioning and alignment," *Journal of Applied Physics*, vol. 11, p. 07B312, 2012.

[89] L. F. Zanini, N. M. Dempsey, D. Givord, G. Reyne, and F. Dumas-Bouchiat, "Autonomous micro-magnet based systems for highly efficient magnetic separation," *Applied Physics Letters*, vol. 99, no. 23, p. 232504, 2011.

[90] L. F. Zanini, "Development of micro-magnets by thermo-magnetic patterning," Master's thesis, Universidade Federal de Santa Catarina, 2010.